NOVEL METHODOLOGIES FOR INVESTIGATING THE PATHOPHYSIOLOGY OF CEREBRAL ANEURYSMS

by

Zijing Zeng

BE, Tsinghua University, 2005

Submitted to the Graduate Faculty of

Swanson School of Engineering in partial fulfillment

of the requirements for the degree of

Doctor of Philosophy

University of Pittsburgh

2011

UNIVERSITY OF PITTSBURGH

SWANSON SCHOOL OF ENGINEERING

This dissertation was presented

by

Zijing Zeng

It was defended on

July 12, 2011

and approved by

Anne M. Robertson, Ph.D., Associate Professor, Department of Mechanical Engineering and Materials Science

Giovanni P. Galdi, Ph.D., Professor, Department of Mechanical Engineering and Materials Science

Michael S. Sacks, Ph.D., Professor, Department of Bioengineering

Akira Takahashi, M.D., Ph.D., Professor, Graduate school of Medicine, Tohoku University

David F. Kallmes, M.D., Professor, College of Medicine, Mayo Clinic

Dissertation Director: Anne M. Robertson, Ph.D., Associate Professor, Department of Mechanical Engineering and Materials Science

NOVEL METHODOLOGIES FOR INVESTIGATING THE PATHOPHYSIOLOGY OF CEREBRAL ANEURYSMS

Zijing Zeng, Ph.D.

University of Pittsburgh, 2011

An intracranial aneurysm (IA) is a pathological state of a cerebral artery in which the elastin and smooth muscle cells found in the healthy arterial wall are absent. Rupture of an IA is a major cause of subarachnoid hemorrhage. Hemodynamics is believed to play an important role in initiation, development and rupture of the IA. However, the coupling between hemodynamics and aneurysm pathophysiology remains poorly understood.

The initiation of cerebral aneurysms is believed to be caused by a breakdown in the homeostatic mechanism of healthy arteries, leading to destructive wall remodeling and damage. Due to its complex nature, there is a need for both controlled *in vitro* and *in vivo* studies of IA initiation. We have designed an *in vitro* flow chamber that can be used to reproduce specific magnitudes of wall shear stress and wall shear stress gradients found at the apices of arterial bifurcations, where aneurysms tend to form.

Animal models provide a mechanism for fundamental studies of the coupling between hemodynamics and pathophysiology in cerebral aneurysms. We conducted a sensitivity study to develop an accurate CFD model for an elastase-induced rabbit aneurysm model. We then used this computational model to evaluate the capability of the rabbit model to reproduce hemodynamic features typical of human IAs. Geometric and hemodynamic features of 51 rabbit aneurysm models were analyzed and shown to fall within the range reported for human IAs. This model was also used to study the relationship between aspect ratio and hemodynamics in the

aneurysm sac. An “in silico design” approach was then used to explore the possibility of extending the rabbit model to capture more of the flow categories identified in human IAs.

Based on a previously developed parametric model for human arterial bifurcations, we created and validated a parametric model for IAs. This parametric model captures important geometric and flow features of both the aneurysm and neighboring vasculature. The model is currently being used for studies of the coupling between geometry and hemodynamics in IAs. It can also be used to guide 3D reconstruction of poor quality clinical data or construct *in vitro* experimental models.

TABLE OF CONTENTS

LIST OF TABLES

LIST OF FIGURES

PREFACE

As a summary of the author's doctoral research, this thesis contains several published work, for which the author was the first author. The second chapter material was published previously in < ***Advances in Mathematical Fluid Mechanics***> (ed. A. Sequeira and R. Rannacher), Springer Verlag, Wien, 2009, pp 631-67 DOI: 10.1007/978-3-642-04068-9_35. The material in the Section 3.1 was published previously in ***Journal of Biomechanical Engineering***, 2010, Vol. 132, Volume 132, Issue 9, 091009 DOI:10.1115/1.4001311. The material in the Section 3.2 was published in ***American Journal of Neuroradiology,*** Mar 2011; 32: 595 – 601 DOI: 10.3174/ajnr.A2324. The author was the first author of these three journal papers. The permission of republishing these materials in this PhD thesis was granted by the copyright holders of these articles. Animal models used in this study were created at the Mayo Clinic under The Institutional Animal Care and Use Committee's approval.

I would like to appreciate many people's help in suggestions, assistance and references during my PhD study. My advisor, Dr. Anne M. Robertson, gives me tremendous help in both research area and professional development side. Most of my knowledge in biomechanics and vascular diseases area are learnt directly or indirectly from her. As the best PhD advisor I have seen, she gives advices to my course study, directs and inspires me in research, discusses with me on scientific subjects, revises my manuscripts with great patience, and helps me improve my

presentation before conferences. I would like to express my deepest sense of gratitude to Dr. Robertson, it is my great pleasure to work with her during the past five years.

I would also like to thank Dr. G. P. Galdi, as a great professor in Mathematics and Fluid mechanics, his classes gave me a solid foundation for my scientific background. I also appreciate his advices and encouragements during my PhD study.

My sincere thanks will also extend to my committee members, Dr. Akira Takahashi, Dr. David Kallmes, and Dr. Michael Sacks, for their help not only in my dissertation, but also in many other aspects in my PhD research and my own professional development.

I would like to thank our collaborators in Mayo clinic Dr.Kallmes' group, for their excellent work on creation of rabbit aneurysm models, image acquisition, biological response study, and flow measurements. Dr.Kallmes provided significant support on study of hemodynamics in elastase-induced rabbit aneurysm models, and many valuable suggestions in my research and manuscripts writing.

I would like to thank our collaborators in Dr.Takahashi's group in Tohoku University in Japan. Dr.Takahashi provided clinical images for the parametric model study, and gave extremely valuable suggestions and comments on the developing of the parametric aneurysm model. He also kindly provided me the opportunity and support to attend the International Intracranial Stent Meeting (ICS09), in which I gained lots of experiences and knowledge in this field.

I am thankful to my colleagues Michael Durka, Michael Hill and Dr. Lifeng Qin for help in my research and sharing experiences and knowledge during time of study. Michael Durka helped me with most of computational work on rabbit aneurysm models, including operating the numerical simulations and data processing, without his diligent work, we can't finish such a large amount of CFD work efficiently.

I appreciate the support by National Institute of Health (NIH) funding: NS-42646-01 and NS-42646-02 during the doctoral research and study.

Finally, I would like to give my deepest appreciation to my family. Without the constant support from my parents and my parents in law during my PhD study, it is impossible for me to finish this dissertation. Most important, I would like to thank my wife, Ling Zhao, for being extraordinary supportive during these years, for her diligent in every aspect of our family life, and for her continuous encouragement throughout my PhD study.

Dedicated to my wife Ling Zhao and my son Alex Zeng.

1.0 INTRODUCTION

A cerebral aneurysm is a pathological condition of cerebral arteries characterized by degeneration of the internal elastic lamina (IEL) and media, accompanied by local enlargements of the arterial wall, typically into a saccular shape. Cerebral aneurysms are predominantly found at the apices of bifurcations and outer bends of highly curved vessels in or near the circle of Willis, a network of vessels at the base of the brain [1-3]. One of the major causes of subarachnoid hemorrhage (SAH) or occasionally intra-cerebral hemorrhage (ICH) is the rupture of cerebral aneurysms, and in 50% of these cases, it is fatal [4-6]. However, the formation, progression and rupture of cerebral aneurysms are not well understood.

It is commonly accepted that hemodynamics plays a role in the initiation and further development of arterial pathologies such as intracranial aneurysms (IA). Previous investigators have postulated the manner in which the walls of IA remodel under the abnormal, intrasaccular hemodynamic stresses plays a major role in the stabilization or eventual rupture of the aneurysm [7, 8]. As a result, a large body of research has been directed at categorizing the hemodynamics inside human IA and correlating aneurysm growth as well as rupture with specific hemodynamic markers such as abnormally high or low magnitudes of wall shear stress (WSS) and oscillatory shear index (OSI) [7-11]. The intra-aneurysmal flow is affected by the geometry of the aneurysm

sac and surrounding vasculature, the existence, size and symmetry of branches arising near the aneurysm, and the position of the aneurysm sac relative to the parent vessel, e.g. side-wall, terminal or bifurcation. Efforts have been made to correlate rupture with these various geometric features [9, 12].

The coupling between hemodynamics and aneurysm pathophysiology is complex and remains poorly understood. Patient specific prognostication regarding risk of rupture might be substantially advanced by improving our understanding of the in-vivo response of the aneurysm wall to intra-saccular hemodynamic stresses. In-vitro systems provide an opportunity for highly controlled investigations of cellular response to various types of hemodynamic stresses. However, most of existing chambers (including parallel and cone-plate shape) can only provide a simple hemodynamic shear stress condition which can hardly reflect the true flow environment at the arterial bifurcation regions. The stress condition of this region is characterized by both high and low WSS distribution and high WSSG. ECs subjected to this condition exhibited increased motility, proliferation, permeability, turnover, surface adhesion, and altered protein expression [13, 14]. Thus, a flow chamber designed to mimic this impingement flow at arterial bifurcation with "well defined flow" is needed.

In order to better understand the pathophysiology of cerebral aneurysms and design effective clinical treatments to enhance the likelihood of stabilization, it is necessary to evaluate the in vivo response of the aneurysm wall to intra-aneurysmal hemodynamic stresses. A number of animal models have been created for studying aneurysm pathogenesis. One such animal model is an elastase induced aneurysm model in rabbits. In this model, saccular aneurysms are

created by elastase infusion in, and distal ligation of, the right common carotid artery (RCCA). The hemodynamic features of this animal model have been shown to lie within the normal range for human aneurysms. This model has been used to evaluate the performance of endovascular devices and evaluate changes in histology after device implantation [15-18]. The rabbit model has also been used to study the correlation of altered expression of extracellular matrix and vascular remodeling molecules with areas of low shear. For example, expression of vascular cell adhesion molecule-1 (VCAM-1) was shown to be up regulated in aneurysms at both 2 and 12 weeks after aneurysm creation. These results are consistent with results reported by Mohan et al., in which prolonged exposure of human aortic endothelial cells to low shear stress was associated with increased expression of VCAM-1 [19]. To better understand the coupling between hemodynamics and biological response within aneurysms and to evaluate flow devices, accurate estimates of flow in and around the model aneurysms are needed. The relationship between the flow field, resulting WSS in the aneurysm cavity, and associated vascular morphology can then be confidently investigated.

3D reconstructions of aneurysms from patient specific data are frequently used in preparing computational fluid dynamics (CFD) models to apply hemodynamic studies [7-10]. These 3D reconstructed models presented accurate anatomies of aneurysms and their surrounding vasculature thus lead to reliable local estimation of the hemodynamic factors. However, due to the pipeline used in this kind of geometric reconstruction and realistic geometry complexity, it is not possible to use them to systematically vary geometric features for parametric studies. Idealized models of ICA have been created for parametric studies, but they are limited by their tendency to oversimplify the geometry, thus not suitable for studying

geometric parameters and shape factors of aneurysms. This leads to the need for developing a systematic way to create parametric aneurysm models from patient geometry and use the model to conduct parametric studies.

Based on this background, the content of this dissertation will have three parts: the first part is the design and manufacture of an *in vitro* device for evaluation of cellular response to flows found at the apex of arterial bifurcations. The second part is the study of hemodynamics in the elastase induced aneurysm models in rabbit. The third part is the development of a parametric model for human intracranial aneurysms.

In the first part, detailed CFD design of the flow domain in an in vitro chamber will be discussed, fulfillment of design criteria will be presented, followed with CAD assembly design, material selection and manufacturing issues.

The second part will focus on the hemodynamics and geometries of the elastase induced aneurysms in rabbit. First, we develop the computational model to evaluate the intra-aneurysmal hemodynamics. A sensitivity study on computational domain selection of the CFD model is discussed in detail. The second part of this chapter includes a validation study of the rabbit aneurysm model: assessment of the relevance of hemodynamics in rabbit model to human aneurysms, and application of the rabbit aneurysm model to study the influence of geometric ratio on intra-aneurysmal hemodynamics. Finally, we present the development of an alternate high flow bifurcation rabbit aneurysm model and the CFD study of its hemodynamics.

Comments on the correlation between hemodynamics and the growth-remodeling processes of the aneurysm wall are included throughout the entire chapter.

In the third part, we develop a parametric model for human intracranial aneurysms using patient specific geometries. The model builds on previous work on parametric models of arteries and bifurcations. Geometric and hemodynamics results for the parametric models are compared to the original data. Examples of parametric modeling for aneurysms and parent geometries are included to illustrate the future applications of the model.

2.0 AN IN VITRO DEVICE FOR EVALUATION OF CELLULAR RESPONSE TO FLOWS FOUND AT THE APEX OF ARTERIAL BIFURCATIONS

2.1 BACKGROUND AND PURPOSE

The arterial system is in some sense an optimized network of vessels [20]. In particular, it appears that the vasculature is designed to maintain the wall shear stress in vessels in a specific range, e.g. [21]. This is reflected in both the geometry of the vasculature and also in its ability to locally modify the vessel caliber through dilation and remodeling in response to changes in shear stress [22-24]. Throughout much of the arterial system, the velocity field is predominantly parallel to the vessel centerline. However, there are locations such as bifurcations, regions of sudden expansion and highly curved segments where the hemodynamic loading is far from this idealized flow, e.g. [25, 26]. These regions may display recirculation, flow impingement, acceleration/deceleration, and points of flow separation. In these areas, the magnitude and direction of the wall shear stress vector, $\underline{t}_s$, may change in space and time and be far from that associated with the nearly uni-directional flow found in straighter, more uniform arteries. For this reason, these flows are often referred to as "disturbed flows."

The fact that pathological changes to the vessel wall are correlated with these flows suggests the nature of the stress vector in these areas is outside the "optimal range" and is

challenging for the vasculature. For example, intimal thickening is found to be correlated with regions of very low and oscillating wall shear stress often found in the carotid artery sinus, e.g. [27]. The destructive remodeling of the vessel wall in these regions appears to be a maladaptive response to hemodynamics in this region.

It is now understood that the endothelial cells (EC) which line our arteries can distinguish between some types of complex flows. Their response to altered $\underline{t}_s$ includes changes in cell shape and alignment, changes in activation of ion channels, intercellular signaling, gene expression changes at the level of transcription and protein synthesis (see, e.g. [26, 28, 29]). These local responses can trigger a cascade of large scale events such as vasodilation, and vessel remodeling.

Because of the importance of the EC in both the normal maintenance of the arterial wall as well as pathological changes associated with disease, numerous in vivo and in vitro studies have been directed at understanding the coupling between $\underline{t}_s$ and EC response. Various hemodynamic parameters have been introduced with the intent of replacing this complex vector function with scalar quantities that capture the most significant features of $\underline{t}_s$ for a given biomechanical response. One such parameter is the magnitude of $\underline{t}_s$ which is nearly uniformly accepted as an appropriate measure of $\underline{t}_s$. It is simply denoted as WSS.

Another hemodynamic feature of interest is the surface gradient of the wall shear stress. The choice of a scalar measure for this quantity is less clear. This is particularly true for curved surfaces where the spatial gradient of $\underline{t}_s$ has an out of plane contribution. A variety of scalar functions of the spatial gradient of $\underline{t}_s$ are used in the literature. Unfortunately, they are all denoted

as WSSG, confounding comparison of results from different groups [30-32]. In most cases, a non-negative quantity is used, which cannot capture the dependence of the biological response on the sign of the gradient. In this chapter, we introduce a new measure of the wall shear stress gradient denoted as WSSVG rather than WSSG to emphasize that it is dependent on the gradient of the wall shear stress vector not the gradient of the WSS. This parameter has a number of advantages. It is appropriate for complex 3D flows and reduces to expected measures in simple 2D flows. The sign of WSSVG reflects the increasing and decreasing nature of $\underline{t}_s$. In addition, this measure is a scalar invariant of a second order tensor, so will be appropriate for use in constitutive equations for vessel remodeling in response to hemodynamic loads (e.g. [33, 34]).

There is substantial evidence to support the hypothesis that hemodynamics also play an important role in the initiation and development of intracranial aneurysms (ICA), (see, e.g. [35-39]. At the bend of arteries and at bifurcations, the blood impinges on the arterial wall where it is redirected with strong spatial variations in $\underline{t}_s$ downstream of the impingement point.

Earlier computational work suggested that the impulse of the incoming flow on the apex region could directly damage even healthy arterial walls [2]. It was later shown that the results supporting this conjecture were unphysical due to the use of perfectly sharp corners in the study [40]. The local increase in pressure at the apex is on the order of a few mmHg, much smaller than the normal variation in pressure throughout the vasculature [41]. Since cerebral aneurysms can form in humans in the absence of hypertension, we conjecture the role of elevated hemodynamic pressures in aneurysm formation is to hasten mechanical damage and ultimate failure of an IEL previously weakened by biochemical factors. The magnitude and spatial

distribution of $\underline{t}_s$ at the apex of the bifurcation is drastically different from the seemingly desired distribution of more uniform flow. It has been conjectured that some aspect of $\underline{t}_s$ at the apex of the bifurcation initiates a cascade of biochemical activities that lead to the degradation of the IEL and media, rather than directly damaging the wall. For example, the character of $\underline{t}_s$ may lead to an imbalance in the production of enzymes responsible for natural remodeling and turnover of the extracellular matrix.

Motivated by diseases such as atherosclerosis as well as the frequent onset of intimal hyperplasia following bypass surgery, numerous in vitro and in vivo studies have been performed to explore the role of WSS and WSSVG in pathological changes to the arterial wall (e.g. [32, 42, 43]). While some in vitro chambers are designed to isolate the effect of specific parameters, others attempt to reproduce a specific "disturbed" flow found in vivo. For example, parallel plate and cone-andplate flow chambers have been used to study the role of WSS under conditions for which there is no spatial or temporal gradient in $\underline{t}_s$. A backward facing step was introduced into these chambers to recreate the recirculating flow associated with intimal hyperplasia in vivo [8], including a reattachment point and regions of deaccelerating and accelerating flow. DePaola et al. appear to be the first to conjecture that endothelial cells may be sensitive to the gradient of $\underline{t}_s$.

Recent in vivo work suggests both the WSS and the WSSVG play an important role in aneurysm initiation. Significantly, the sign of the gradient in $\underline{t}_s$ has been reported to be important for pre-aneurysmal changes [32]. However, the chambers designed for atherosclerosis do not reproduce the salient hemodynamic features found at the apices of bifurcations where aneurysms

tend to form. In particular, the WSS field downstream of the stagnation point is monotonic and the surface gradient of $\underline{t}_s$ is much smaller than that found at the apex of bifurcations. There is a pressing need for an in vitro flow chamber which reproduces the WSS and WSSVG fields associated with aneurysm formation in vivo.

An in vitro T-chamber for studies of cellular response to apex flows was first introduced by Robertson et al. [44, 45]. This chamber well approximates the WSS field found in idealized human cerebral bifurcations and forms the starting place for the present work. In this work, we design a T-chamber which successfully reproduces specific profiles in both WSS and WSSVG found to be associated with pre-aneurysm changes in canine arterial bifurcations [32, 46].

2.2 METHODS

2.2.1 Governing Equations

We perform numerical simulations in an idealized arterial bifurcation as well as in segments of an in vitro flow chamber. For both cases, the fluid is idealized as incompressible, homogeneous and linearly viscous (Newtonian) and the flow is modeled as steady and isothermal. The relevant governing equations are therefore the incompressibility condition and equation of linear momentum. Referred to rectangular Cartesian coordinates, x_i, the governing equations in the fluid domain, Ω, are

$$v_{i,i} = 0$$

$$\rho v_{i,j} v_j = -p_{,i} + \mu v_{i,jj} \tag{1}$$

where v_i are the components of the velocity vector $\underline{v}$, p is the combined term representing the Lagrange multiplier arising from the incompressibility constraint (equivalent to the mechanical pressure) and the gravitational potential, μ is the constant viscosity and ρ is the constant mass density. The notation $()_{,i}$ denotes $\frac{\partial()}{\partial xi}$ and repeated indices imply summation over the values of the index i = 1, 2, 3. The bounding surface of Ω is composed of rigid walls where the velocity is prescribed to be zero, as well as N inflow and outflow surfaces. The locations of these N surfaces are somewhat arbitrary, arising when we truncate the physical domain in order to make the computational problem tractable. The choice of boundary conditions on these surfaces is not unique from the physical or mathematical perspective. We will specify the velocity on surfaces Γα and the modified stress vector $\underline{t}$ on surfaces denoted as Γα where α = [0, 1, 2, ..N − 1]. The choice of these surfaces and the corresponding conditions are problem specific and therefore will be given below for particular simulations. The modified stress vector is defined as

$$t_i' \equiv (-p\delta_{ij} + \mu v_{i,j})n_j \tag{2}$$

where n_j are the components of the outward normal to the surface Γα. It is physically reasonable and computationally straightforward in appropriately chosen FEM formulations to prescribe $\underline{t}$ to be parallel to $\underline{n}$ on inlet and outlet surfaces, so that from (2),

$$(-p\delta_{ij} + \mu v_{i,j})n_j = Cn_i \tag{3}$$

For a discussion of the implementation of (3) using the finite element method see, for example [47], for a comparison of this condition with other inflow/outflow conditions see [48], and for numerical and some mathematical aspects of this boundary condition, see [49]. More recently, Galdi has addressed the mathematical properties of the system (1) for the case of steady

and unsteady flows when condition (3) is applied at all inflow and outflow surfaces [50]. Kucera and Skalak have considered the unsteady problem with more general boundary conditions [42]. An early discussion of physical anomalies arising when the usual Cauchy stress vector rather than the modified stress vector is specified at outflow boundaries is given in [51].

In this chapter, we give a more precise meaning to the scalar quantities called the wall shear stress and wall shear stress gradient. The central considerations are (i) that these quantities be physically meaningful based on known biological data and (ii) that they are scalar invariants. This last point is important when these quantities are used in constitutive equations for destructive remodeling and damage of the arterial wall such as the model proposed in [52].

We now consider the fluid domain to be surrounded by a solid domain Ω' (the wall), Fig. 1. Consider an arbitrary point P on the interface of these domains $\partial\Omega$ with unit normal $\underline{n}$ directed into the fluid domain. The wall shear stress vector, $\underline{t}_s$ at P is defined as

$$\underline{t_s} = \underline{t} - \underline{t} \cdot \underline{n}\,\underline{n} \tag{4}$$

We would like the WSS to be a scalar function of $\underline{t}_s$ with dimensions of stress. Since a scalar valued function of a vector is invariant if and only if it can be expressed as a function of its inner product (e.g. [53]), the choice of WSS is clear,

$$WSS = \left|\underline{t_s}\right| = \sqrt{\underline{t_s} \cdot \underline{t_s}} \tag{5}$$

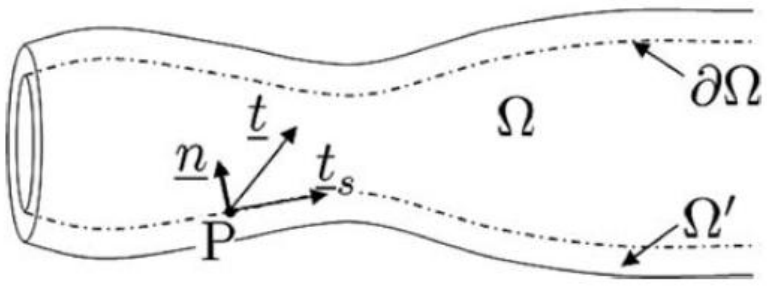

Figure 2.1 Schematic of the vessel lumen and arterial wall

To our knowledge, there is only one work which does not use this definition [54]. We denote the spatial gradient of $\underline{t}_s$ with respect to surface coordinates as grads $\underline{t}_s$. For curved surfaces, grads $\underline{t}_s$ may not be a two dimensional tensor because the gradient of the surface base vectors may not lie on the surface. For example, consider the surface of a cylinder of circular cross section which is parameterized in terms of standard cylindrical components (θ, z). The grads $\underline{t}_s$ has an $e_r \otimes e_\theta$ component. We do not expect the biological cells to be sensitive to a purely geometric contribution of this kind, so we define a modified gradient of the wall shear stress vector as

$$\underline{G} = grad_s\, \underline{t}_s - \underline{n} \otimes (\underline{n} \cdot grad_s \underline{t}_s) \tag{6}$$

The quantity $\underline{G}$ is a two dimensional second order tensor with two principal invariants tr($\underline{G}$) and det$G$, (e.g. [53]). Based on physical motivations elaborated on below, we define the *WSSVG* as,

$$WSSVG = tr\underline{G} \tag{7}$$

We emphasize that WSSVG is an invariant of the gradient of the wall shear stress *vector* and not the gradient of the WSS. To avoid confusion, we do not use the notation WSSG. As we

will see below, this is an important distinction and necessary to ensure the WSSVG captures the desired physical behavior.

To attain a clearer understanding of the physical meaning of these quantities, we consider the special case of 2D flow of an incompressible linearly viscous fluid over a flat surface. Using 2D rectangular coordinates (x_1, x_2), we define a solid boundary at $x_2 = 0$ with normal $\underline{e}_2$ into the fluid and consider velocity fields of the form, $\underline{v} = v_1(x_1, x_2)\underline{e}_1 + v_2(x_1, x_2)\underline{e}_2$. For such flows,

$$\underline{t}_s = t_{s1}\underline{e}_1 = \mu \frac{\partial v_1}{\partial x_2}\underline{e}_1 \ , \qquad WSS = \mu \left|\frac{\partial v_1}{\partial x_2}\right| \quad at\ x_2 = 0 \tag{8}$$

where we have made use of the no-slip condition. We see the WSS has the expected meaning of the magnitude of the viscous drag per unit area on the wall by the fluid.

Furthermore, for these 2D flows,

$$\left[grad_s \underline{t}_s\right] = \begin{bmatrix} \mu \frac{\partial^2 v_1}{\partial x_1 \partial x_2} & 0 \\ 0 & 0 \end{bmatrix}, \quad at\ x_2 = 0 \tag{9}$$

For flat plates, Eq. (6) simplifies to $\underline{G} = \text{grad}_s\ \underline{t}_s$. It therefore follows directly from (7) that,

$$WSSVG = \mu \frac{\partial^2 v_1}{\partial x_1 \partial x_2} \tag{10}$$

The second principal invariant, $\det(\text{grad}_s\ \underline{t}_s)$, is zero for these 2D flows and so the choice to use the trace invariant is clear. A linear dependence on this invariant is consistent with the desired dimensions of WSSVG. It is clear from (10) that WSSVG is capable of distinguishing between increasing and decreasing $\underline{t}_{s1}$ through its sign.

The difference in using the surface gradient of WSS rather than the surface gradient of the stress vector is clear if we consider a special case of the 2D flow which is symmetric about the plane $x_1 = 0$. As an example, consider flows for which the fluid impinges on the plate with $v_1(-x_1, x_2) = -v_1(x_1, x_2)$ and $v_2(-x_1, x_2) = v_2(x_1, x_2)$. The idealized 2D flow fields we consider below for the apex region of the T-chamber display this symmetry. From the perspective of the response of the endothelial cells to flow of this type, we would like our "measured" WSSVG to display a symmetry about the plane $x_1 = 0$ as well. It follows directly from the result (10), that WSSVG $(-x_1, x_2)$ =WSSVG(x_1, x_2), as desired. Note that grad*s* WSS is an odd function of x_1 and so would predict different behavior on either side of the symmetry plane.

2.2.2 Flow in idealized bifurcation models

The T-chamber developed here is designed to reproduce shear stress fields which are typical of the apex region of cerebral arterial bifurcations. With this in mind, we briefly review the central features of such flows. Unsteady and steady flows in arterial bifurcations have been the subject of intense research, due to their relevance in atherosclerosis and other vascular diseases (see, e.g. [27, 40, 55, 56]). Here, we concentrate on flow in the apex region of bifurcations, where cerebral aneurysms are most likely to form.

Quantitative features of the bifurcation flow, such as the distribution of WSS, are dependent on the bifurcation geometry as well as the flow and fluid parameters. One such idealized bifurcation model with two planes of symmetry is shown in Fig. 2a, b. The bifurcation

geometry was created using a parametric model for human cerebral bifurcations [6, 49]. Approximate solutions to (1) were obtained using the finite element method, implemented in ADINA (Automatic Dynamic Incremental Nonlinear Analysis, Watertown, MA). The velocity was prescribed to be zero on the lateral (rigid) walls. Boundary condition (3) was applied at the inlet and outlet surfaces with C = 0 on (Γ_1, Γ_2) and C set equal to a positive constant on Γ_0, chosen such that a Reynolds number (Re) of 255 was achieved, where

$$Re = \rho \overline{V} D / \mu \tag{11}$$

D is the diameter at Γ_0 and $\overline{V}$= 4Q/(πD^2) is the average velocity at the same location. For these studies, we choose parameters ρ = 1.05 g/cm^3 and μ = 0.035 g/(cm s), D = 4mm and from (11), $\overline{V}$ = 21 cm/s. The diameter of both daughter branches was set to 2.4 mm. These values are relevant for cerebral aneurysm formation.

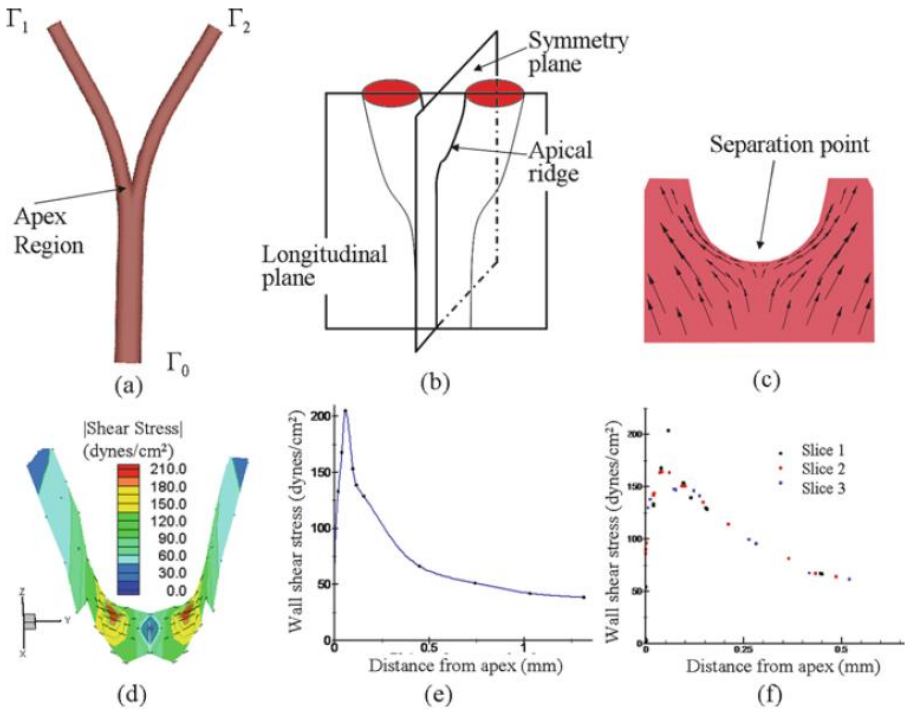

Figure 2.2 Flow in an idealized bifurcation model.

(a) Idealized geometry and computational domain Ω. (b) Schematic of cutting planes for bifurcation. (c) Velocity vectors in longitudinal plane of apex region. (d) Contours of the WSS (dynes/cm^2) with vectors $\underline{ts}$ superimposed on iso-contours. (e) WSS along apical ridge defined by the intersection of apex and longitudinal plane. Distance is measured from impingement point. (f) WSS along apical ridge (slice 1) and planes parallel and separated by 0.04 and 0.08mm from the longitudinal plane (slice 2 and 3, respectively)

For a saddle shaped region in the neighborhood of the bifurcation in Fig. 2e, WSS along the apical ridge (formed by the intersection of saddle region and the longitudinal plane) is plotted as a function of distance from the impingement point. As can be seen in these two figures, WSS is non-monotonic, increasing from zero at the impingement point to a local maximum value and then decreasing again.

It is clear from Fig. 2d that the WSS field is fairly two dimensional in nature in the bifurcation region. To assess this further, consider the WSS at points denoted as slice 1 in Fig. 2f, corresponding to the curve in Fig. 2e. The WSS along two other curves is shown (labeled slice 2 and 3) in Fig. 2f. These correspond to the curves formed by the intersection of the saddle region with planes parallel to the longitudinal plane, separated from it by distances of 0.04 and 0.08 mm, respectively. If the stress field was perfectly two-dimensional, these curves would be identical. Though the maximum drops slightly with distance from the longitudinal plane, the WSS can be seen to be close to two-dimensional in this region. Furthermore the direction of vectors $\underline{t}_s$ are approximately tangent to these planes, Fig. 2d. This near two-dimensionality is likely due to the fact that the principal radii of curvature at the apex, are of opposite sign. Our in vitro chamber makes use of this near two dimensionality in the neighborhood of the apex.

Meng et al. [32] evaluated the response of vascular tissue to sudden exposure to apical $\underline{t}_s$ fields. Artificial bifurcations were surgically created from native segments of common carotid arteries in dogs. Using CFD analysis in reconstructions of these vessels, they obtained WSS fields similar in form to those shown in Fig. 2e. They divided the apex into three distinct hemodynamic regions which we denote as Regions A,B,C. Region A displays WSS $\leq$ 20 dynes/cm^2, Region B displays WSS > 20 dynes/cm^2, and positive WSSVG and Region C displays WSS > 20 dynes/cm^2 and negative WSSVG. Distinct histological responses were found in these regions. Significantly, in five of six cases, Region B displayed pre-aneurysmal changes including a thinned wall, disrupted IEL, reduction in smooth muscle cells and loss of endothelium. However, these same changes were not found in region C where the WSS

magnitude was equally high though the WSSVG was of a negative sign. In that work, elevated WSS and positive elevated WSSVG were found to be important for aneurysm initiation.

2.2.3 Rationale behind Design of Fluid Domain in the Bifurcation Chamber

The geometric features of the T-chamber designed by Chung and collaborators [41, 45] well approximates the WSS field found in an idealized human cerebral bifurcations. This chamber forms the starting place of the present work. Motivated by the in vivo results just discussed, this T-chamber was modified to reproduce the quantitative features of both the WSS and WSSVG of the range reported in [32]. Many tests of cellular function provide only a relative measure (e.g. Western blotting, etc.) and so it is desirable to build the chamber to recreate both the bifurcation stress field as well as control fields. We introduce two control regions for exposure of cells to constant WSS.

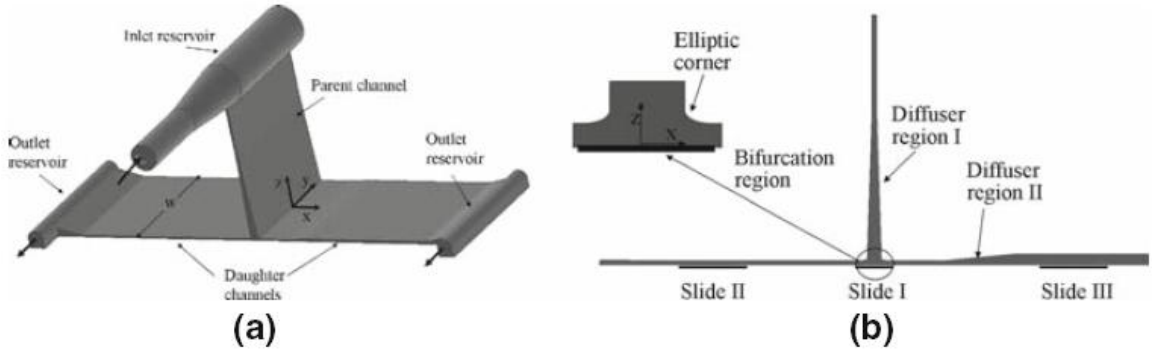

Figure. 3

Figure 2.3. Schematic of main features of fluid domain in flow chamber.

(a) Entire 3D fluid domain (b) 2D cross section of fluid domain without reservoirs

A schematic of the general geometric features of the T-chamber are shown in Fig. 3, here the chamber orientation is inverted relative to the bifurcations shown in Fig. 2. Culture medium flows into the inlet reservoir, moves down the parent (vertical) channel, flows into the two daughter channels, into the outlet reservoirs and finally out of the chamber, Fig. 3a. Three separate slide regions are specified on the bottom plate: one in the region of the T-junction (slide I), two in control regions of constant WSS (slides II and III), Fig. 3b. Distinct slide banks are used to decrease contamination of the final biological cells from each test region with those from the transition regions. In addition, cross communication between cells in the different regions will be lessened.

Following [45], we define *Active Test Region*s, ATR-I, ATR-II, ATR-III, where the wall shear stress is within a chosen percentage of the desired 2D flow field for slides I, II and III. For ATR-II and ATR-III, the desired stress field will be a constant, corresponding to the solution for steady, fully developed, 2D, channel flow,

$$\tau_{fd_{2D}} = \frac{6Q\mu}{wh^2} = \frac{4V_0\mu}{h} \tag{12}$$

where Q is the volumetric flow rate, V_0 is the centerline (maximum) velocity, w is the channel width and h is the channel height. It follows from the exact analytic solution for 2D flow that $V_0 = 3Q/(2hw)$. In the bifurcation slide, (slide I), the desired 2D field will correspond to the 2D bifurcation flow field, discussed in more detail below.

In summary, the T-chamber should meet the following criterion:

Design Criteria

1. A 2D WSS and WSSVG field is created on slide I which, with proper choice of flow rates, is relevant to (i) the apex of human cerebral arterial bifurcations and (ii) values for canine models in which pre-aneurysmal changes were reported.

2. Geometry of the flow domain creates nearly constant WSS fields on slides II and III. For example, supra-physiological WSS and physiological stress levels could be created in ATR-II and ATR-III, respectively.

3. The shear stress field should be approximately two dimensional in a large percentage of the chamber. In particular, the width of chamber should be chosen to provide sufficient quantities of cells for meaningful biological analysis in the bifurcation region.

4. The thickness of the daughter channels should be machined to sufficient tolerance to obtain acceptable errors in WSS and WSSVG.

5. The flow chamber should be easily assembled.

6. The total volume of the chamber fluid domain should be minimized to reduce the cost of the testing fluid, chamber body material and lessen the dilution of cellular byproducts.

7. The components of the chamber should be suitable for repeated autoclaving during sterilization.

A variety of perfusion fluids are used in the literature. In general, they have approximately the same properties as water. In other cases, an attempt is made to match the viscosity and density of blood. We take this latter approach and set μ = 0.032 g/(cm s), ρ = 1.02

g/cm^3. These values are within the range reported for normal blood at 37◦C at shear rates higher than 400 s^{-1}, (e.g. [57]). We use these latter values here.

It should be recalled, that the solution (12) is for a 2D channel not a channel with a finite width. An analytic series solution exists for fully developed flow in channels of rectangular cross section and can be used to assess the error in using (12), [45]. The velocity is diminished in a boundary layer near the wall, so that for a given flow rate, the average velocity and WSS will generally be higher outside the boundary layer in the finite channel compared with the idealized 2D solution given in (12). The difference between the WSS outside this boundary layer and that in of the 2D solution can be controlled through the channel geometric ratio $\beta = h/w$, [45]. For the geometries used here, this error is less than 2% and so it is convenient to simply estimate the WSS in slides II and III using (12).

2.3 T-CHAMBER DESIGN—ANALYSIS AND RESULTS

2.3.1 Fluid Domain

A 2D computational analysis was used to select the relevant 2D chamber geometric parameters in Fig. 4a such as the channel heights (h_0, h_1, h_2) and the shape of the bifurcation region. Next, the length of the daughter channel between the bifurcation region and the constant WSS regions $s1$ and $s2$ was chosen to assure the flow is nearly fully developed when it reaches slides II and III. Finally a 3D analysis was performed to design the inlet and outlet reservoirs to diminish the

effects of the fluid entering and exiting the chamber. These reservoirs are essential for obtaining a nearly 2D flow in the test regions. The final design was then checked using a comprehensive CFD study of the full 3D chamber.

Bifurcation Region

Criterion 1 was the central factor in the design of the bifurcation region. The 2D computational domain for these studies was composed of the parent channel, the bifurcation region and symmetric daughter branches of constant height, h_1, Fig. 4a. The modified stress vector $\underline{t}$ was set to zero at the inlet and a parabolic profile with the desired flow rate was specified at each outlet. The FEM mesh was composed of structured quadrilateral elements (between 250 and 500K elements). The WSS distribution on slide I was found to be quite sensitive to the shape of the juncture between the parent and daughter branches (the outer corner of the bifurcation) and the design of this region required the most intense evaluation. A simple sharp corner has been used in a recent T-chamber designs [58]. However, as seen in Fig. 5a below and Fig. 1 of [58], corners of this type can produce standing vortices. The qualitative nature of the WSSVG is altered by these vortices, Fig. 5b. Furthermore, these vortices can potentially be shed and washed downstream, creating additional errors in the imposed WSS and WSSVG fields on the bottom plate. Instabilities of this kind will not be captured in steady simulations.

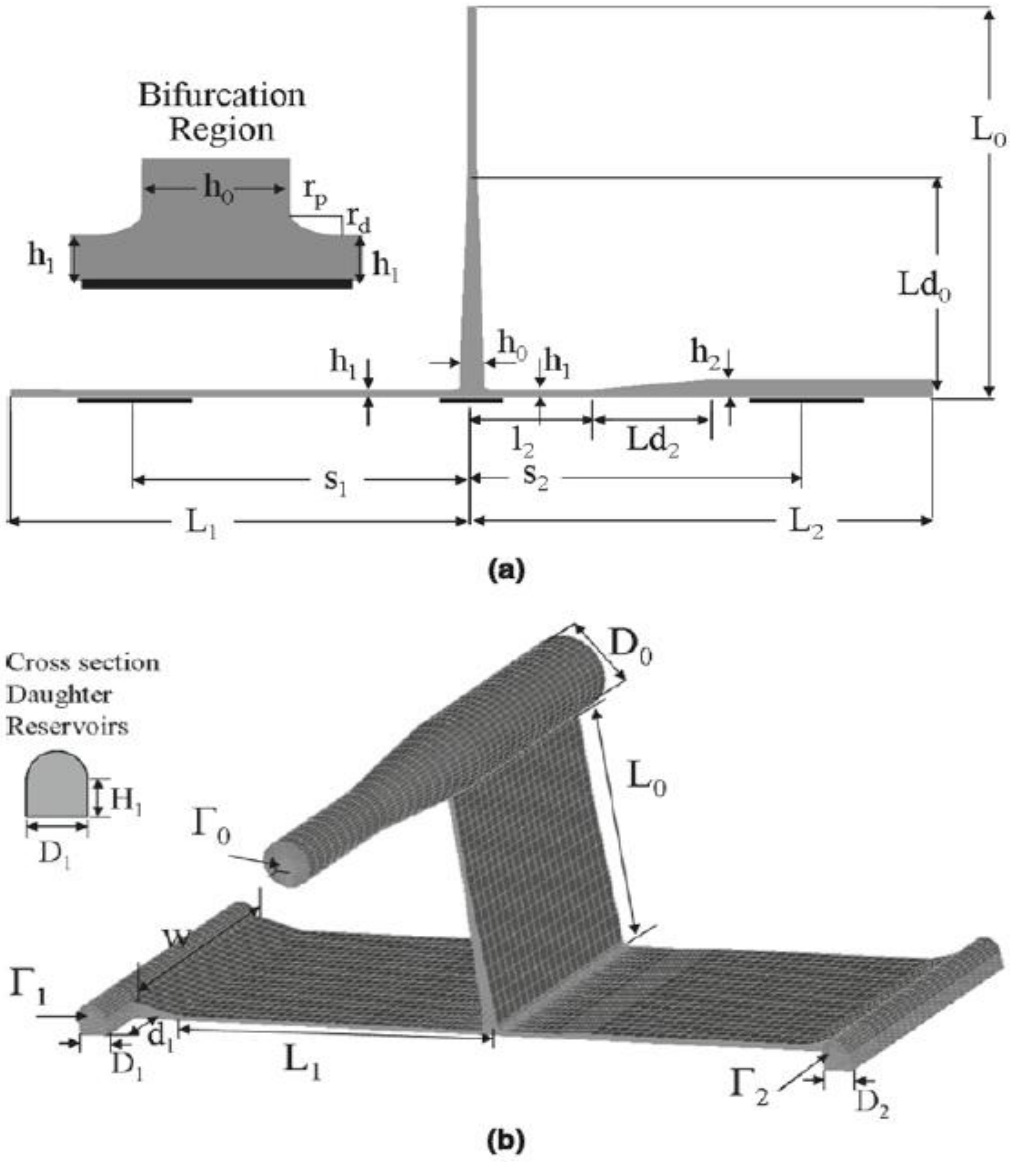

Figure 2.4. Geometric parameters considered in chamber design.

(**a**) 2D domain (no reservoirs), (**b**) full 3D domain

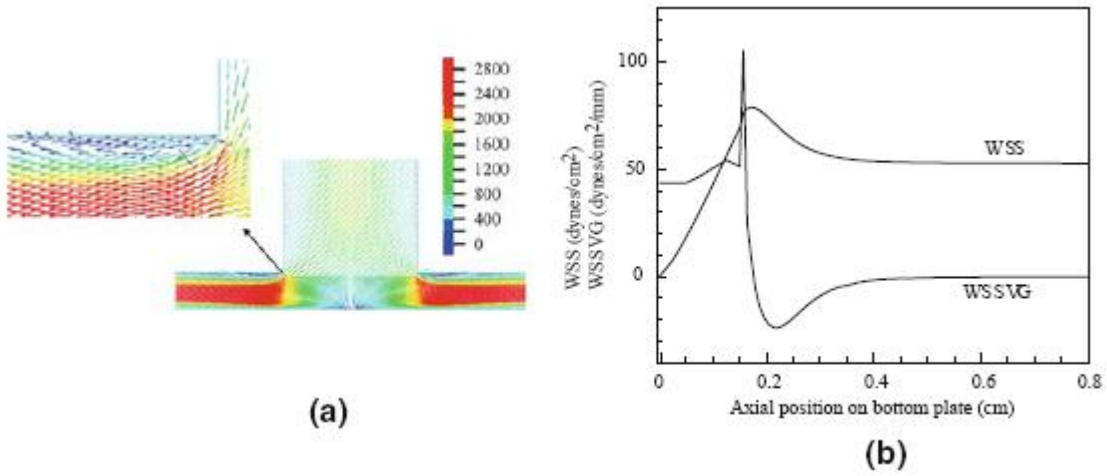

Figure 2.5. Flow through a bifurcation with sharp corners (2D simulation).

In (**a**), velocity vectors in bifurcation region with vortex seen downstream of sharp corner. In (**b**) WSS distribution along centerline of bottom plate in region $x \in [0.0, 0.8]$ cm. Here, Q = 4518 ml/min, [$h0$, $h1$, $h2$] = [1.0, 0.3, 0.3]mm

These vortices can be removed by rounding the sharp corner to form a section of an ellipse, Fig. 6. The elliptical geometry can be characterized by the ellipticity, $\varepsilon = \sqrt{(r_p^2 - r_d^2)/r_p^2}$, where r_p and r_d are the half length of the major axis, Fig. 4a. The original chamber introduced in [6, 7], provided a good match with the WSS distribution in the idealized bifurcation using a circular corner (ε = 0), but there were quantitative differences in the WSS from those reported in [38]. In particular, for the canine model, the maximum in WSS (WSSmax) is found 2–3mm from the bifurcation point, nearly twice the distance of that in the T–chamber with a circular corner. By elongating the circular corner (increasing ε), while holding other variable fixed, the location of the maximum in WSS shifts downstream. This effect can be seen Fig. 7 where 2D solutions for the WSS and WSSVG on the bottom plate are shown for a circular corner (ε = 0) and an elliptical corner with ε increased to $\sqrt{3/2}$. Comparison of Figs. 7 and 8 demonstrates the effect

of increasing flow rate on the WSS and WSSVG profiles. The location where the WSSVG changes sign is relatively insensitive to flow rate, while both WSSmax and WSSVGmax increase with increasing *Q*. As can be seen in Fig. 9, the WSSmax is quite sensitive to the channel height of the daughter branch.

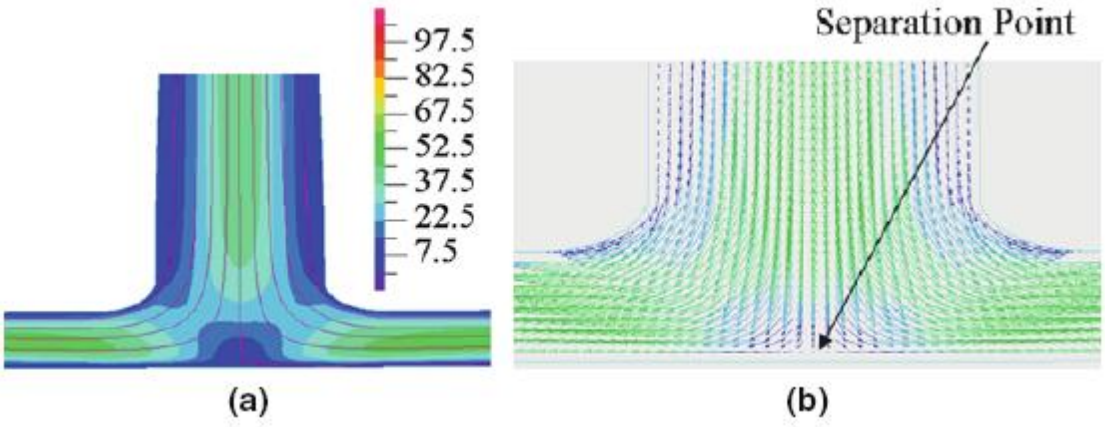

Figure 2.6. Flow through a bifurcation with elliptical corner (2D simulation).

(**a**), magnified view of the bifurcation with streamlines superimposed on iso-velocity contours (mm/s). (**b**), magnified view of velocity vectors in the bifurcation region. Here, Q = 1333 ml/min and geometric parameters are given in Table 1.

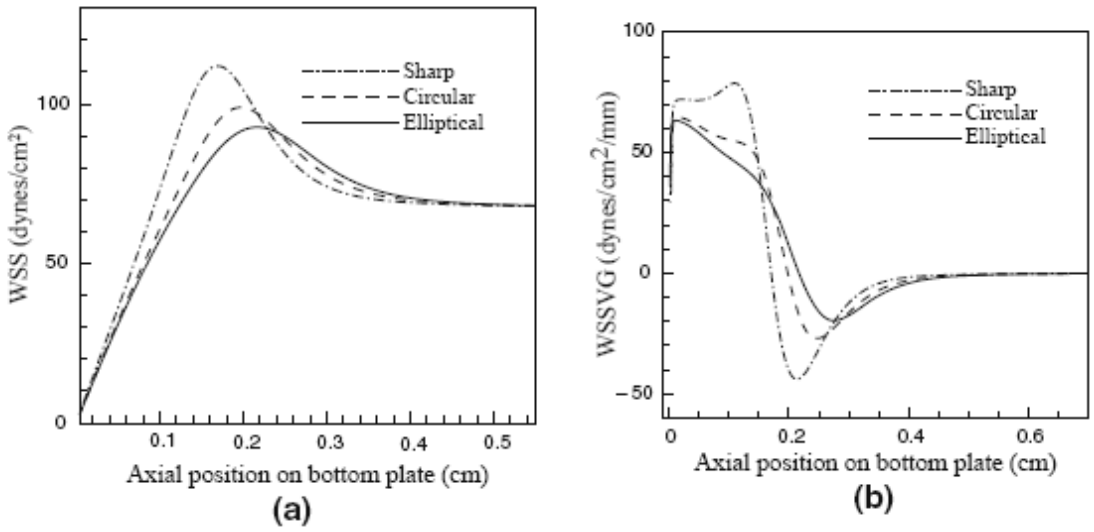

Figure 2.7. Comparison of (a) WSS and (b) WSSVG

On the *bottom plate* of T-chambers with elliptical, circular and sharp corners, (2D simulations) Q = 1333 ml/min, $\varepsilon = \sqrt{3}/2$, Rc = 0.5 mm, with all other geometric parameters given in Table 1.

Table 2.1 Values (in mm) of geometric parameters for T-chamber, Fig.4.

The ellipticity (ε) is $\sqrt{3}/2$, the slide widths (in the flow direction) for slides I, II and III are 15, 25, and 25 mm respectively.

h_0	h_1	h_2	L_1=L_2	w	l_2	Ld_0	Ld_2	s_1= s_1	D_0	D_1= D_2	d_1= d_2
3.0	0.8	1.2	70	48	14	30	7.5	45	16	6	15

As h_1 is narrowed from 0.8 to 0.4mm for fixed h_0, the WSSmax more than doubles with a very slight downstream shift in its location. It was found that by adding a slight taper to the channel upstream of the bifurcation, the magnitude and location of the WSSVGmax could be easily controlled with little change in WSSmax, making it possible to closely match specific WSS and WSSVG profiles.

Using these trends as guidelines, it was possible to select ε, h_0, h_1 and the parent channel taper in such a away to obtain bifurcation WSS and WSSVG values that capture the main quantitative features of a given arterial bifurcation. For example, shown in Fig. 10 is a comparison between WSS and WSSVG profiles for a representative canine data set from [32] and results from a T-chamber model, designed to obtain a quantitative match of this data.

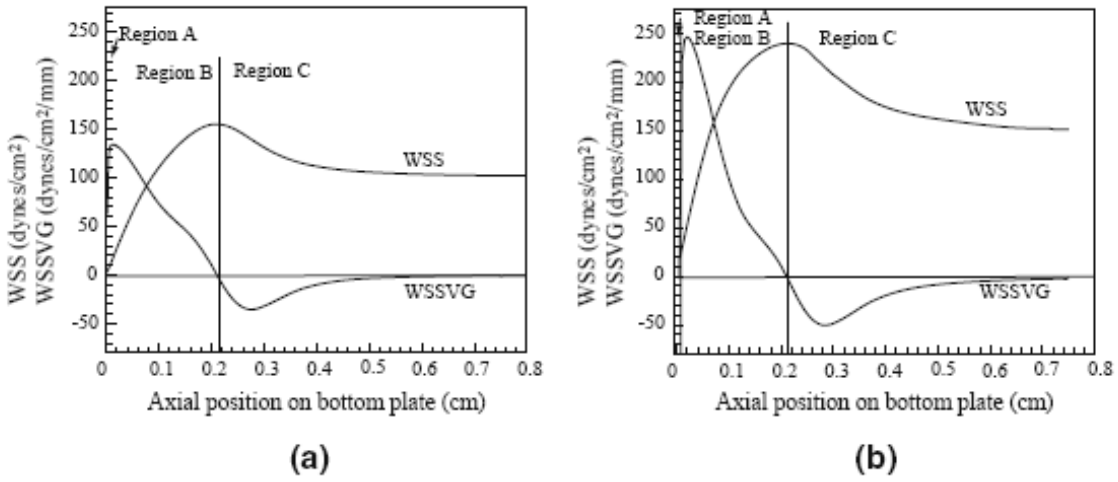

Figure 2.8. WSS and WSSVG distribution along *centerline* of bottom plate in bifurcation region.

2D simulations with elliptical outer bifurcation $\varepsilon = \sqrt{3}/2$, h_0, h_1, h_2 = [3.0, 0.8, 1.2] mm and all other geometric parameters given in Table 1. Two flowrates are considered: (**a**) Q = 2000 ml/min, (**b**) Q = 2400 ml/min. Region A is defined by WSS $\leq$ 20 dynes/cm^2, Region B by WSS > 20 dynes/cm^2 and positive WSSVG and Region C by WSS > 20 dynes/cm^2 and negative WSSVG

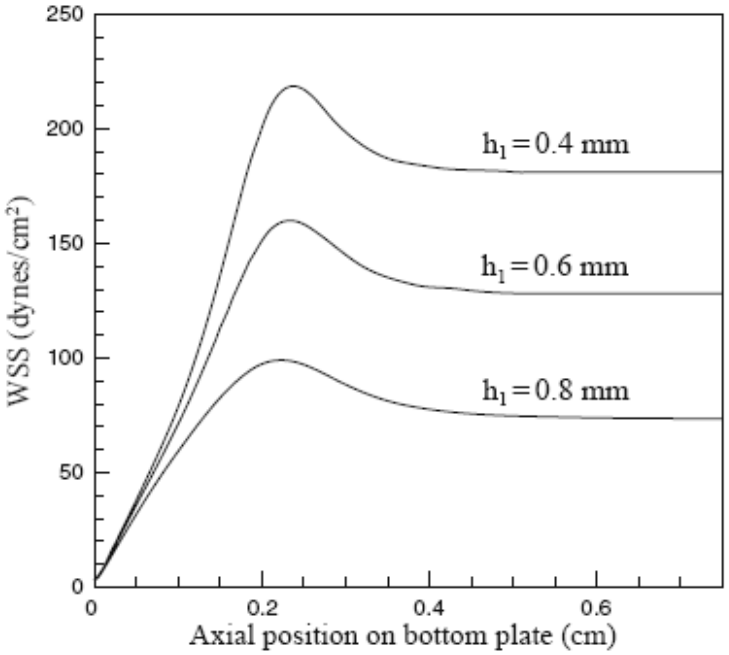

Figure 2.9. WSS distribution along *centerline* of bottom plate in bifurcation region

For h_1 = [0.4, 0.6, 0.8] mm, (2D simulations) with elliptical outer bifurcation $\varepsilon = \sqrt{3}/2$, Q = 1333 ml/min. All other geometric parameters are given in Table 1

Test region II and III

The chambers are designed to be run with an equal flow split between the two daughter branches. This ensures the flow in the bifurcation region is nearly symmetric about the plane x = 0. In this case, the flow rate in each daughter channel is $Q_d = Q/2$. The transition regions between slides I and the slides in the daughter branches are designed to achieve nearly fully developed flow prior to slides II and III. Assuming the flow is approximately 2D, the WSS on each daughter slide can then be calculated directly from (12). A 2D CFD analysis was performed to select the geometry of the diffuser and slide location that would guarantee the flow to be nearly fully developed on both slides. Values for the current chamber are shown in Table 1.

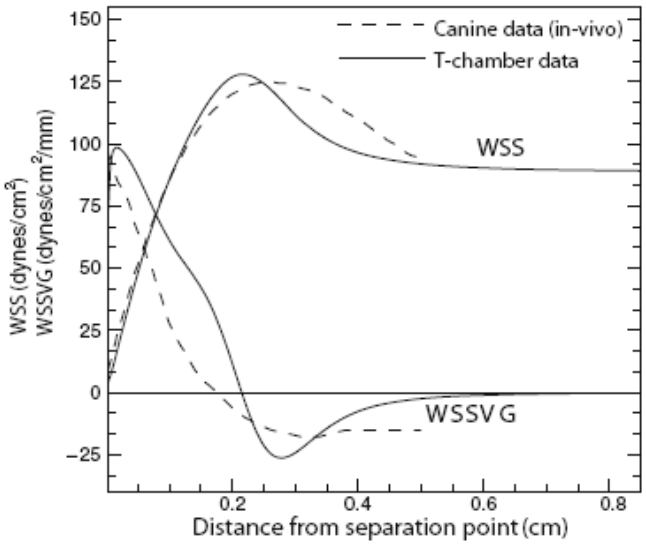

Figure 2.10. WSS and WSSVG profiles in bifurcation region of canine model and T-chamber.

T-chamber flowrate and geometry chosen to approximate maximum in WSS and WSSVG in canine data as well as qualitative shapes of curves. In T-chamber study L_{d0} = 18mm and Q = 1750 ml/min, (2D simulations). All other geometric parameters are given in Table 1.

2.3.2 Reservoir Design

As discussed in detail in [45], the size of the ATR is influenced by the magnitude of the lateral wall effects as well as entrance and exit effects. While simply increasing the length of the chamber segments upstream of the test regions will generally lead to a more 2D flow it will also increase the volume of perfusion fluid. The cellular byproducts of the cells in the chamber are sometimes evaluated from samples of the perfusion fluid obtained during experiments [59]. By decreasing the volume of fluid, the cost of the experiment can be decreased and it will be possible to obtain higher concentrations of these materials.

Parametric studies were performed to design the shape and size of the reservoirs and diffusers for the parent and daughter channels. The 3D computational domain for these studies consisted of the inlet/exit to the reservoir, the inlet/daughter reservoir and the adjacent parent/daughter channel, Fig. 4b. A uniform velocity profile was applied at the inlet/outlet of the computational domain and the modified traction vector was set to zero at the outlet/inlet. The width of the channel was set to 48 mm to provide a large quantity of slides for cell culture while matching readily available slip cover and slide lengths.

The inlet reservoirs decreased the incoming momentum of the flow from the tubing and help to redistribute it across the width of the chamber, thereby contributing to the 2D nature of the flow. The shape of the reservoir has a significant impact on its effectiveness. Following [45], we chose cylindrical reservoirs with incoming flow perpendicular to the flow direction in the neighboring channel, Fig. 4b. For the inlet flow, a reservoir of circular cross section with D_0 = 16 mm was found to provide a good balance between damping effects and volume requirements. The reservoir design was found to be very effective at damping the momentum of the flow entering the inlet reservoir thereby diminishing the length of the parent channel needed to ensure the flow is nearly 2D in the test regions. Figure 11a displays the iso-velocity (magnitude) contours in the symmetry plane (x = 0) of the inlet reservoir and parent channel. The damping of the inlet jet can be seen within the reservoir. The diffuser effectively converts the incoming jet to a nearly 2D flow, a short distance downstream of the diffuser.

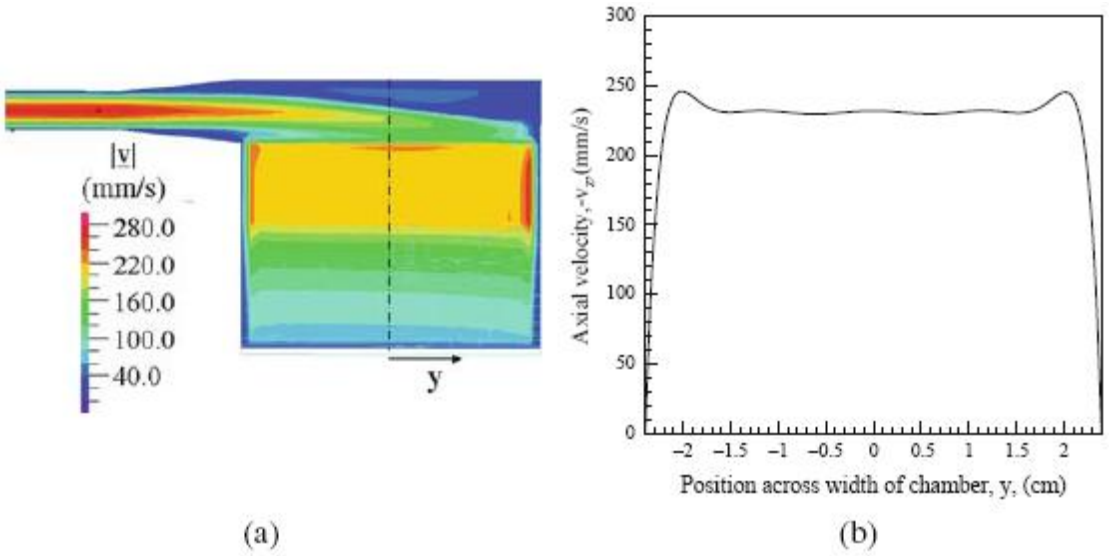

Figure 2.11. Evaluation of transition to fully developed flow in parent channel

3D simulations with (**a**) iso-velocity contours in yz-plane (mm/s) and (**b**) axial velocity ($-v_z$) as a function of *y* just upstream of bifurcation slide (x = 0, z = 36 mm), with Q = 1333 ml/min, [h_0, h_1, h_2] = [3.0, 0.8, 1.2]mm and all other geometric parameters are given in Table 1. Coordinate system show in Fig. 3

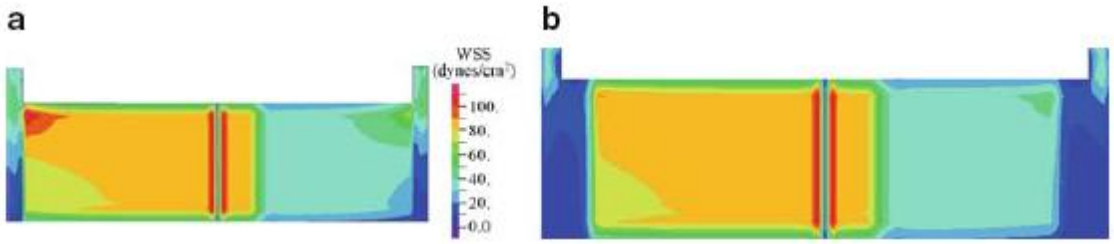

Figure 2.12. WSS (dynes/cm^2) contours on *bottom surface* of flow domain.

3D simulation for chamber (**a**) without diffusers and (**b**) with diffusers at outlet reservoirs. Geometric parameters are given in Table 1 and Q = 2000 ml/min

There are two slight modifications in this inlet reservoir design from that in [45]. In the earlier chamber, a constant radius extension of the reservoir was used on both sides of the channel. Here, the constant radius inlet extension was replaced by a diffuser. The opposing extension on the inlet reservoir was found to have little impact on the flow and was removed in the current chamber.

The addition of two outlet diffusers upstream of the daughter reservoirs was found to significantly lessen the upstream influence of the reservoirs, Fig. 12. These reservoirs were designed independently from the parent reservoir and, for simplicity, were chosen to be identical. The cross section shape of is the union of a half circle of diameter D_1 and a rectangle of height H_1, Fig. 4b. The value of the geometric parameters used in the final chamber design are given in Table 1.

The fluid domain can potentially be reduced in volume by decreasing the reservoir and channel volumes. Careful design of the reservoirs was used to diminish the entrance and exit lengths of the neighboring flow and therefore the lengths (and volume) of each channel. It was found that a region in the parent branch adjacent to the inlet reservoir could be narrowed to a thickness $h_p = 1/3 h_0$ and then gradually expanded over a length L_{d0} to the desired value of h_0, Fig. 4a. Due to the gradual nature of the taper, these alteration to the parent channel had no measurable effect on the velocity field, WSS, or WSSVG in the bifurcation region. Values chosen for this chamber are given in Table 1. The total chamber volume is 25.8ml.

2.3.3 Validation of T-chamber Design

The design of the various sections of the chamber were performed for subsets of the entire final chamber geometry. It was therefore necessary to perform a 3D analysis for the full 3D chamber, including the inlet port and reservoirs. This corresponds to the complete computational domain

shown in Fig. 4b using the geometric parameters in Table 1. A uniform velocity profile corresponding to the flow rate Q_d was prescribed at each of the outlets (Γ_1, Γ_2) to ensure equal flow division. The modified traction vector was set to zero at the inlet, Γ_1. Approximately 70K structured hexahedral elements were used for these 3D studies. The results of this validation study are shown in Figs. 13 and 14. The WSS on the bottom plate and reservoirs is shown in Fig. 13. The boundaries of ATR-II and III based on a criterion that the WSS be within 10% of the desired 2D value are drawn. The slide locations are drawn in solid lines with the lateral boundaries of the ATR drawn as dashed lines. The slide widths in the direction of flow are 15, 25 and 25mm for slides I, II and III, respectively. For studies with Q = 1333 ml/min, the desired WSS values in ATR-II and ATR-III, are 70 dynes/cm^2 and 31 dynes/cm^2, respectively. Due to the no-slip condition at the lateral walls, there is a boundary layer where the WSS differs substantially from the 2D value. Conservatively, a domain excluding a 3mm wide strip on each lateral side of the slides will satisfy the ATR criterion. Shown in Fig. 13 are the slide regions, all within the appropriate ATR. Necessarily, the slide must extend beyond the lateral boundaries of the ATR. This can be addressed either by removing these cells from the slide after testing and prior to genetic analysis, or by bounding the domain occupied by the cells (see, e.g. [60]). The effect of varying the flow rate on the WSS distribution on the bottom surface of the final flow chamber (geometric parameters in Table 1), is shown in Fig. 14. The three slides can be seen to be well located for all three flow rates tested.

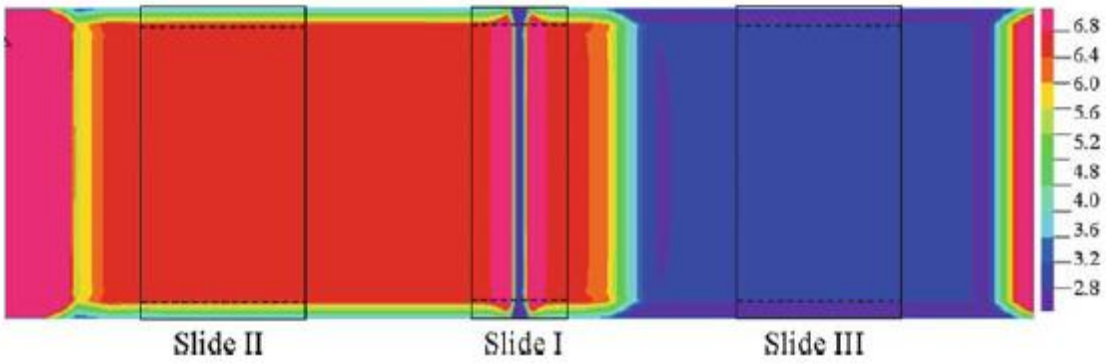

Figure 2.13. WSS (dynes/cm^2) contours on bottom surface of flow domain, with labeled slide regions. 3D simulation, geometric parameters are given in Table 1 and Q = 1333 ml/min

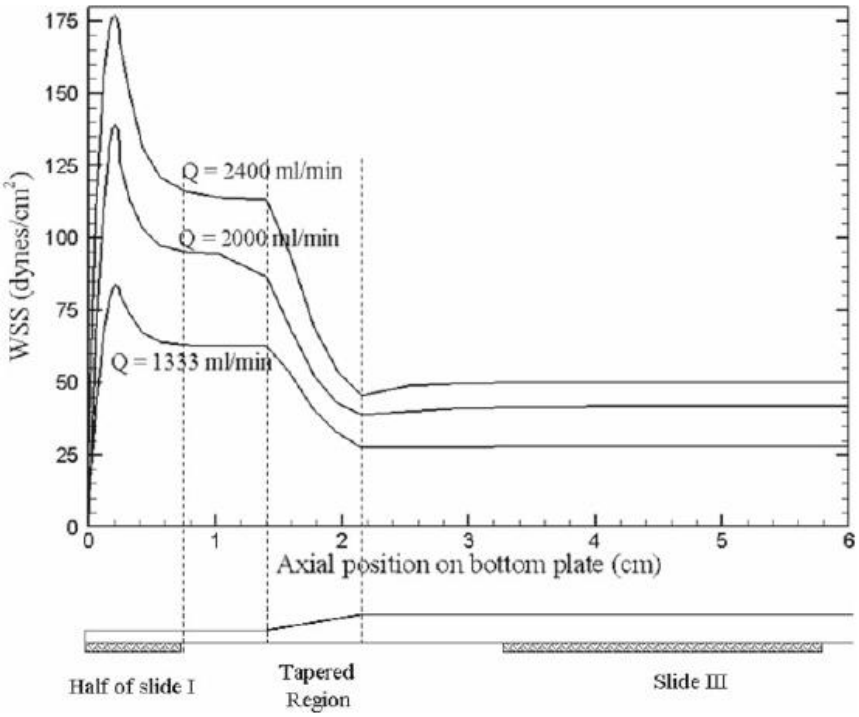

Figure 2.14. WSS (dynes/cm^2) along centerline of *bottom plate* for flowrates, Q = [1333, 2000, 2400] ml/min with the geometry given in Table 1

When the chamber is placed within a flow loop for testing, the flow division can be controlled by downstream flow regulators. 2D CFD studies were performed to investigate the possible impact of imbalances in this split. Shown in Fig. 15 are results of a conservative study, in which a deviation of ±10% from the desired value was imposed. While the change in flow magnitude is reflected in the magnitude of the WSS, it is clear that the locations of both the impingement point and the maximum in WSS are nearly insensitive to an imbalance of this magnitude. Therefore, the interpretation of the three regions within slide I will not be jeopardized if an experimental error of this kind is introduced.

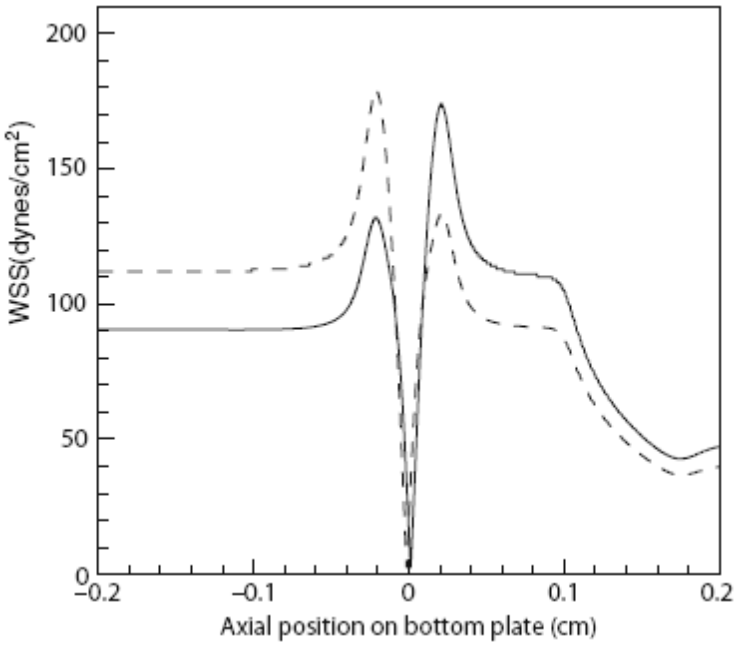

Figure 2.15. Evaluation of the effect of a flow imbalance relative to a balanced flow $Q_1 = Q_2 = Q_n$.

WSS along the bottom plate for imbalances (Q_1, Q_2) = (1.1, 0.9) Q_n (*solid line*) and (Q_1, Q_2) = (0.9, 1.1) Q_n (*dashed line*). Geometric parameters are given in Table 1 and Q_n = 1000 ml/min

2.4 ASSEMBLY DESIGN AND MANUFACTURE

The 3D assembly design of the flow chamber is shown in Fig. 16a, generated using Pro/ENGINEER Wildfire package (PTC Inc). The entire chamber is composed of four plates which we denote as A, B, C, D from the top to bottom in Fig. 16(a) and an inlet adaptor. The breakdown of the upper chamber into three layers was necessary for precise machining of the parent channel which has a very high aspect ratio ($w/h_0 = 16$, $w/h_{in} = 48$) and two different cross sectional shapes (constant and tapered).Machining of this channel through layers A,B,C was the most demanding aspect of the manufacturing process. The daughter branches, daughter diffusers and daughter reservoirs were machined from the underside of Plate C. These three plates were cut to a tolerance of ±0.002in (0.051 mm) using CNC milling (Atlantic Diecasting, NY). The inlet reservoir of diameter D_0 was drilled in the top piece. The slide slots were machined to a tolerance of ±0.003in (0.076 mm) on the upper side of layer D using CNC milling (Swanson School of Engineering, University of Pittsburgh), Fig. 16a, b. These slots were custom cut to fit the slides to minimize any change in height along the bottom boundary of the fluid domain. Standard AS-568A o-rings were used to seal all sections of the T-chamber, Fig. 16a. The o-rings were chosen to have 20–30% compression to ensure a positive seal while still allowing the mating pieces to properly seat against each other. Precision ground alignment pins were used to assure proper alignment of the pieces during assembly. They were placed at opposite corners of the parts, which is sufficient for alignment on a plane. Another critical aspect of the design was the decision to avoid any glued parts which could cause warping during autoclaving or potentially leak contaminants into the test chamber. Instead, the pieces were held together by stainless steel, standard hex, quarter 20 (1/4–20in) bolts (McMaster), Fig. 16c. Polysulfone was

chosen for the chamber material due to its easy machinability and its ability to withstand autoclave conditions (120◦C, 15 psi, 30 min). The final manufactured T-chamber is shown in Fig. 16c. Significantly, the tolerance for the channel heights h_0, h_1, h_2 are all set by the machining tolerances. This is in contrast to the use of gaskets to set the height in some channels.

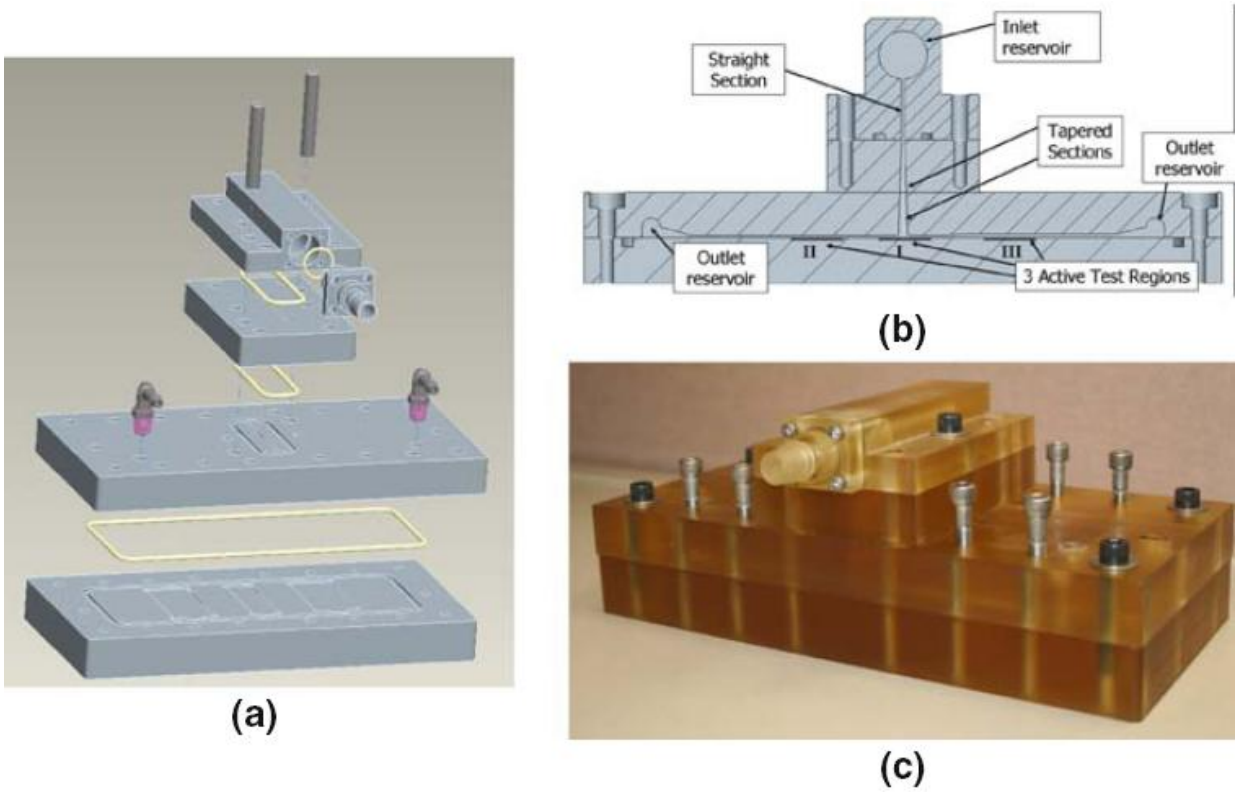

Figure 2.16. (a) Exploded view of final T-chamber assembly design. (b) Cross section view of assembly design of flow chamber. (c) Photograph of manufactured T-chamber

2.5 DISSCUSSION

Cerebral aneurysms typically form at the apex region of arterial bifurcations. Hemodynamic stresses are believed to play an important role in the initiation of this pathology. Recent work in a

canine model identified an association between aneurismal changes and a combination of elevated WSS and WSSVG in bifurcations formed from a naive vessel. This study was the first to connect in vivo histological changes with specific WSS and WSSVG profiles. The flow chamber designed here provides a tool for exploring these results in a controlled setting. Most studies of endothelial cell response to mechanical stresses have been motivated by a desire to better understand the role of hemodynamics in the genesis and development of atherosclerosis. A number of researchers have developed in vitro chambers to evaluate the response of cellular components of the arterial wall (e.g. endothelial and smooth muscle cells) to homogeneous stress fields or recirculating flow fields of the type associated with atherosclerotic plaque formation. In early work in this field, DePaola et al., designed a step flow chamber which created a recirculating region [61]. At the edge of this region, the flow impinges on the wall and then separates – part of the flow circulating backward toward the step and the remainder moving downstream. However, the magnitude of the WSS and WSSVG fields in this flow are much smaller than those associated with aneurysm formation. Recent work by Dolan et al. showed different EC response to positive or negative WSSG under the high WSS condition using a parallel flow chamber with varying the dimensions of the flow domain. The flow chamber captured part of the WSS and WSSG profile presented in Fig.2.10. They conjectured that EC responses to positive WSSG may contribute to pathogenic remodeling that correlate to the aneurysm initiation at arterial bifurcations [62].

In this work, we have used parametric CFD studies to design a T-chamber capable of reproducing the qualitative and quantitative features of the WSS and WSSVG fields studied in [32]. The geometry of the flow domain was chosen using 2D and 3D CFD analyses. Building on

earlier work for a parallel plate flow chamber [45] and the work in [41], the magnitude of entrance and exit effects were controlled through careful design of chamber reservoirs. A full 3D analysis including all chambers was used to validate the final design. The chamber material was chosen for its easy machinability and its capability to withstand the high temperatures necessary for standard sterilization procedures. To our knowledge, three previous T-chambers have been constructed [41, 58, 63]. The current chamber builds on that in [41] with several principal changes. It is capable of generating a good approximating of both the WSS and WSSVG fields reported in [32, 46] and conjectured to lead to pre-aneurysmal changes. Secondly, an elliptical rather than circular corner is used at the bifurcation in order to shift the maximum in WSS further away from the impingement point. Thirdly, the chamber is designed so that it does not require any adhesives which could impact the cellular response. As in [41, 45], the height of the chamber is machined into the plates, and is not set by the width of a gasket as has been done in some earlier chambers. Several features distinguish this T-chamber from that in [58] including (i) the use of inlet and outlet reservoirs to diminish entrance and exit effects, (ii) confinement of wall effects to less than 5% of the chamber width, (iii) avoidance of vortex formation in the bifurcation region, and (iv) the use of three separate test regions for built in controls. Both T-chambers are directed at obtaining nearly 2D flow in the test regions (approximately independent of y, Fig. 3). This is particularly import due to inter-endothelial cell communication which is known to occur through both humoral exchange and via gap junctions. Furthermore, if the cells are to be removed from the slides for later analysis, the cells outside the ATR will contaminate the data. The effects of the entrance flow, exit flow and walls preclude complete 2D flow in the slide regions. Fortunately, the lateral wall effects can be diminished by lowering the aspect ratio of the chamber. A boundary layer thickness defined by a WSS less than 90% of the centerline

value can be estimated from the exact solution for fully developed flow in a channel [45]. For the current chamber, β (the channel thickness to width ratio) is quite small: 0.017, 0.025 and 0.0625 in the daughter and parent branches with a corresponding boundary layer thickness of 4.2% or less of the chamber width. However, for a parent value of $\beta = 0.15$ such as is found in [58], the boundary layer on each side of the channel will rise to nearly 10% of the chamber width. The effect can be even more dramatic in the non-monotonic region at the apex, (e.g. Fig. 2 of [58]). The reservoirs significantly diminish the effect of the inlet and outlet flow for the chamber. The absence of reservoirs can result in large entrance and exit lengths which cannot be predicted by simple boundary layer theory [45, 64]. The chamber used in [58] does not employ reservoirs. The inlets and outlets were omitted from the CFD analysis in [58], so the impact of this design choice is not known. Many tests of cell functionality provide only a relative measure of a particular response. To address this issue, we have included two control sections within the T-chamber. In the current chamber, the control flows are for a WSS of two different magnitudes. By switching out the bottom plate it is possible to change these controls. Other control flows of interest include flow over a backward facing step and constant WSSVG flows.

The apex region of the current chamber was carefully designed to avoid generating vortices at the outer walls of the bifurcation. Even for steady flows, these vortices will change the WSS profile on the bottom plate [58]. Clearly this will be even more problematic if the vortices become unstable and are washed downstream. A variety of WSSG definitions are used in the literature, unfortunately confounding comparison of results from different groups. As in this work, several researchers consider the $\underline{G}$ = grad*s* $\underline{ts}$ to be of primary importance, (e.g. [25, 65, 66]). In these works, an orthogonal surface basis composed of a unit vector in the time

averaged direction of *ts* (for a cardiac cycle) and its perpendicular component are introduced. The WSSG is then defined as the square root of the sum of the squares of the diagonal elements of $\underline{G}$ using this basis. In contrast in [54], $\underline{G}$ is replaced with the 3D gradient of the full stress vector *t*. For both these definitions, a non-negative quantity is used for the WSSG. In [67], the WSSG was approximated by the change in WSS divided by the change in axial position. In other works, particularly those with 2D flows in mind, the WSSG is not clearly defined. The variation in definitions may be one reason why groups have reported different correlations between biological markers for intimal hyperplasia and WSSG.

In this work, we have introduced a new measure of the gradient of the wall shear stress, denoted as WSSVG to distinguish it from these definitions of WSSG and to emphasize that it is not a measure of the gradient of WSS. We feel the WSSVG definition (7) has some advantages. It differentiates between increasing and decreasing shear stress through the sign of the WSSVG. It has been shown to be a scalar invariant of grad*s* $\underline{t_s}$ and it does not require calculation of the time averaged direction of WSS a priori. These last two points will become important if the WSSVG is to be incorporated into constitutive equations of the arterial wall, for example, to capture destructive remodeling during aneurysm formation [52]. Furthermore, when the definition (7) is specialized to 2D flows over a flat surface, the sign of the gradient enters in a physically meaningful way.

In the future, it may be of interest to use this chamber for unsteady flows. In preliminary studies, we have found little difference between WSS and WSSVG results for steady simulations and the corresponding time averaged values for unsteady simulations using the same time

averaged flow rates. It will also be useful to study the cellular response in real time. Modifications can be made to the bottom plate to achieve this objective.

3.0 HEMODYNAMICS IN ELASTASE-INDUCED RABBIT ANEURYSM MODELS

3.1 SENSITIVITY OF CFD BASED HEMODYNAMIC RESULTS IN RABBIT ANEURYSM MODELS TO IDEALIZATIONS IN SURROUNDING VASCULATURE

3.1.1 Background and Purpose

In order to better understand the pathophysiology of cerebral aneurysms and design effective clinical treatments to enhance the likelihood of stabilization, it is necessary to evaluate the in vivo response of the aneurysm wall to intra-aneurysmal hemodynamic stresses. A number of animal models have been created for studying aneurysm pathogenesis [68-70]. One such animal model is an elastase induced aneurysm model in rabbits [71]. In this model, saccular aneurysms are created by elastase infusion in, and distal ligation of, the right common carotid artery (RCCA). This model has been used to evaluate the performance of endovascular devices and evaluate changes in histology after device implantation [15-18]. The rabbit model has also been used to study the correlation of altered expression of extracellular matrix and vascular remodeling molecules with areas of low shear [31, 72]. To better understand the coupling between hemodynamics and biological response within aneurysms and to evaluate flow devices, accurate estimates of flow in and around the model aneurysms are needed. The relationship

between the flow field, resulting hemodynamic factors in the aneurysm cavity, and associated vascular morphology can then be confidently investigated.

By using high quality CT, MRI, or 3D angiographic images, case-specific CFD models can be constructed and used to obtain estimates of detailed flow characteristics in the cerebral vasculature [7-10, 30]. To construct the computational model, a certain vascular domain around the aneurysm site must be selected and proper boundary conditions applied. However, aneurysms are usually associated with complex arterial anatomy, and the extent of the surrounding vasculature that should be included in CFD models to optimize flow estimates remains unknown. Inclusion of surrounding vessels that do not impact estimated flow will result in needless computational effort, while exclusion of vessels that would alter flow estimates will degrade the accuracy of CFD results. For elastase induced aneurysms at the RCCA [73], up-stream and down-stream bifurcations are in close proximity to the aneurysm cavity, Fig. 3.1. For this type of model aneurysm, casual selection of the extent of the model geometry may lead to unreliable local CFD results in and around the aneurysm cavity or, conversely to consumption of excessive computational resources.

The central goal of this work is to study how the computed hemodynamic factors within the aneurysm cavity change as a result of varying the complexity and extent of the nearby vasculature. In this study, we evaluate the sensitivity of the hemodynamics to extent of vasculature using CFD outputs for various parent artery anatomies. We include two specific aneurysm morphologies - low and high aspect ratio (AR, the ratio of aneurysm height to neck width) aneurysms, considered by many investigators to be at different risk for spontaneous

rupture [43, 74-76]. We apply five separate models of up and downstream anatomies to these two aneurysm geometries. Quantitative and qualitative analysis of changes in estimated intra-aneurysmal hemodynamics as a function of peri-aneurysm anatomy offer insight into the sensitivity of CFD outputs to different choices of computational domain.

3.1.2 Materials and Methods

Aneurysm Creation

Saccular aneurysms were created in New Zealand white rabbits (body weight, 3–4 kg) by our collaborators in Mayo clinic using a previously reported protocol. Briefly, using a balloon catheter, porcine elastase (Worthington Biochemical Corporation, NJ) was incubated within the lumen of the proximal RCCA for 20 min, after which the balloon was deflated and catheter system was removed. The RCCA was then ligated at its mid-portion. Dilated, arterial segments thus formed from the stump of the RCCA, are termed "aneurysms" for the purpose of this work [77, 78].

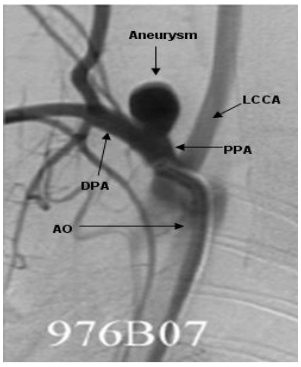

Figure 3.1 2D anteroposterior subclavian artery angiogram with arrows indicating the surrounding vasculature. (Left common carotid artery (LCCA), proximal parent artery [79], distal parent artery (DPA), aortic arch (AO) and aneurysm.)

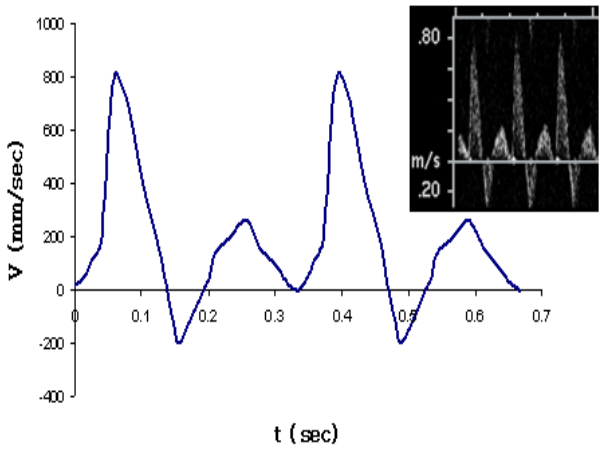

Figure 3.2 Raw Doppler velocimetry waveform (upper right) and corresponding idealized waveform used in computational studies (case 976)

Imaging Procedure and Data Acquisition

Images of 3D vasculature were taken in the Mayo clinic. Three-dimensional rotational angiography (3DRA) was performed 12 weeks after aneurysm creation and used to construct 3D models of the interior surface of the vasculature using a commercial package (Mimics; Materialise). Briefly, after femoral artery cut down and sheath placement, a 5Fr catheter was placed into the aortic arch. During infusion of iodinated contrast, 3DRA was performed. In a separate setting, transthoracic Duplex Doppler ultrasound imaging (ACUSON Sequoia 512 machine with a 15L8 transducer, Siemens Medical Solutions) was performed for these same aneurysms and arterial waveforms (Fig. 3.2) were obtained within distal parent arteries (DPA) and left common carotid arteries (LCCA).

Anatomical Models

The 3DRA data was used to construct 3D models of the interior surface of the vasculature using a commercial package (Mimics; Materialise). Geometric measurements including aneurysm height (H: distance from neck cross section to aneurysm apex), neck width (N: hydraulic diameter of neck cross section) and aneurysm diameter (D: largest hydraulic diameter along the centerline of the aneurysm sac) were taken from the 3D reconstructed models. A 3D reconstruction of the complete set of vessels considered for the high AR case (AR=2.1) is shown in Fig. 3.3. The structure of the neighboring vessels for the low AR case (AR=1.0) is similar to that shown in Fig. 3.3 with the exception that the distal trifurcation is replaced by a quadrification for the low AR model. For both the low and high AR cases, models of four distinct vascular subregions denoted as Models A, B, C, D and E were created in order to explore the importance of the various vessels surrounding the aneurysm (Table 3.1). Model A is the smallest subregion including only the aneurysm, PPA, and DPA. Model B includes the LCCA in addition to the Model A vessels. Model C is composed of the Model B vessels and the aortic arch. Model D includes the distal trifurcation (quadrification in the low AR case) as well as the Model B vessels. Model E is the most complete model consisting of the Model D geometry and the aortic arch and is used as the reference model. To evaluate the role of vessel extensions, four variations of Model A were considered denoted A_1-A_4 (Table 3.1). Model A_1 consists of the native aneurysm, PPA and DPA. Models A_2, A_3, A_4 are composed of the submodel A_1 as well as straight vessel extensions of the PPA, DPA, both PPA and DPA, respectively. The extensions have the same cross sectional shape as the native vessel at the corresponding surfaces of A_1, with length three times the effective diameter. This length was chosen because of the invariance in

results to longer extensions. In order to generate a structured brick element mesh in Models B and D, it was necessary to add a half diameter length extension proximal to Γ_4 of these models.

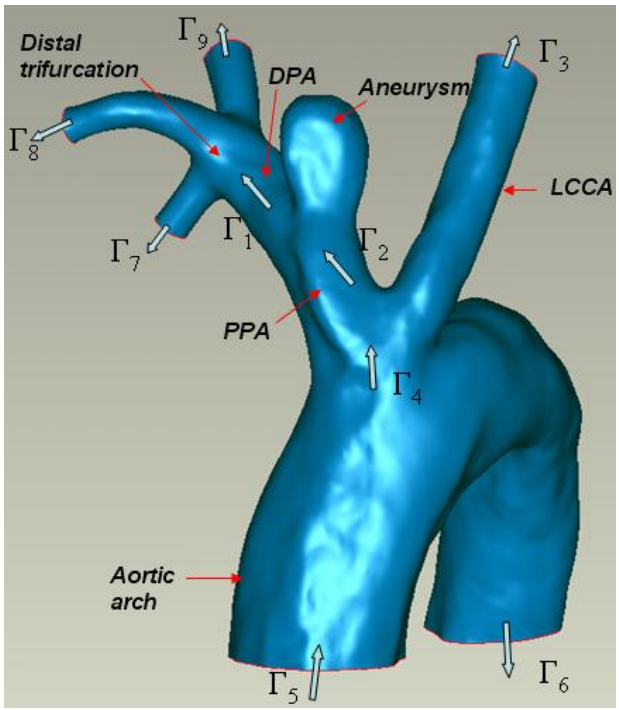

Figure 3.3 3D reconstruction of vascular domain used for high AR Model E; inlet/outlet cross sections for Model E and various submodels are labeled as $\boldsymbol{\Gamma_\alpha}$

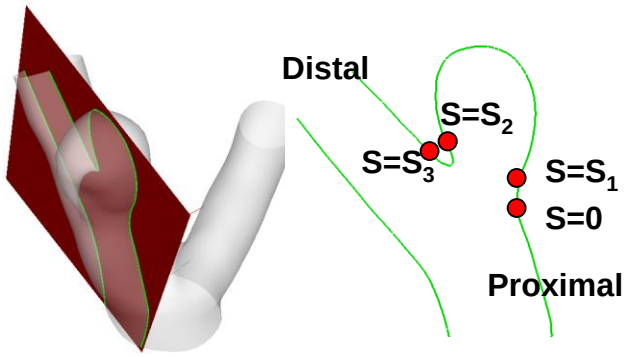

Figure 3.4 Schematic view of intersecting plane used for error analysis, the cross section plane (left), and the resulting intersecting curve (right).

Table 3.1 Model geometry and computational domains for high AR (upper row) and low AR (lower row) cases. (Arrows indicate the flow directions; $\boldsymbol{\Gamma_\alpha}$indicate different computational domain boundaries.)

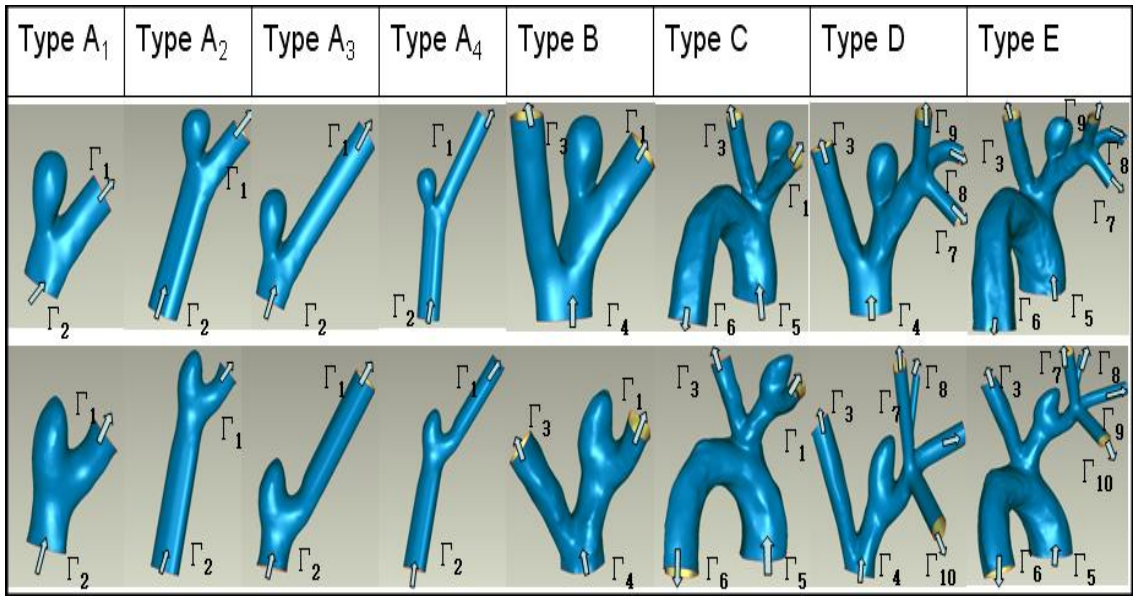

Computational Fluid Dynamic (CFD) Analysis

Blood flow in the reconstructed models was simulated based on the unsteady, 3D Navier-Stokes equations, using the finite element method with ADINA software (64 bit) (ADINA Inc.). The blood was modeled as a Newtonian fluid with constant density and viscosity chosen as ρ = 1050 kg/m^3 and μ = 3.5 mPa·s, respectively. The time varying boundary conditions on the computational domain are given below. To attain highly accurate computational results, the finite element mesh was composed of hexahedral (brick) elements. The mesh density was chosen such that the change in maximum WSS upon doubling the flow direction density was less than 3%. The resulting number of elements ranged from 15,000 to 85,000 in the various models. A study was done for a representative model using 6 cardiac cycles to evaluate the variations of pulsatile

flow results among each cycle. Upon comparison of numeric values (up to 6 decimal digits) of velocity components (U, V, W) at the same mesh point during cycles 2 to 6, no difference was found at the same cardiac time point (same time step point in each cycle) for different cycles. Thus, CFD analyses were performed for each model for a period of two cardiac cycles using 100 time steps per cycle. Simulations were done using a 3-GHz dual Xeon processor work station with 4-GB of memory (upgraded to 8-GB for Model E).

Boundary conditions

The vessel wall was idealized as rigid and the no-slip boundary condition was applied to the walls of all models. In this work, three types of inlet and outlet conditions were applied at surfaces labeled Γ_1-Γ_{10} in Fig. 3.3 and Tables 3.1-2.

Table 3.2 Inflow and outflow conditions used in computational studies; FOW denotes "first order Womersley" velocity profile, MT denotes "modified traction" condition, TVU stands for "time varying uniform" velocity profile

	Γ_1	Γ_2	Γ_3	Γ_4	Γ_5	Γ_6	Γ_7	Γ_8	Γ_9	Γ_{10}
Model A	FOW	MT	--	--	--	--	--	--	--	--
Model B	FOW	--	FOW	MT	--	--	--	--	--	--
Model C	FOW	--	FOW	--	TVU	MT	--	--	--	--
Model D	--	--	FOW	MT	--	--	TVU	TVU	TVU	TVU (low AR)
Model E	--	--	FOW	--	TVU	MT	TVU	TVU	TVU	TVU (low AR)

We approximate the velocity field at the outlet of a number of the vessels (boundaries Γ_1 and Γ_3) with a first order Womersley approximation (FOW), implemented using a bi-quadratic function with velocity specified at surface vertex and mid/internal grid points (implemented in ADINA spatial functions). The FOW is the pulsatile velocity field corresponding to a steady plus first order term (fundamental frequency) of the exact solution for fully developed, pulsatile flow in a straight pipe of circular cross section (e.g, [80]). It is mapped to the non-circular vessel cross section. From the intravascular duplex doppler measurements at boundaries Γ_1 and Γ_3, the shape of pulsatile waveform was noted to be similar in each model, although the magnitude differed. For this reason, a standard time varying shape was used and an animal specific maximum velocity was chosen at the appropriate location (Fig. 3.2).

The velocity profile in arteries leaving the heart has been reported to be closer to a time varying uniform profile (TVU) than a parabolic profile [33, 34]. For this reason, we apply TVU conditions at the inlet of Models C and E, Tables 3.1-2. Doppler measurements could not be made in this location, so a parametric study was performed. A base time averaged volumetric flow rate Q_5 was chosen proportional to the cross section area at Γ_5. Studies were then performed with Q_5 increased and decreased by 50% respectively to examine the sensitivity of the hemodynamic results to this value. The same standard time varying waveform was used as for the FOW conditions.

At other cross sections, the velocity has a more complex dependence on cross sectional position and is not well approximated as either FOW or TVU. At these locations, we applied the

so called "do nothing'' boundary condition using a modified stress tensor, which has the same divergence as the Cauchy stress tensor

$$T_{ij}^{'} = -p\delta_{ij} + \mu \frac{\partial v_i}{\partial x_j} \tag{13}$$

In (13), p is the mechanical pressure, v_i are the rectilinear components of the velocity vector $\underline{v}$, and T'_{ij} are the components of the modified stress tensor. We have employed standard indicial notation in (13). The modified stress vector is specified to be parallel to the local normal [49],

$$t_i^{'} = T_{ij}^{'} n_j = (\mu \frac{\partial v_i}{\partial x_j} n_j - p n_i) = C n_i \quad \text{on } \Gamma_\alpha \tag{14}$$

where n_i are the components of the outward normal to surface Γ_α and C is a prescribed constant. Here, α corresponds to 2, 4, 6 for Models A, B/D, C/E, respectively, Table 3.1. For our rigid wall model, this constant can be set to zero without any loss in generality of the results. From a physical perspective, the modified traction [81] condition given in (14) is preferable over specifying the Cauchy stress vector to be constant, which violates even the Womersley solution. For a comparison of condition (14) with other inflow/outflow conditions see [48]. A discussion of physical anomalies arising when the usual Cauchy stress vector rather than the modified stress vector is specified at outflow boundaries is given in [51].

The TVU condition was also applied at the trifurcation surfaces, Γ_7-Γ_9 (high AR) and quadrification surfaces Γ_7-Γ_{10} (low AR model). The trifurcation/ quadrification is a more complete outflow vasculature for Models A- C. Therefore, for consistency with these models, the sum of the flow rates through the trifurcation/ quadrification in Model D and E was specified to match that for outflow surfaces Γ_1 in Models A-C. For example, $Q_7 + Q_8 + Q_9 = Q_1$ for the

high AR model. The flow rate division among Γ_7-Γ_9 (high AR) and Γ_7-Γ_{10} (low AR) was specified such that the WSS was equal in these branches [82]. For these conditions, the WSS was approximated as $4\ \mu Q/\pi R^3$ where $R=\sqrt{A/\pi}$, and A is the cross sectional area. Thus the velocity magnitude $|\underline{v}|$ for the uniform profile can be calculated as $|\underline{v}| = Q/A$. The inflow and outflow conditions for all models at the relevant computational surfaces are given in Table 3.2.

From a mathematical perspective, the combinations of inflow and outflow conditions chosen for our models, Tables 3.1-2, are well posed. In particular, local existence and uniqueness can be shown for small data for steady and unsteady cases, [42, 50].

Hemodynamic Parameters

Using the parameters given above, the time averaged Reynolds number at the PPA region defined as:

$$\mathrm{Re} = \frac{\rho U D_{PPA}}{\mu} \tag{15}$$

ranged from 200 to 400. The Womersley number, defined as [83]

$$\alpha = R\sqrt{\frac{2\pi\rho f}{\mu}} \tag{16}$$

ranged from 3 to 5 based on the PPA radius, where R is the vessel radius and f is the fundamental frequency of the pulsatile waveform (Hz).

Here, the projection of the Cauchy stress vector on the arterial surface will be denoted as $\underline{\tau}_w$. The time averaged value of the magnitude of $\underline{\tau}_w$ over a period of one cardiac cycle will be denoted as WSS:

$$WSS = \left|\underline{\tau}_w\right| . \tag{17}$$

And the time averaged WSS is defined as:

$$TAWSS = \frac{1}{T}\int_0^T \left|\underline{\tau}_w\right| dt \tag{18}$$

While there is no clear demarcation of normal and abnormal WSS levels, values between 1.0 and 7.0 Pa are typically considered normal while those above 7.0 Pa and below 0.4 Pa are believed to be pathological [84].

To study the shear stress characteristics associated with pulsatile loading, the oscillatory shear index (OSI) was calculated using:

$$OSI = \frac{1}{2}\left(1 - \frac{\left|\int_0^T \underline{\tau}_w dt\right|}{\int_0^T \left|\underline{\tau}_w\right| dt}\right) \tag{19}$$

where T is the period of one cardiac cycle [85].

The contours of velocity magnitude are obtained for cross sectional slices perpendicular to the centerline and one diameter upstream from the aneurysm neck (same location for every model) in order to better understand the effect of domain truncation on flow into the aneurysm region.

For quantitative comparison between models, the WSS distribution was extracted along a representative curve in all models. This curve is the intersection of the lumen surface with the intersection plane shown in Fig. 3.4. The curve extends from the proximal neck (position s=0) to distal neck (position $s=s_3$) (Fig. 3.4). To further quantify the comparison between models, the

spatial average of the WSS error relative to Model E, ε, was calculated along these curves in aneurysm sac region as follows:

$$\varepsilon = \frac{\int_{S_1}^{S_2} |WSS - WSS_E| \, ds}{s_2 - s_1} \tag{20}$$

where ds is the infinitesimal arc length along the curve, WSS_E denotes the WSS at the corresponding point in Model E. The error is calculated in the sac, which extends from $s = s_1$ to $s = s_2$, where (s_1, s_2) = (2mm 12mm) for the high AR model and (2mm, 9mm) for the low AR model. Finally, this error was normalized by an representative parent artery WSS value of 1.2 Pa to obtain the percentage differences of error for each model.

(a)

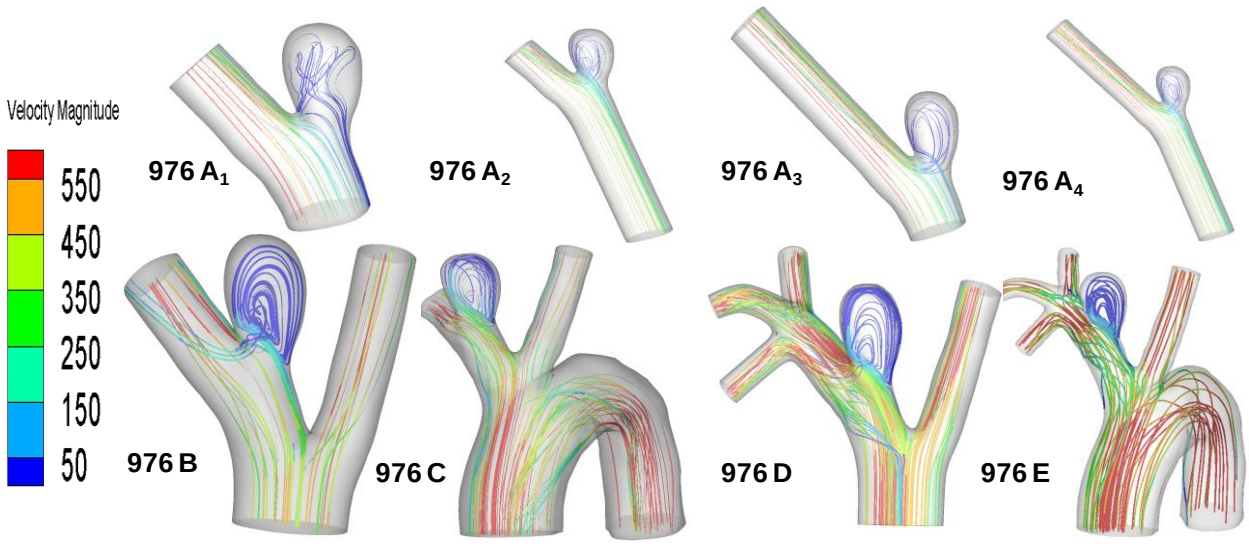

(b)

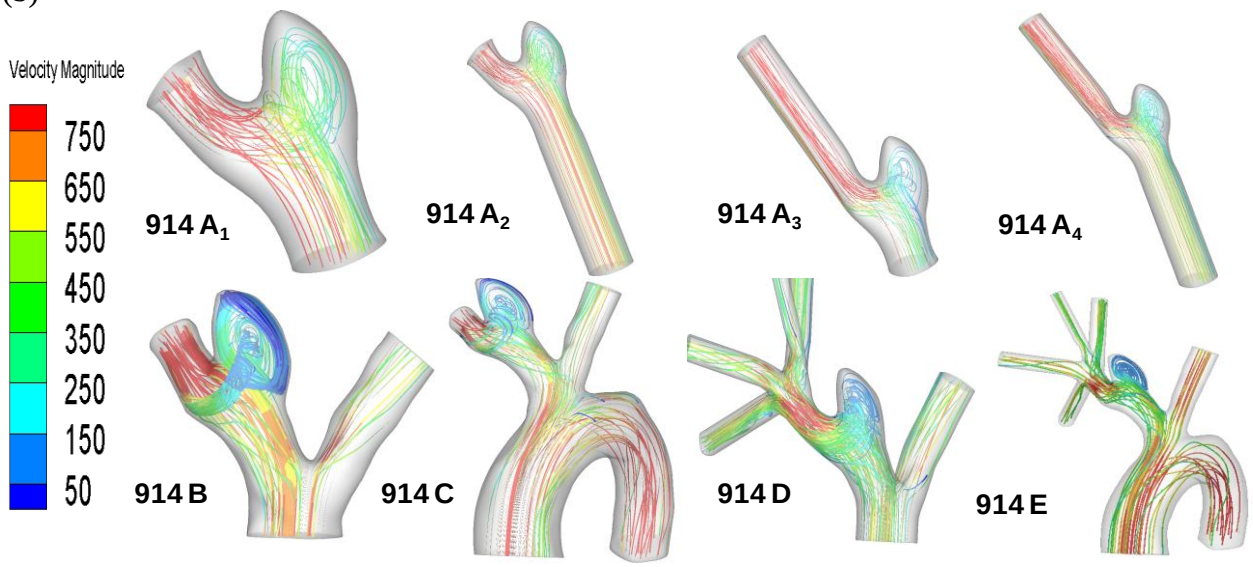

Figure 3.5 Streamlines for all models; (a) high AR case; (b) low AR case; color of the streamlines indicates the velocity magnitude (mm/s)

3.1.3 Results

The computational results for streamlines, WSS, OSI and contours of velocity magnitude for each model have been calculated and are shown in Figs. 3.5-10. In Table 3.3, the results for the streamlines, WSS and OSI are then categorized as similar (S) or not similar (NS) to Model E to provide a succinct summary of the comparison between models. The computational run times for the models are given in Table 3.4, and the errors along the intersecting curves are given in Table 3.5.

(a)

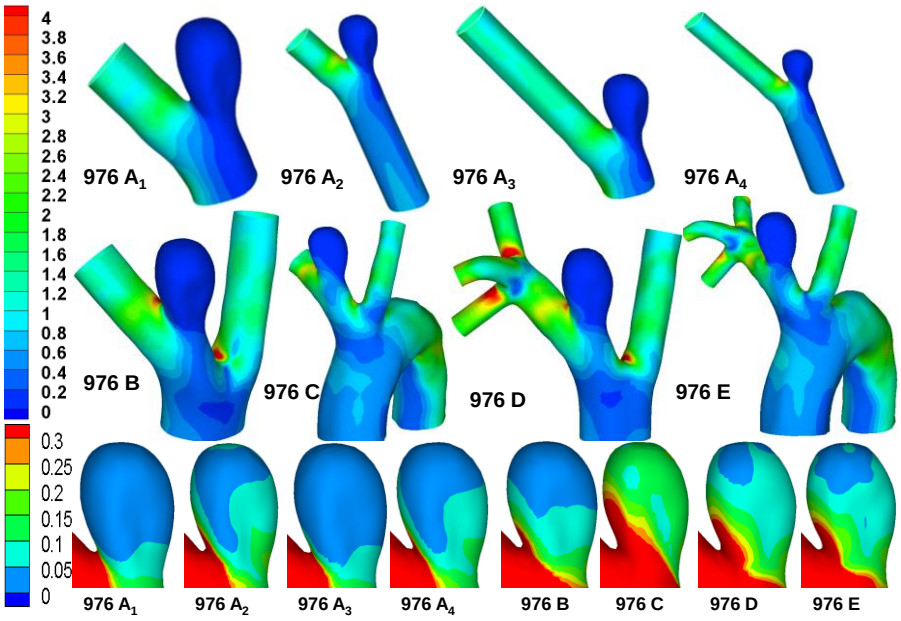

(b)

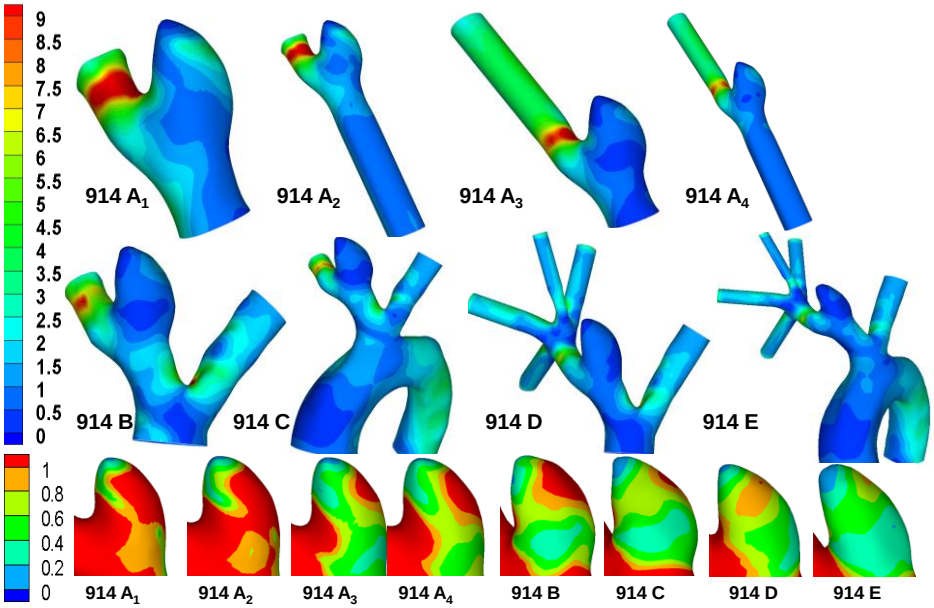

Figure 3.6 WSS contours for all models, (a) high AR case; (b) low AR case; unit in (Pa).

Model E (Reference Model)

Model E includes the most extensive vasculature and is used as a reference model to evaluate all other models.

Table 3.3 Summary of results for comparison of results for Models A-D with reference Model E, NS denotes not similar, S denotes similar.

	Hemodynamic Features in the sac	A_1	A_2	A_3	A_4	B	C	D
High AR case	WSS	NS	S	NS	S	S	NS	S
	OSI	NS	S	S	S	S	S	S
	Streamlines	NS	S	S	S	S	S	S
	Velocity contour	NS	NS	NS	NS	S	S	S
Low AR case	WSS	NS	NS	NS	NS	NS	NS	S
	OSI	NS	NS	NS	NS	S	S	S
	Streamlines	S	S	S	S	NS	NS	S
	Velocity contour	NS	NS	NS	NS	NS	NS	S

Table 3.4 Numbers of elements and computational time used for different model types

Model type	A_1	A_2	A_3	A_4	B	C	D
Element Quantity	15000	20000	20000	25000	26000	40000	70000
Computational time (Hours)	12	16	16	22	25	60	100

* Model E has 85000 elements, and took approximately 90 hours to complete after the computer was upgraded to 8GB memory. It could not be studied without this increase in memory.

Model D

By comparing the results for Model D with reference Model E, we can analyze the effects of truncating the aortic arch from the computational domain. For the high AR case (976), there is very good agreement in streamlines, WSS, OSI and velocity magnitude in the aneurysm sac

(Figs. 3.5 (a), 3.6 (a), 3.9 (a) and 3.10(a)). The WSS distribution in the sac region of the high AR Model D is quantitatively and qualitatively similar to Model E (Fig. 3.6(a) and Fig. 3.7). The error ε for Model D is 0.0031 Pa, and the error relative to a representative parent value of 1.2 Pa is less than 0.3%, Table 3.5.

Table 3.5 Spatially averaged magnitude of WSS error (relative to Model E) along curves formed by lumen surface and intersecting plane of the aneurysm sac region (Fig. 4) (units in Pa), and percentage difference of the error relative to parent artery WSS.

	A_1	A_2	A_3	A_4	B	C	D
High AR (976) case ε (Pa)	0.0412	0.0123	0.0501	0.0084	0.0236	0.0847	0.0031
WSS percentage difference relative to parent artery	3.4%	1.0%	4.2%	0.7%	2.0%	7.1%	0.3%
Low AR (914) case ε (Pa)	1.5352	1.3790	0.8021	0.5843	0.4153	0.2250	0.1354
WSS percentage difference relative to parent artery	130%	115%	67%	49%	35%	19%	11%

For the low AR case (914), the truncation of the aortic arch in Model D generates some minor differences with Model E. Little difference is seen in cross sectional velocity contours (Fig.3.10(b)); but the magnitude of velocity in the sac at the proximal wall is increased in D compared to E, (Fig. 3.5(b)). The WSS distributions are qualitatively similar in Models D and E of the low AR models with respect to the location of the maximum and minimum, though the WSS is slightly elevated in Model D at the proximal sac (Fig.3.6 (b) and Fig. 3.8). Specifically, the error ε is 0.1354 Pa (11%) in this case. While Model D correctly predicts the absence of

elevation in OSI throughout the low AR aneurysm sac, the region of elevated OSI at the proximal neck of Model E (Fig. 3.9(b)) is shifted.

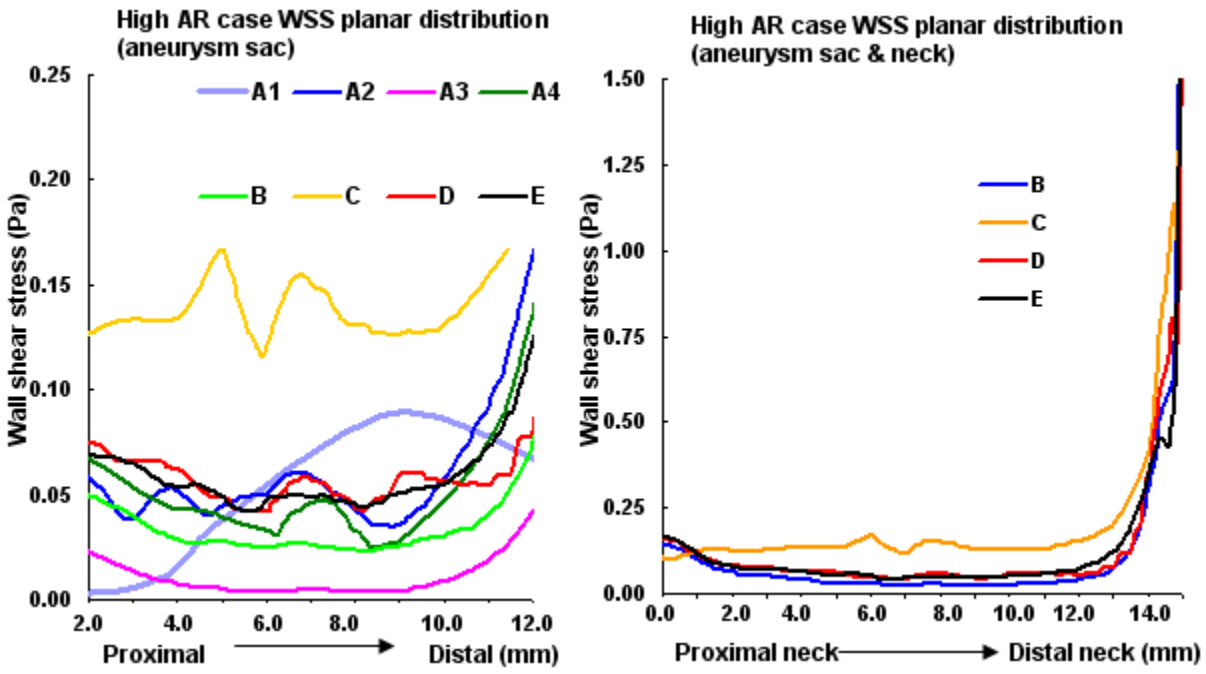

(a) (b)

Figure 3.7 WSS along intersecting curve for high AR case, (a) entire aneurysm region (sac and neck, Models B-E); (b) aneurysm sac only (Models A-E).

Model C

A comparison of results for Models C, D and E for both high and low AR cases shows the inclusion of the downstream trifurcation (quadrification) is more important than the inclusion of the aortic arch (Figs. 3.5-10). In particular, though the qualitative distribution is similar across

the three models, the WSS magnitude is markedly higher in Model C than in Models D and E (Figs. 3.6, 3.7 and 3.8). Further, ε increased to 0.0847 Pa (7.1%) in the high AR model and to 0.2250 Pa (19%) in the low AR model. The increased error in WSS for the low AR Model C is likely due to the error in velocity profile upstream of the sac (Fig. 3.10(b)). The general structure of the streamlines in the sac is similar across all three models, Fig. 3.5. There are only minor differences in the OSI patterns (Fig. 3.9(b)) between Models C and E. In particular, Model C predicts the region of elevated OSI at the neck of Model E. For the high AR case, the velocity contours upstream of the aneurysm are quite similar to those of Model E with respect to maximum and general distribution. The maximum is elevated in the low AR case, Fig. 3.10(b).

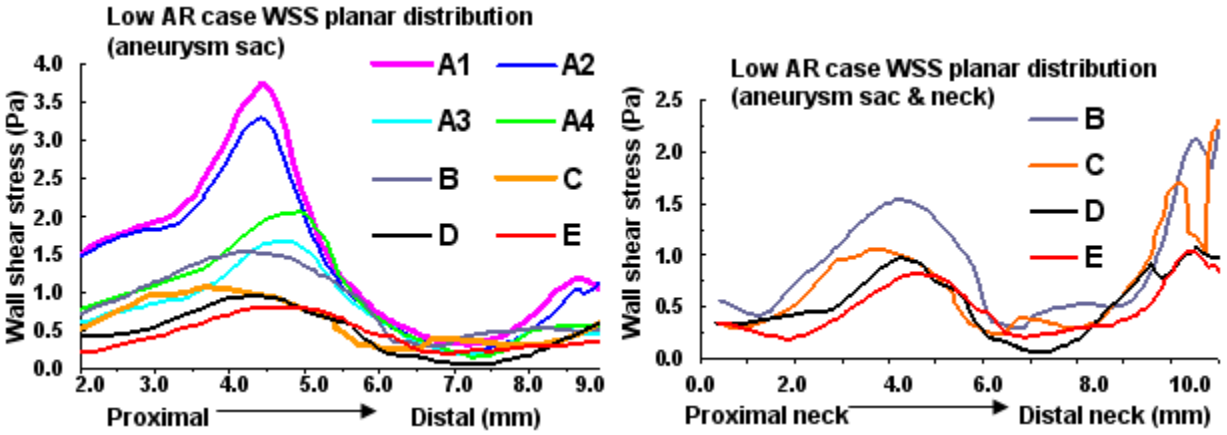

(a) (b)

Figure 3.8 WSS along intersecting curve for low AR case, (a) entire aneurysm region (sac and neck, Models B-E); (b) aneurysm sac only (Models A-E).

Model B

The error in employing a simple model in which both downstream trifurcation / quadrification and upstream aortic arch are removed can be evaluated by comparing Model B with E. The

general structure of the streamlines is similar for the high AR case, but differs slightly for the low AR case (Fig. 3.5). In the low AR case, the streamlines have a pronounced out of plane structure. For the high AR case, the WSS is in general slightly lower than in Model E, (Figs. 3.6(a) and 3.7) though the error is less than for Model C (Table 3.5). For example, the error is 2.0% for Model B and 7.1% for Model C. In contrast, for the low AR case, Model B has an elevated WSS value (Figs. 3.6(b) and 3.8) resulting in an error of approximately 35% for Model B compared to 19% for Model C and 11% for Model D. The velocity contours of Model B are quite similar to Model C for both cases, displaying the same error in magnitude relative to Model E for the low AR case.

(a)

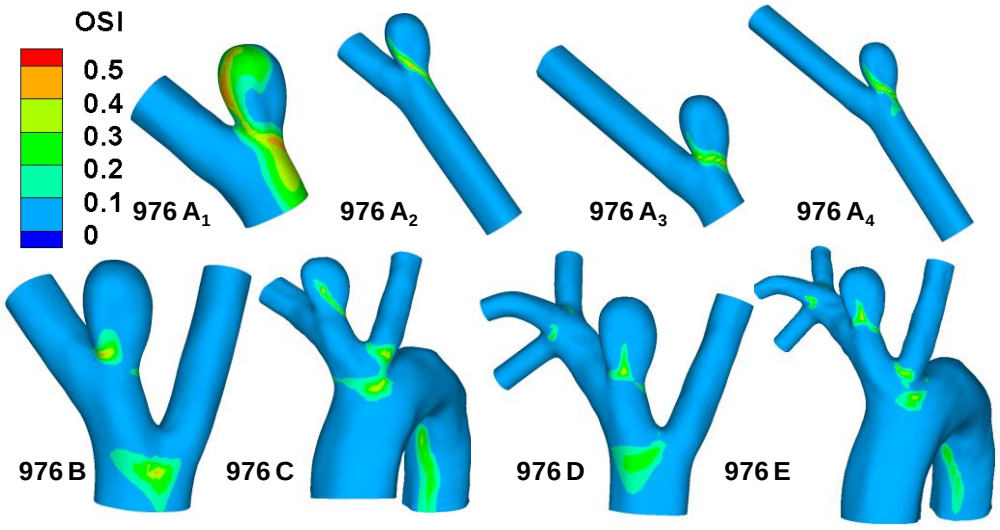

(b)

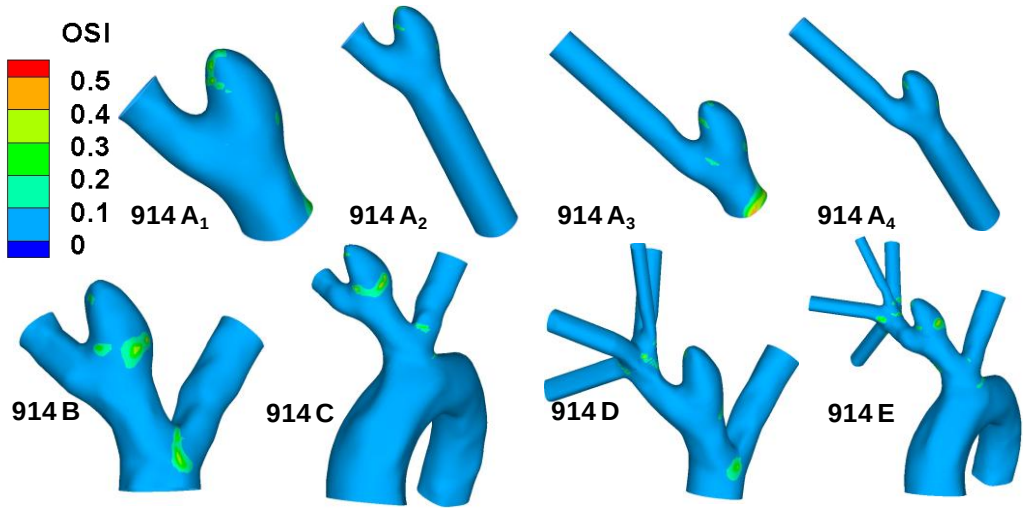

Figure 3.9 Contours of OSI; (a) high AR case; (b) low AR case.

Model A

The vasculature contained in Model A is vastly reduced compared with Model E, containing none of the upstream and downstream branching. Because of the simplicity of this model, upstream and downstream extensions were also included in an effort to diminish the impact of the imposed inlet and outlet conditions. Despite the simplicity of Model A, with the exception of the high AR Model A_1, the streamlines for Models A_1-A_4 are similar to those of Model E (Fig. 3.5). In these models, the fluid can be seen to enter the aneurysm at the distal neck and circulate in a single vortex before exiting the sac. In contrast, in high AR Model A_1, the flow enters the aneurysm sac through a larger region of the neck, after which the flow is diverted to both proximal and distal sides of the sac.

Of the four models, A_2 and A_4 best approximate the WSS for the high AR case. In fact, the error ε along the intersecting curve is less than for Models B and C, though greater (a) than D (Table 3.5). However, the region of elevated WSS at the distal neck in the sac of the high AR Model E (Fig. 3.6(a)) is not seen in Models A_1 and greatly reduced in Models A_2, A_3, and A_4. For the WSS prediction in the low AR case, Models A_1 and A_2 perform the worst while the errors in Models A_3 and A_4 are closer to that seen in Models B and C (Figs. 3.6(b), 3.8, and Table 3.5). The elevated OSI at the neck of high AR Model E is seen in Models A_2-A_4, though it differs in distribution, Figs. 3.9(a). For the low AR case, regions of elevated OSI are seen at the neck of Models A_1-A_4, but shifted and shrank comparing to the distribution in Model E. The high AR models with inlet extension (A_2 and A_4) have upstream velocity contours most similar to those of Model E with respect to distribution and maximum, Figs. 3.10(a). For the low AR case, the PPA cross section velocity magnitude is elevated in all Models A_1 - A_4. While A_4 provides the closest overall match of results to those of Model E, there is little improvement in run time for Model A_4 compared to Model B, Table 3.4.

(a)

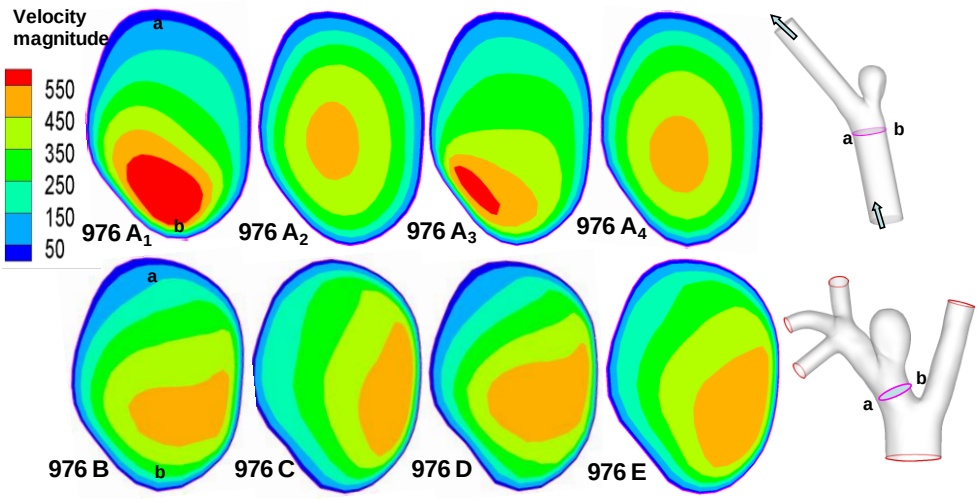

(b)

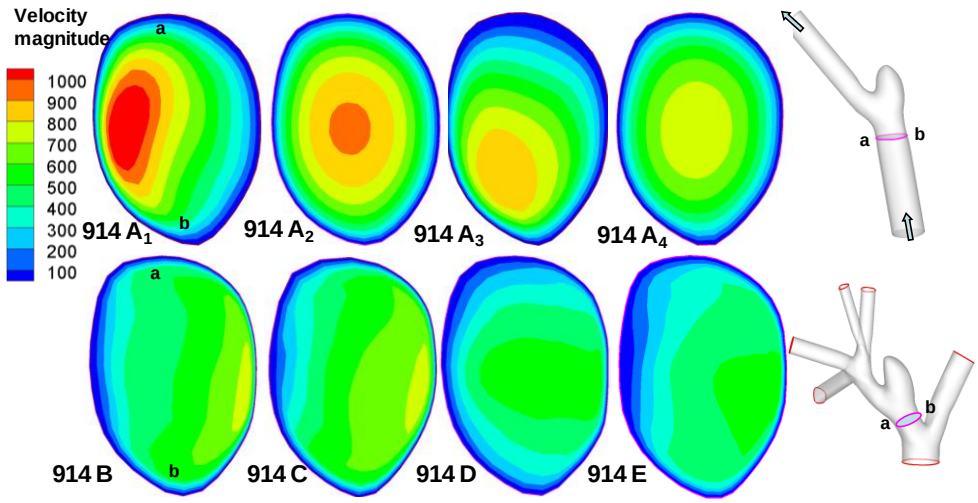

Figure 3.10 Contours of magnitude of velocity (mm/s) at systole in cross sectional slices of the PPA, (a) high AR case; (b) low AR case; a and b indicate the orientation of cross sections.

Further Evaluation of Model Conditions and Idealizations

As noted in the subsection Boundary conditions, the flow rate into the arch for Models C and E could not be measured, so was chosen to be proportional to the cross section area at Γ_5. This sensitivity of the solution to this condition was evaluated by reanalyzing the flow in Model C with the volumetric flow rate Q_5 increased and decreased from this value by 50%. The flow rates prescribed at outflow boundaries Γ_1 and Γ_3 were maintained at the same measured values for all three runs. The WSS distribution in the aneurysm was not visibly changed and the maximum

WSS magnitude changed less than 5%. Results with the baseline value of Q_5 of Model C are shown in Figs. 3.5-10.

Necessarily, there is a limit to the extent of the downstream domain which can be included in the computational model. The most extensive downstream vasculature was used in Models D and E which included the downstream trifurcation/quadrification. To further evaluate this choice, we analyzed results for Model D with extensions on the outlets of these downstream vessels. Since the flow in the sac of the low AR model was found to be more sensitive to other changes in vasculature, this model was considered. The spatial average WSS along the intersecting curve in the sac region changed less than 1% with the addition of these extensions.

3.1.4 Discussion

The current study evaluated the influence of the extent of the computational domain on calculated hemodynamic features within saccular aneurysms in an animal model. If only a bulk measurement of WSS magnitude in the aneurysm sac is of interest, it is sufficient to consider even the simplest model with inlet and outlet extensions (Model A_4). For example, the high AR Model A_4 correctly predicts the WSS to be pathologically low through almost the entire aneurysm sac and correctly predicts the minimum at the dome and maximum at the distal neck. Model A_4 is less effective for the low AR case, it correctly predicts the locations of the maximum and minimum WSS in the aneurysm sac, however the magnitude is elevated in general. With the advent of more localized measurements of biological function it is often desirable to have reliable *local* estimates of these hemodynamics (e.g. [46]). In these cases,

more exacting criteria must be used for model selection and more extensive vasculature is required.

Our results have shown the level of sensitivity of *local* values of WSS and OSI to the extent of model geometry depends strongly on the aspect ratio. For the high AR model, WSS and OSI results are fairly similar among Models A_2, A_4, B, D, and E with Model D giving the most accurate reproduction of results for WSS. Namely, our results suggest that removing the aortic arch is suitable for high AR studies, yielding errors in WSS of 2% or less along the intersecting curve for all these models. Using simple models for the high AR studies result in substantial savings in computational time. For example, Model A_4 requires 78% less computational time than Model D, Table 3.4.

The low AR hemodynamic results were much more sensitive to the inclusion of surrounding vasculature. If a reliable estimate of local values of WSS is needed, Model D is the clear choice yielding an error along the intersecting curve of less than 11% for the aneurysm sac region. Model D correctly captures the location of the maximum and minimum in WSS. Unlike the high AR model, the low AR Model A_4 does not provide a reasonable quantitative prediction of the WSS distribution. There is little motivation for using Model C rather than Model D with respect to WSS results. Though the runtime dropped by 40%, the error in spatially averaged WSS in the sac increased from 11% to 19% in the low AR case and from 0.3% to 7.1% in the high AR case. Namely, inclusion of the downstream vasculature was more important than inclusion of the aortic arch for WSS results in both the low and high AR models. This is likely due to the close proximity of the downstream branches to the aneurysm sac.

If OSI is of interest, then it is particularly important to clarify the conditions necessary for a model to be suitable. For example, in the high AR case, all models except A_1 correctly predict the low OSI throughout the dome and elevated OSI at the neck. However, only Model D reproduces the general spatial distribution seen in Model E. In the low AR case, Models A_1-A_4 are all poor, predicting elevated OSI in different regions than the reference model. Although Models B, C and D correctly predict elevated OSI in the neck region, the extent of tissue with elevated OSI is diminished in Model D relative to Model E.

The influence of idealizations for the native upstream vasculature on intraaneurysmal hemodynamics was previously considered by Castro et al. for flow in patient specific models of cerebral aneurysms [86]. They evaluated the effect of replacing the native vasculature directly upstream of the aneurysm with a straight cylinder, such as was considered in Model A_2 of this work. Their results showed that gross simplifications in the upstream geometry led to changes in the WSS field. They did not consider the impact of downstream vasculature.

This study suffered some limitations. The range of geometric variations considered was necessarily finite. Further, the inflow and outflow velocity data was obtained from Doppler wave form imaging, which is planar and not volumetric. Recently we have aquired pointwise velocity measurements using phase contrast magnetic resonance angiographs (PCMRA) in the parent vessels (unpublished data). We intend to use these data for future studies. In comparing hemodynamic results across models, we considered commonly used parameters (WSS and OSI) as well as streamlines and velocity fields. Identification of the most important parameters for a

given vascular pathology remains an area of active research. The quantitative comparison of the pointwise results between models was confined to an assessment of the WSS along curves formed by the intersection of a selected plane and the aneurysm lumen. A representative plane was chosen that intersected the proximal, distal and apex sac regions. Table 4 provides an assessment of the ability of Models A-D to reasonably reproduce the hemodynamic results of reference Model E. However, it should be kept it mind that the suitability of a particular model depends on the hemodynamic parameter of interest and magnitude of acceptable error.

We included a number of idealizations to render the computational studies tractable. The vessel walls were modeled as rigid. The motion of the arterial wall is generally accepted as causing only secondary hemodynamic effects compared with geometric and unsteady flow effects [10, 87]. Another idealization was to treat the blood as Newtonian using the high shear rate viscosity for blood. The viscoelastic and shear thinning properties of blood are largely due to the aggregation and formation of 3D microstructure of red blood cells. However, these structures are not expected to be stable at the shear rates found in the arteries and aneurysm sacs studied here [57].

Finally, while the focus of this work was a rabbit model for cerebral aneurysms, the approach taken here can be used for hemodynamic studies of other species and pathologies. The circle of Willis, where most cerebral aneurysms are found, has a complex geometry with numerous branches and curved regions. We anticipate that inclusion of neighboring vessels will also be important for studies of local hemodynamics in saccular aneurysms in this region. Further, we expect our findings regarding influence of the extent of the vascular domain to

apply to experimental studies of hemodynamics in physical models of elastase induced rabbit aneurysms.

3.1.5 Conclusion

The results of this work suggest the extent of model geometry which should be used in hemodynamic studies of elastase induced aneurysms in rabbits depends strongly on the aneurysm aspect ratio, hemodynamic parameters of interest and magnitude of acceptable error. Results for the high AR model are much less sensitive to the surrounding vasculature, suggesting even the simplest model with extensions is capable of reproducing WSS and OSI distributions. However, flow in low AR aneurysms is more sensitive to the extent of the model. If WSS is of primary concern for these aneurysms, the inclusion of downstream vessels is more important than the aortic arch. Careful attention to these outcomes can substantially decrease the computational requirements and increase reliability of the results for future CFD studies.

3.2 HEMODYNAMICS AND ANATOMY OF ELASTASE-INDUCED RABBIT ANEURYSM MODELS--SIMILARITY WITH HUMAN CEREBRAL ANEURYSMS?

3.2.1 Background and Purpose

The central goal of the current work is to evaluate the homology of both the geometric and estimated hemodynamic features in the elastase induced rabbit aneurysms as compared to previously reported values for human IA. This comparison is necessary to justify the use of the animal model as a testbed for hemodynamic based human IA research. Further, the results of this study will enhance our ability to interpret fundamental biological studies in this model aneurysms system.

To achieve this objective, the anatomy and hemodynamics for elastase-induced rabbit aneurysms (n=51) were evaluated using CFD and compared with published results for human aneurysms. The relevance of this model was evaluated in two contexts. The first was to determine whether the range of geometric and hemodynamic parameters of the rabbit model is realistic for humans. That is, do they lie within the range reported for human IAs? The second focus was to determine whether the range of geometric parameters produced in the rabbit model provide a large enough spectrum to test current hypothesis about the role of geometry in aneurysm development and rupture.

3.2.2 Materials and Methods

Aneurysms were created in Mayo clinic as reported in section 3.1. For the current study, a range of aneurysm sizes was purposefully created using previously reported techniques [88-91].

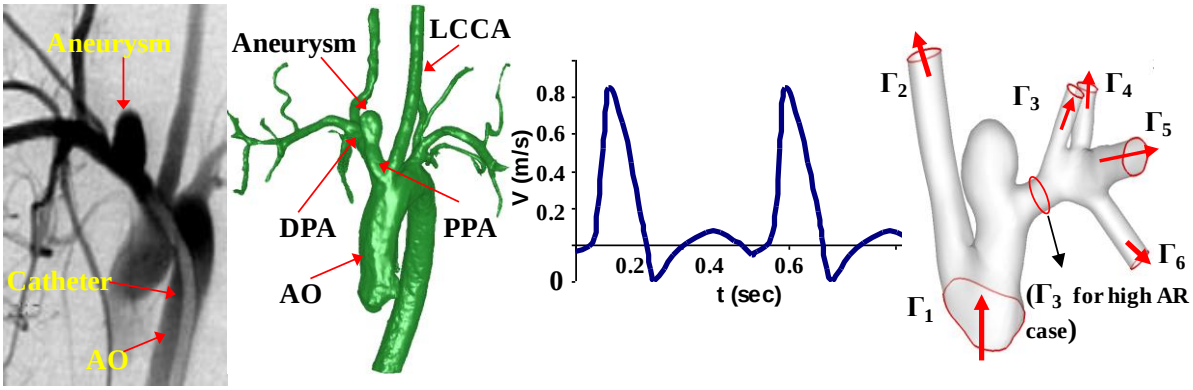

Figure 3.11 From left to right: (A) Digital subtraction angiogram of an elastase-induced aneurysm, proximal parent artery (PPA), distal parent artery (DPA), left common carotid artery (LCCA), aortic arch (AO), and catheter; (B) Reconstructed 3D geometry from 3DRA images; (C) Ultrasound waveform (inset) and idealized velocity waveform in CFD; (D) Computational domain for CFD analysis with flow directions (red arrows), inlet surfaces (Γ_1) and outflow surfaces (Γ_2, Γ_3 for high AR models) and (Γ_2- Γ_6 for low AR models).

The image procedures and in vivo flow information measurements were taken in the Mayo clinic as described in Section 3.1. The resulting 3D reconstruction of the vasculature and waveform are shown in Fig.3.11.

Geometric measurements were obtained from the 3D reconstructed models using Mimics (Materialise Inc., Leuven, Belgium), Geomagic studio (Geomagic. Inc., North Carolina, USA) and Solidworks (Dassault Systèmes SolidWorks Corp, Massachusetts USA). Briefly, the

centerline of the parent vessel and aneurysm were determined, after which the neck cross section and cross section of maximum area were extracted perpendicular to the centerline.

The hydraulic neck diameter (N) and maximum aneurysm diameter (D) were measured for these cross sections. The height of the aneurysm (H) was specified as the distance from the geometric center of the neck cross section to the aneurysm apex. The aneurysm surface area (S) and aneurysm volume (V) were obtained from numerical integration of the surface and volume of the reconstructed aneurysm sac. The hydraulic diameters of the proximal (D_{PPA}) and distal (D_{DPA}) segment of the parent arteries were measured one neck diameter upstream and downstream of the closest edge of the aneurysm neck. Four non-dimensional geometric parameters were considered: the aspect ratio (AR) [75, 76], D/H [12], bottleneck factor (BF) [92], and non-sphericity index [93]

$$AR=H/N, \qquad BF=D/N, \qquad NSI=1-(18\pi)^{1/3}(\mathbf{V})^{2/3}/S$$

A cutoff AR of 1.8 was used to distinguish between low and high AR aneurysms. This cutoff is intermediate between the value of 1.6 proposed by Ujiie et al (2001) and Weir et al. (2003) and that of 1.85 proposed by Raghavan (2005) as being valuable for predicting IA rupture [43, 75, 93].

Computational Fluid Dynamic (CFD) Analysis

The CFD set up and material selection is as the same as in section 3.1. The extent of the vascular domain necessary to obtain reliable CFD results in the elastase induced rabbit model was evaluated in an earlier work [94]. Based on the studies in section 3.1, the LCCA, proximal parent artery (PPA), DPA and aneurysm itself were included in the computational domain of

the high AR cases. The low AR domains consisted of the high AR domain plus the downstream trifurcation /quadrification structure (Fig.3.11D).

The inflow and outflow conditions follow those specified in section 3.1 [94]. Briefly, a time varying uniform velocity profile was specified at all outlets of the models (cross sections Γ_2- Γ_6 for low AR models, Γ_2 and Γ_3 for high AR models). The magnitude was chosen to match the animal specific waveform measured *in vivo,* as noted above. A modified traction condition or so called "do nothing" boundary condition was applied at the inlet (Γ_1) of all the models [49].

The finite element mesh of the computational domain was composed of 40,000 to 60,000 hexahedral (brick) elements. This mesh density was found to give less than 3% change in maximum WSS compared with results from a model with double the mesh density along the centerline. CFD analyses were performed for each model for a duration of two cardiac cycles using 100 time steps per cycle. Simulations were performed using a 3-GHz dual Xeon processor work station with 8-GB of memory. The simulation time ranged from 16 to 20 hours depending on model size.

Hemodynamic Parameters

Several measures of the hemodynamic wall shear stress vector $\underline{\tau}_w$ -- the magnitude of the wall shear stress vector (WSS), the time averaged wall shear stress (TAWSS) and the oscillatory shear index (OSI) (32) were evaluated. Two dimensionless flow parameters time averaged Reynolds number (Re) and the Womersley number α were also considered, as defined in (15) and (16).

Human intracranial aneurysm data: Literature review

A systematic search of previously published human IA geometric and hemodynamic parameters was conducted using keywords: cerebral, aneurysm, geometry and hemodynamics in the PubMed online database. In general, only studies with at least 20 cases and a quantitative analysis of aneurysm geometry and/or hemodynamics were included in the analysis, (Table 3.6). Only two studies were available for quantitative OSI values and distribution in human IAs [11, 95]. Therefore, despite the small sample sizes of two and six they were included in the analysis.

Table 3.6 Previously reported geometric and hemodynamic features from human aneurysms.

	Human aneurysm study compared	**No. of aneurysms**	**Parameters reported corresponding to rabbit aneurysms**
Geometry	Parlea et al. (1999)	87 cases	D, H, N, D/H, AR, BF
	Raghavan et al. (2005)	27 cases: 9 ruptured; 18 unruptured	D, H, N, V, S, AR, BF, NSI
	Jou et al. (2008)	26 cases: 8 ruptured; 18 unruptured	D_{PA}, N, AR, S
Hemodynamics	Cebral et al. (2005)	62 cases	TAWSS, flow structure, impingement region, pressure, OSI
	Hassan et al. (2005)	68 cases	WSS; flow structure
	Jou et al. (2008)	26 cases	WSS (end diastole)
	Karmonik et al. (2010)	6 cases	OSI
	Stienman et al. (2003)	2 cases	TAWSS, velocity field, flow structure, OSI
	Shojima et al. (2004)	20 cases	WSS (peak systole)
	Shojima et al. (2005)	29 cases	Pressure

3.2.3 Results

Aneurysm Geometry

Table 3.2 and Fig. 3.12 display geometric results for 51 elastase induced aneurysm models and human IAs from the literature. Human geometric data for the study were taken from the retrospective works of Parlea et al. [12] and Raghavan et al. [93] on IA, Parlea et al. analyzed the geometry of 87 simple-lobed aneurysms using 2D angiographic data. Raghavan et al. evaluated geometric features from 3D reconstructions from 27 aneurysms. The dimensional geometric parameters of the 51 cases for the rabbit model all fall within the range reported for human IA, including aneurysm height, width, neck, volume and surface area, (Table 3.2, Fig. 3.12A).

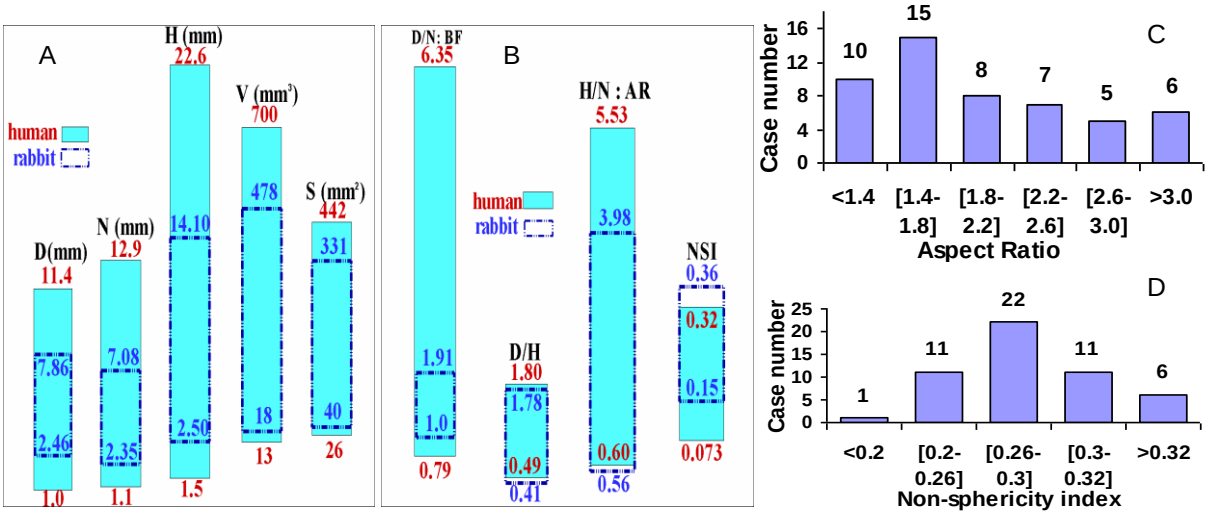

Figure 3.12 (A) Range in geometric features for human and rabbit model aneurysms: maximum diameter (D, mm), neck diameter (N, mm), height (H, mm), volume (V, mm^3) and surface area (S, mm^2); (B): Range in geometric indices: aspect ratio (H/N), bottle neck factor (D/N), D/H and non-sphericity index; (C) Distribution of AR for rabbit aneurysms; (D) Distribution of NSI for rabbit aneurysms.

The ARs in the 51 prospectively created rabbit aneurysms range from 0.56 to 3.98 with a good distribution of ARs across the cases, Fig. 3.12C. The rabbit AR values fall nearly completely within the range reported for human IAs and are almost evenly split between low and high aneurysms (25 low and 26 high).

Table 3.7 Comparison of geometric features in rabbit aneurysms (n=51) and human aneurysms (from published results).

Geometric features	**Rabbit aneurysms**		**Human aneurysms**	
	Mean	Range	Mean	Range
D (mm)	5.27 ± 1.02	[2.46—7.86]	Ruptured 4.87 ± 1.86; Unruptured 4.81 ± 1.37(10)	[1—11.4] (9).
N (mm)	4.12 ±1.01	[2.35— 7.08]	Ruptured 3.79 ± 1.58; Unruptured 4.25 ± 1.38 (10) Ruptured 4.1 ± 1.1; Unruptured 4.1 ± 1.2 (4)	[1.1—12.9] (9).
H (mm)	7.98 ± 2.79	[2.50— 14.10]	Ruptured 6.55 ± 3.80; Unruptured 5.13 ± 1.54 (10).	[1.5—22.6] (9).
DPPA (mm)	4.01 ± 0.55	[3.10—5.25]	Internal Carotid: 3.56mm, Basilar: 3.23mm (9)	——
DDPA (mm)	3.26 ± 0.51	[2.5—4.23]	Internal Carotid: 4.7mm (4)	
V (mm^3)	146 ± 98	[18—478]	Ruptured 146 ± 219; Unruptured 84 ± 59 (10).	[13—700] (10)
S (mm^2)	142 ± 66	[40—331]	Ruptured 122 ± 128; Unruptured 83 ± 41 (10). Ruptured 256 ± 351; Unruptured 124 ± 110 (4).	[26—442] (10)
BF (D/N)	1.31 ± 0.24	[1.00 —1.91]	Ruptured 1.387 ± 0.492; Unruptured 1.156 ± 0.171 (10). 1.91 ± 0.86 (9).	[0.79—6.35] (9).
D/H	0.72 ± 0.25	[0.41—1.78]	1.11 ± 0.29 (9).	[0.49—1.80] (9).
AR(H/N)	2.01 ± 0.76	[0.56—3.98]	Ruptured 1.85 ± 0.79; Unruptured 1.27 ± 0.40 (10) 1.86 ± 0.86 (9). Ruptured 2.0 ± 0. 9; Unruptured 1.5 ± 0.8 (4).	[0.60—5.53] (9).
NSI	0.28 ± 0.03	[0.15—0.36]	Ruptured 0.233 ± 0.061; Unruptured 0.156 ± 0.058 (10).	[0.073—0.32] (10)

The NSI value in the rabbit models range from 0.15 to 0.36, extending above the 0.32 maximum reported in humans, Fig. 3.12B. Mean NSI values of 0.156 and 0.233 were reported for unruptured and ruptured human IAs, respectively (Table 3.7). The range of NSI in the rabbit model includes both these values, though it is skewed toward the higher NSI range, Fig. 3.12B. The range of rabbit D/H values shows excellent agreement with human data, nearly coinciding with the human IA range, (Table 3.7, Fig. 3.12B). The rabbit BF values also fall within the human range, though they are at the low end of these values.

Intrasacular Hemodynamics

Hemodynamic results for all 51 rabbit models are shown in Table 3.3 and Figs. 3.13. Corresponding results for human IA are summarized in Table 3.3.

Non-dimensional Flow Parameters

Re for the rabbit model ranged from 200 to 400, comparing well with values of 200 to 500 in and around the Circle of Willis of humans [81, 96]. The rabbit Womersley number using a reprentative f of 3.3 Hz was 2.5-5.0 as compared to reported values of 1.5-5 [97] for humans.

Qualitative features of flow

The systolic streamlines for two representative rabbit sacs are shown in Fig. 3.13A. For all rabbit models, the fluid entered the sac from the distal side and exited from the proximal side. The flow structures could be categorized as Type A flows with a single and stationary circulation inside the aneurysm sac and Type B flows with a transient secondary circulation in the dome as well as a primary (larger) stationary circulation below this. This transient secondary circulation

was apparent at diastole and disappeared by systole. For Type A flows, the inflow velocity is faster and occupies a smaller percentage of the neck.

A

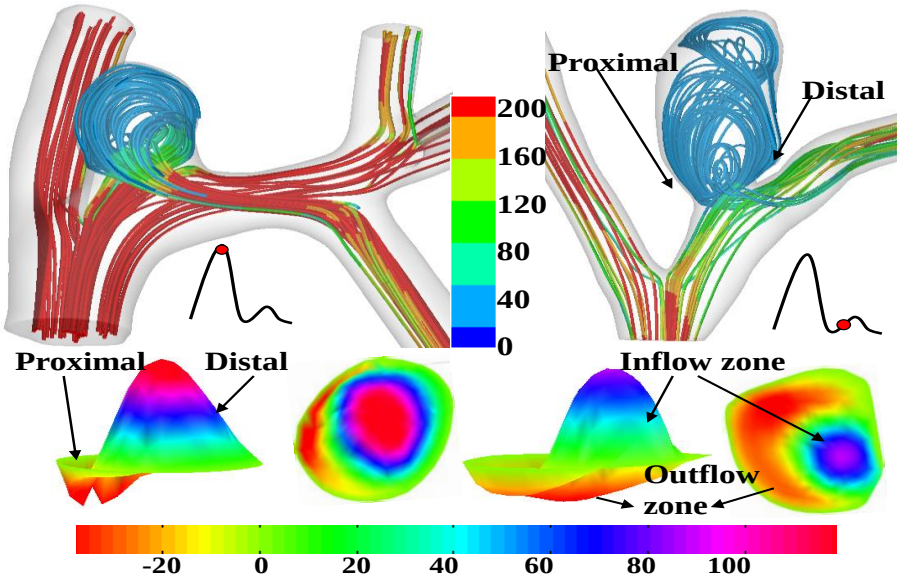

B

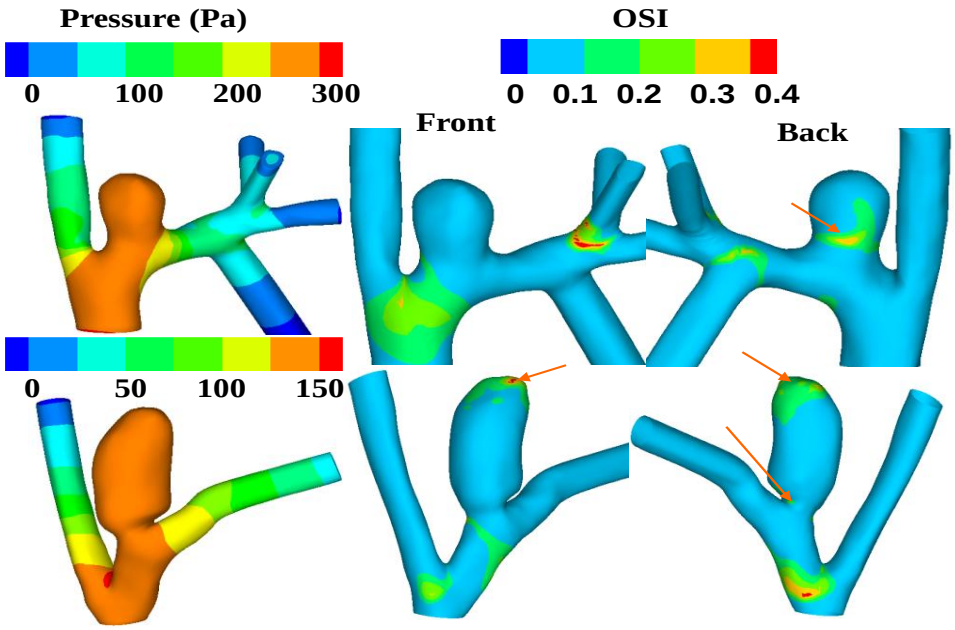

C

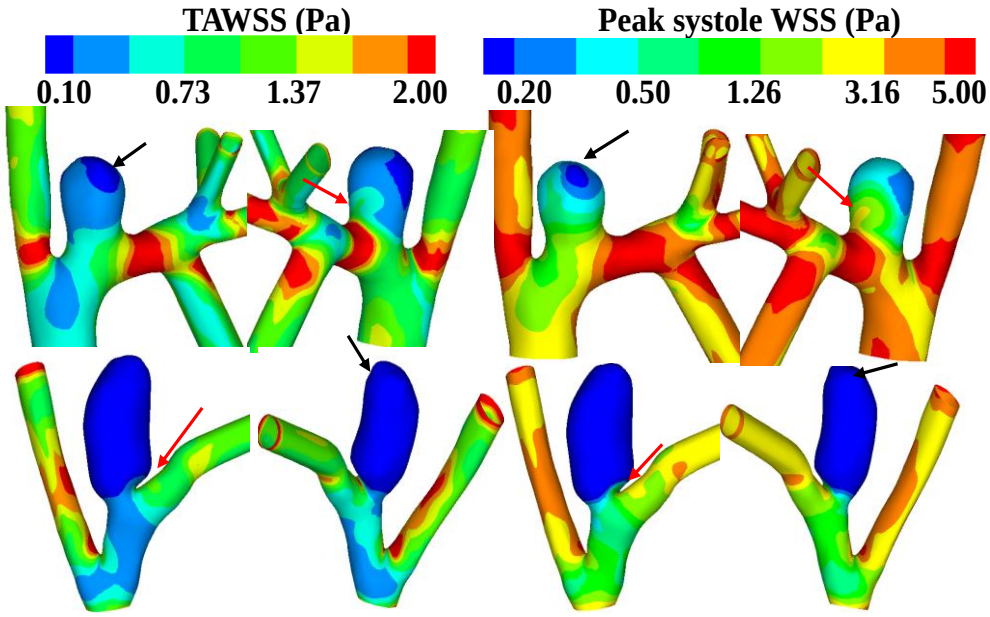

Figure 3.13 Hemodynamic results for two representative cases.

(A) Top row: streamlines at peak systole displaying two types of flow structures. Color designates velocity magnitude (mm/sec). Bottom row: Corresponding normal component of velocity (mm/s) at aneurysm neck are shown below. Heights not drawn to scale. Color reflects magnitude. (B) Left column: Pressure (left column, Pa) at peak systole relative to zero reference pressure at inlet surface Γ1 (1 mmHg = 133.3 Pa). Center and right columns: Two views of OSI distribution. Arrows indicate regions of elevated OSI. (C) TAWSS (Pa) and WSS (Pa) at peak systole (1 Pa = 10 dynes/cm2). WSS contours in logarithmic scale. Red/black arrow indicates the maximum/minimum value in aneurysm sac.

133.3 Pa). Center and right columns: Two views of OSI distribution. Arrows indicate regions of elevated OSI. (C) TAWSS (Pa) and WSS (Pa) at peak systole (1 Pa = 10 dynes/cm^2). WSS contours in logarithmic scale. Red/black arrow indicates the maximum/minimum value in aneurysm sac.

In their study of hemodynamics in 62 human IAs, Cebral et al. identified four categories of flow based on the nature of the inflow jet and the number and transient nature of circulation regions in the sac [7]. Type I displays an inflow jet with an unchanging direction and a single circulation region (44%) as seen in the Type A rabbit model described above. Type III displays a shifting inflow jet with one stationary and one transient circulation region (17%), similar to the Type B rabbit model. The other categories observed by Cebral et al. display multiple stationary circulation patterns (19%) and one stable and multiple transient recirculation regions (20%). Hence, the flow types in the elastase-induced aneurysms correspond to 61% of those analyzed by Cebral et al [7].

The impingement region of the rabbit models is always located at the distal neck and a slow jet flow is observed at the distal wall. This impingement location was reported in 20% of all human IA in Cebral et al. [7], though impingement was also found at the aneurysm dome and side walls.

Wall Pressure

The spatial variations in pressure within and around the aneurysm sac is small, (Fig. 3.13B). The range in pressure was less than 0.05 mmHg within the sac and less than 0.5 mmHg between the sac and its parent artery, (Table 3.8). Similarly, the pressure in human IA is relatively constant and deviates less than 1 mmHg from the pressure in the parent vessel [7, 98] (Table 3.6).

Oscillatory Shear Index

OSI ranged from 0.3 to 0.4 in subregions of the neck of the 51 rabbit aneurysms (Table 3.8, Fig. 3.13C). A second region of elevated OSI was found at the top of the aneurysm for all Type B flows (n=18) and not seen in any Type A flows. This is to be expected from the transient secondary circulation in those flows. The OSI was also elevated along the side walls of the sac for a smaller group of cases (n=15). Literature on human aneurysms similarly reported elevated OSI in the neck, sidewall and dome [11, 95]. The maximum values of OSI range from 0.3 to 0.4 for both human and rabbit aneurysms.

Wall Shear Stress

The average TAWSS across the PPA of the rabbit models was 0.81 Pa and ranged from 0.23 to 1.48 Pa. TAWSS was markedly lower inside the majority of the sac and elevated on the distal neck compared with the parent artery (n=51), (Fig. 3.13D, E). On the distal neck, the TAWSS was higher than 0.5 Pa while in the aneurysm domes the TAWSS was less than 0.1 Pa and nearly uniform (n=47) (Fig. 3.13, Table 3.8). While there were large quantitative differences between WSS at peak systole and TAWSS, the qualitative structure was very similar (Fig. 3.13D, E).

In human aneurysms, the distal neck has been identified as the region of highest WSS [8, 9, 95, 99]. Shojima et al. noted that 18 out of 20 middle cerebral artery aneurysms displayed a highly localized region of elevated WSS, either just inside (n=10) or just outside (n=8) the neck [8]. In all 51 rabbit aneurysms the highest WSS was found at the neck. The WSS inside the rabbit aneurysms was markedly lower (below 1 Pa) than the WSS in the parent arteries,

particularly in the aneurysm dome where it was always less than 0.1 Pa. In contrast, Cebral et al. reported a second region of highly elevated WSS (on the order of 5 Pa) within the upper sac [7].

Table 3.8 Hemodynamic features from rabbit aneurysms (n=51) and human aneurysms.

Hemodynamic features	**Rabbit aneurysms**	**Human aneurysms**
Reynolds Number (Re)	Range [200—400]	Range [200—500] (33, 34)
Womersley Number (α)	Range [2.5—5.0]	Range [1.5—5.0] (35)
Flow pattern	Type A: Single stationary recirculation; Type B: Single stationary recirculation in lower sac and secondary transient recirculation in the dome.	Four flow categories including Types A and B (2)
Pressure difference between parent artery and sac (mmHg)	0.36 ± 0.19 Range [0.1—0.5]	0.89 ± 0.68 (6); ~ 0.5 (2).
Oscillatory Shear Index	Elevated [0.3—0.4] at Neck (n=51) Side walls of sac (n = 15) Dome (n = 18)	Elevated OSI [0.24—0.47] at neck, sidewall and dome (7, 8).
Spatially averaged WSS at peak systole (aneurysm sac, Pa)	0.49 ± 0.62 Range [0.02—3.2]	1.64 ± 1.16 (5); Range [0.1—3.4] (5).
Spatially averaged TAWSS (aneurysm sac, Pa)	0.13 ± 0.20 Range [0.002—1.23]	——
Spatially averaged WSS at peak systole (PPA, Pa)	2.16 ± 0.93 Range [1.02—4.89]	3.64 ± 1.25 (5)
Spatially averaged TAWSS (PPA, Pa)	0.81 ± 0.33 Range [0.23—1.48]	——
Location of maximum WSS	Distal neck (n = 51)	Neck (3, 5) Often at distal neck (4)
Location of minimum WSS	Dome (< 0.1 Pa)	Dome (3-5)

3.2.4 Discussion

The primary focus of this work was to determine whether the geometric and hemodynamic environments created in an elastase induced aneurysm model in rabbits are similar to those reported for human IAs. This aneurysm model is receiving increased attention as a system for testing novel therapies and studying fundamental issues in the aneurysm pathophysiology. It is therefore of great importance to demonstrate the relevance of this model to human aneurysms. The results of the current work also provide a data base of geometric and flow properties in a large set (n =51) of elastase induced aneurysms. Data of this kind will be useful in applications such as the design of representative in vitro systems to compliment in vivo studies in the rabbit model. The dimensional geometric parameters of the 51 elastase induced aneurysms all fall in the human range. With the exception of NSI, the non-dimensional geometric parameters are also within the human IA range. The aspect ratio has been proposed as an important parameter for predicting likelihood of IA rupture [43, 76]. Recently, methodologies have been developed for constructing a large range of neck and heights in the rabbit model [90, 91]. Using these techniques, a good distribution of human AR was created, evenly divided between low and high AR. The AR values for the rabbit model lie almost completely within the human range, Fig. 2B. These results suggest the geometry of the rabbit model is suitable for exploring the potential coupling between AR and aneurysm pathophysiology

The recently introduced NSI was found to be the best geometric predictor of rupture in a study of 27 IA and 13 geometric parameters [93]. The range of NSI in the rabbit model includes the mean value reported for both ruptured and unruptured human IA, though it is skewed toward the higher NSI range, Fig. 3.12B. If the clinical usefulness of this shape index is supported by a larger prospective study, it may be worthwhile to increase the pool of low NSI cases in future rabbit studies. It is worth noting that this shape ratio does not distinguish between increases in surface area from different causes such as ellipticity and surface undulation, nor does it distinguish between different orientations of the long axis of the aneurysm relative to the parent vessel.

No data are available for the correlation of D/H and IA rupture. However, both the BF and the geometric ratio D/H have been proposed as useful parameters for predicting the success of endovascular coil placement and surgical clip applications [92]. The range of rabbit D/H values nearly coincides with human values. While the range of BF in the rabbit model is in the low range for human IA, it includes the mean for both ruptured and unruptured IA [93], (Table 3.7, Fig. 3.12B).

Cebral et al. (2005) categorized the human intra-aneurysmal flow into four types depending on the complexity and transient nature of the flow [7]. Types I and III were identified in 50% and 79% of human bifurcation and terminal aneurysms, respectively. These same two flow types are the most common in the rabbit model, despite the fact that it is more similar to a sidewall aneurysm. This is likely due to the influence of the surrounding vasculature. The rabbit

aneurysm is just downstream of a large branch (LCCA) and lies on a curve segment of artery. Curvature has been shown to affect flow in sidewall aneurysms in human models [100, 101].

The spatial distribution of WSS and OSI in and around the rabbit aneurysm sac is typical for large groups of human IA [11, 95]. The ranges in Re and α for the 51 rabbits are also in very good agreement with typical values for humans. However, α only includes information about the frequency of the waveform, not its temporal dependence. The rabbit aneurysms are constructed along extracranial vessels and exposed to low or absent antegrade flow during diastole, in contrast to human, intracranial vessels which are exposed to constant antegrade flow. This is likely responsible for the relatively low WSS maximum and flow rates found in the rabbit model relative to humans. The relatively constant pressure distribution and small deviation from parent vessel pressure inside the aneurysm sac of the rabbit model are also observed in human cerebral aneurysms [7, 98]. This is consistent with the low flow speed and slow secondary recirculation in the sac.

This works extends an earlier study for a smaller number of rabbit subjects in which geometric parameters were measured at two weeks using 2D angiograms and compared to human IAs [71]. In the present work, a much wider range of geometric parameters were determined from 3D reconstructions of the lumen. Hemodynamic results were previously reported in a smaller study of flow in 5 rabbit aneurysms [73] and are consistent with those reported here.

There were a number of limitations to this study. As for most CFD studies of intra-aneurysmal flow, we have assumed the flow domain is fixed (rigid walls). In both human and rabbit aneurysms, the elastin component is absent or nearly absent resulting in much stiffer walls than found in the surrounding arteries. The motion of the aneurysm wall is generally accepted as being of secondary importance compared to geometric and unsteady flow effects [95]. Based on earlier results [94], we applied modified traction boundary conditions at the inlet of the computational domain. In the future, we intend to further evaluate this choice using phase contrast magnetic resonance angiographs in the parent vessels [102].

The identification of the most significant hemodynamic and geometric parameters for aneurysm growth and rupture remains an active area of research. We have confined attention to parameters which are currently considered significant. In some cases, such as for the OSI and NSI, the data is somewhat sparse and the clinical relevance is still under investigation.

While the flow structures and geometry of the rabbit model successfully reproduce those commonly found in human IA including bifurcation and terminal aneurysms, they do not span all type of flow categories identified in humans. Further, it is possible that there is some other important, as yet unidentified aspect of flow that is different in bifurcation and terminal aneurysm geometries. In section 3.4, a new high flow bifurcation aneurysm model will be discussed, and the resulting flow type extends the current coverage of that reported in human intracranial aneurysms.

In this work, we have confined attention to a comparison of geometry and hemodynamics. Future investigations will evaluate growth and remodeling in the rabbit model and compare these results with published data for human aneurysms. The current work lays an important foundation for these studies.

3.2.5 Conclusion

Hemodynamic and geometric features in a commonly used elastase-induced rabbit saccular aneurysm model are qualitatively and quantitatively similar to those seen in large numbers of human cerebral aneurysms.

3.3 CAN ASPECT RATIO BE USED TO CATEGORIZE INTRA-ANEURYSMAL HEMODYNAMICS?—A STUDY OF ELASTASE INDUCED ANEURYSMS IN RABBIT

3.3.1 Background and Purpose

It is desirable to identify and treat high risk lesions prior to rupture. However, the identification of one or more clinically measurable quantities that can be used independently or collectively to predict rupture risk remains elusive. Geometric factors such as maximum sac diameter and aspect ratio (AR = height/neck width) have been considered.

Statistically significant differences in average size of unruptured aneurysms (4-6mm) and ruptured aneurysms (5-8 mm) have consistently been found, [103]. The majority of ruptured aneurysms are less than 5mm, and therefore, this single parameter is insufficient. Ujiie et al. retrospectively studied 201 patients with 207 ruptured and unruptured aneurysms and found that 80% of ruptured aneurysms had an AR larger than 1.6 whereas 90% of unruptured aneurysms had an AR less than 1.6 [75]. Based on an investigation of 774 ruptured and unruptured aneurysms, Weir et al. concluded AR is a useful clinical index [43]. Nader-Sepahi retrospectively studied patients with multiple aneurysms, one of which had ruptured. In 79% of the patients, the higher AR aneurysm had bled [104]. Raghavan et al. found AR to be a better predictor of rupture than any of the aneurysm size factors [93].

Ujiie et al. conjectured the correlation between aneurysm rupture and AR is due to differences in intra-aneurysmal flow. In an experimental study of flow in vein pouch bifurcation

aneurysms in rabbits, they found a single recirculation zone in aneurysms with AR<1.6 and a second slower circulation in the dome of sacs with AR > 1.6. Studies in human IA have identified correlations between intra-aneurysmal hemodynamics and rupture [7, 8, 98, 99].

It is commonly accepted that aneurysm rupture occurs when the mechanical loading exceeds the strength of the aneurysm sac and that local wall weakening occurs in response to the local hemodynamic environment. Ujiie et al conjectured low wall shear stress leads to inflammation and hence to localized degeneration of the wall. However, this conjecture has never been studied, partially due to the unavailability of human aneurysm tissue. Animal models provide a mechanism for investigating this connection.

The objective of the proposed work is to determine whether there are significant differences in the hemodynamics in low and high AR sacs in the elastase induced aneurysm model and if so, where these differences are most pronounced. With this information, future studies of the effect of AR on growth, remodeling and damage in the rabbit model can be planned. Further, this information can guide investigations of the coupling between AR and hemodynamics in human IAs.

In this work, flow as a function of AR was evaluated in 51 elastase induced aneurysm models in rabbits. A broad range of aspect ratios were created using previously developed techniques [105]. The aneurysms considered here are all side wall, formed downstream from a bifurcation. This provides an opportunity to explore the effects of geometry on flow in a fairly controlled setting.

3.3.2 Materials and Methods

Aneurysm creation and image acquisition follow the procedure described in previous sections. Geometric measurements were obtained in section 3.3. The computational fluid dynamic simulation was done using the method shown in section 3.3, and the results were post processed and analyzed.

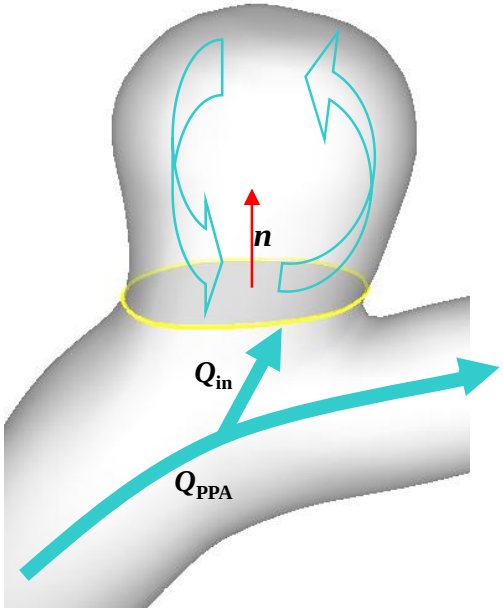

Figure 3.14 Schematic view of flow going through the parent artery and into the aneurysm, red arrow indicates the cross section normal at aneurysm neck.

A non-dimensional flow rate, Q_{ND} was defined as the percentage of PPA flow entering the aneurysm sac at peak systole, (Fig. 3.14D). Hemodynamic features including flow streamlines, velocity magnitude and flow impingement regions were analyzed. Several scalar measures of the wall shear stress vector were considered including its magnitude (WSS), the

time averaged WSS (TAWSS), the oscillatory shear index (OSI) [85] and relative residence time (RRT),

$$RRT = \frac{1}{(1-2\times OSI)\times TAWSS} = \frac{1}{\left|\int_0^T \underline{\tau}_w dt\right|}$$

where T is the duration of one cardiac cycle. The inverse of RRT is an indicator of the distance traveled by a particle close to the wall during time T [106]. The time averaged Reynolds and Womersley were calculated one diameter upstream of the aneurysm neck. Here V is the cross sectional average velocity, further averaged over one period.

3.3.3 Results

Flow structures

The intra-aneurysmal flow could be categorized as three types with type I having a single circulation, type II flows having a single circulation with an inflection in the streamlines and type III flows displaying two circulations, (Figs. 3.15 and 3.16). Of the 51 aneurysms studied, 28 were of type I, 5 of type II and 18 of type III, (Fig. 3.15). In all cases, flow entered the distal sac and exited the proximal sac. In type II flows, an inflection point appeared during diastole and the relative position of inflow and outflow streamlines shifted. In type III flows, a second transient recirculation appeared in the upper sac during diastole causing a reversal in flow direction at the top of the sac and a separation point to appear at the proximal wall, (Fig. 3.16C). The projected streamlines traced a figure eight rather than appearing as two distinct vortices of the type found in driven cavity flows. In comparing streamlines for late diastole in Figs. 3.16B and C, it appears

the increasing AR caused the inflected streamlines of type II flows to undergo an out of plane rotation to form the secondary recirculation of type III flows.

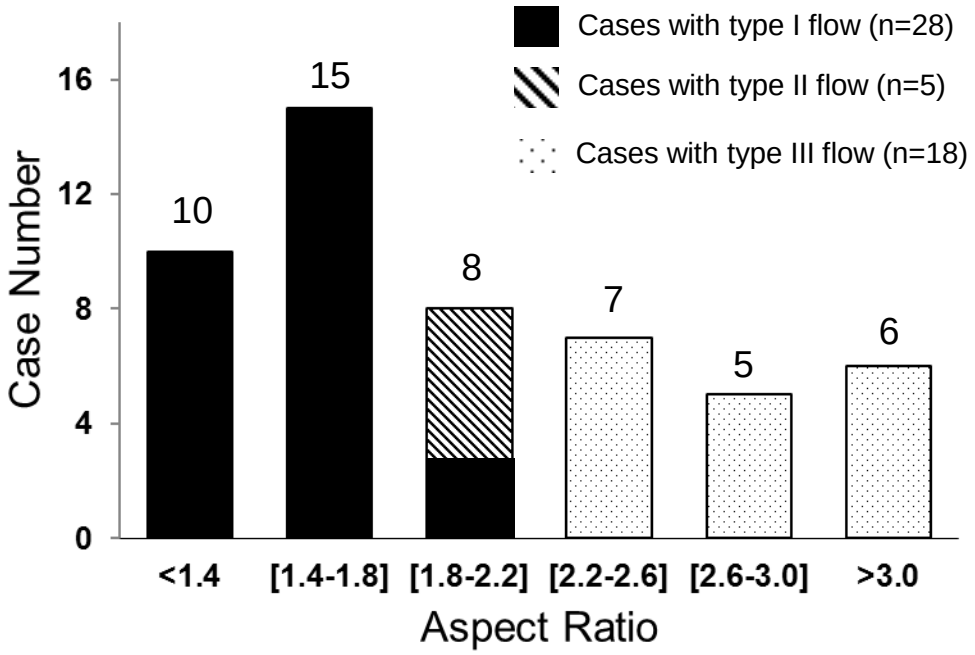

Figure 3.15 Distribution of AR and flow types for rabbit aneurysm models

Correlation of AR and other geometric indices with flow types

All sacs with AR < 1.8 (n = 25) were of type I while all sacs with AR> 2.2 were of type III (n=18). In the eight sacs with AR in [1.8, 2.2], flow was either of type II (n=5) or type I (n=3). In subsequent discussion, we categorize AR as low, transitional or high corresponding to AR< 1.8, AR in [1.8, 2.2] and AR >2.2, respectively.

The ability of AR and other selected geometric indices to predict flow types I and III was assessed using receiver operating characteristic (ROC) curves, (Fig. 3.17). BF, Dmax/H and H/P

had AUC values over 0.90, whereas NSI and N/P had lower AUC values. Compared to other aneurysm size or shape ratios, AR has the best performance in categorizing the flow types independently. Scatter plots of H, Q_{PPA}, BF, Dmax/H, and H/P for the three AR categories did not demonstrate a strong correlation between these parameters and AR categories (Fig. 3.18). This result shows the independency of AR with other geometric or flow factors, which means AR is a unique factor to be considered in distinguish the flow patterns.

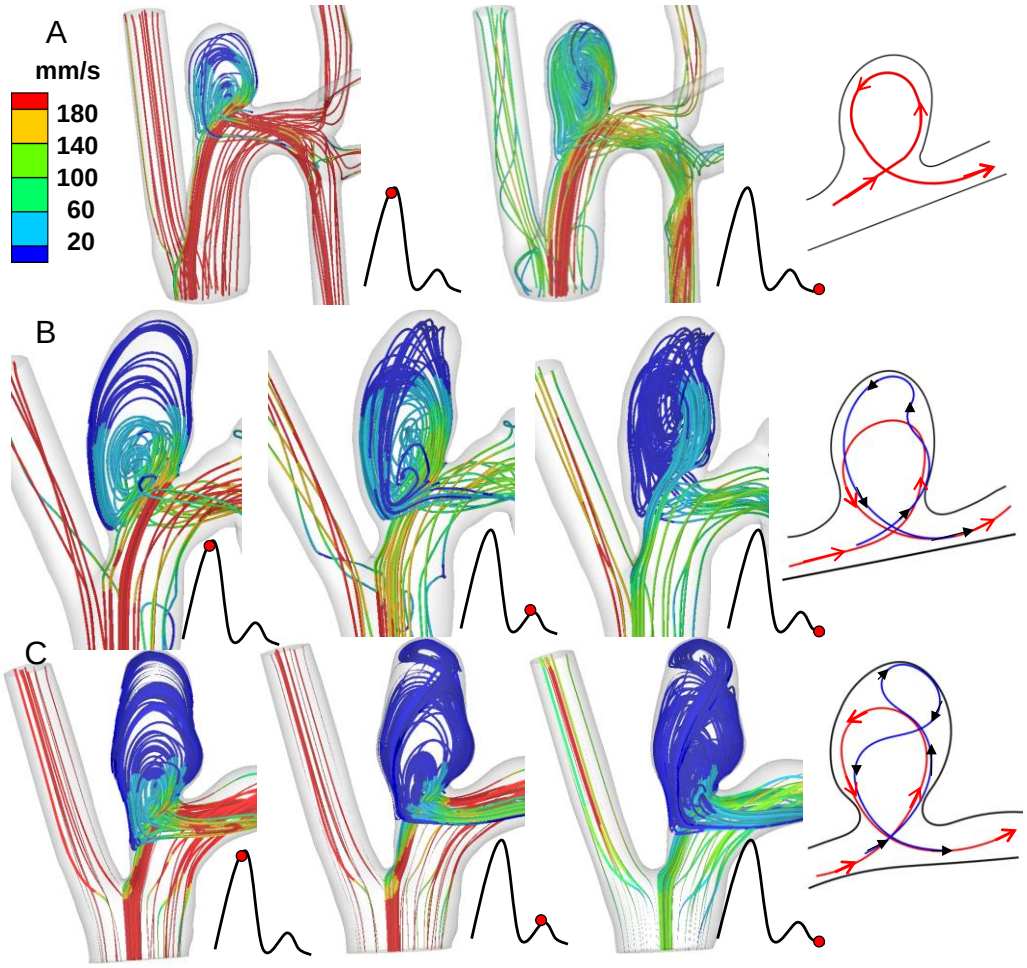

Figure 3.16 Flow streamlines at peak systole, peak diastole and end diastole as well as a schematic of streamlines during end diastole for A) type I, B) Type II and C) Type III flows. The streamline color denotes the velocity magnitude (mm/s).

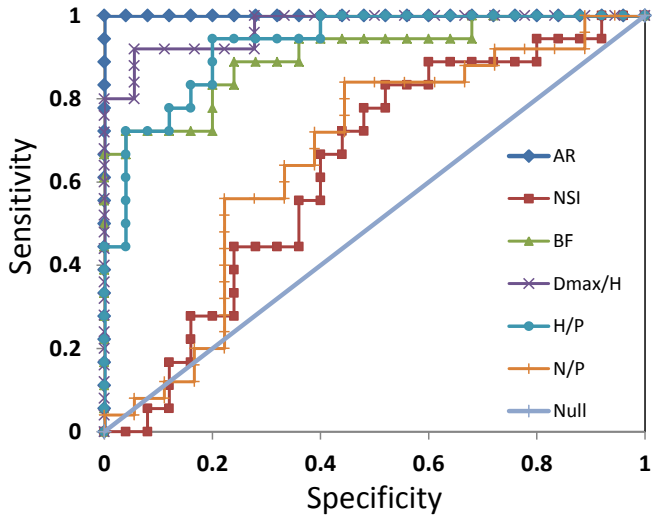

Figure 3.17 ROC curve plots for different geometric indices, the corresponding AUC are: AR=1 NSI=0.63, BF=0.90, D_{max}/H=0.97, H/P=0.92, N/P=0.66.

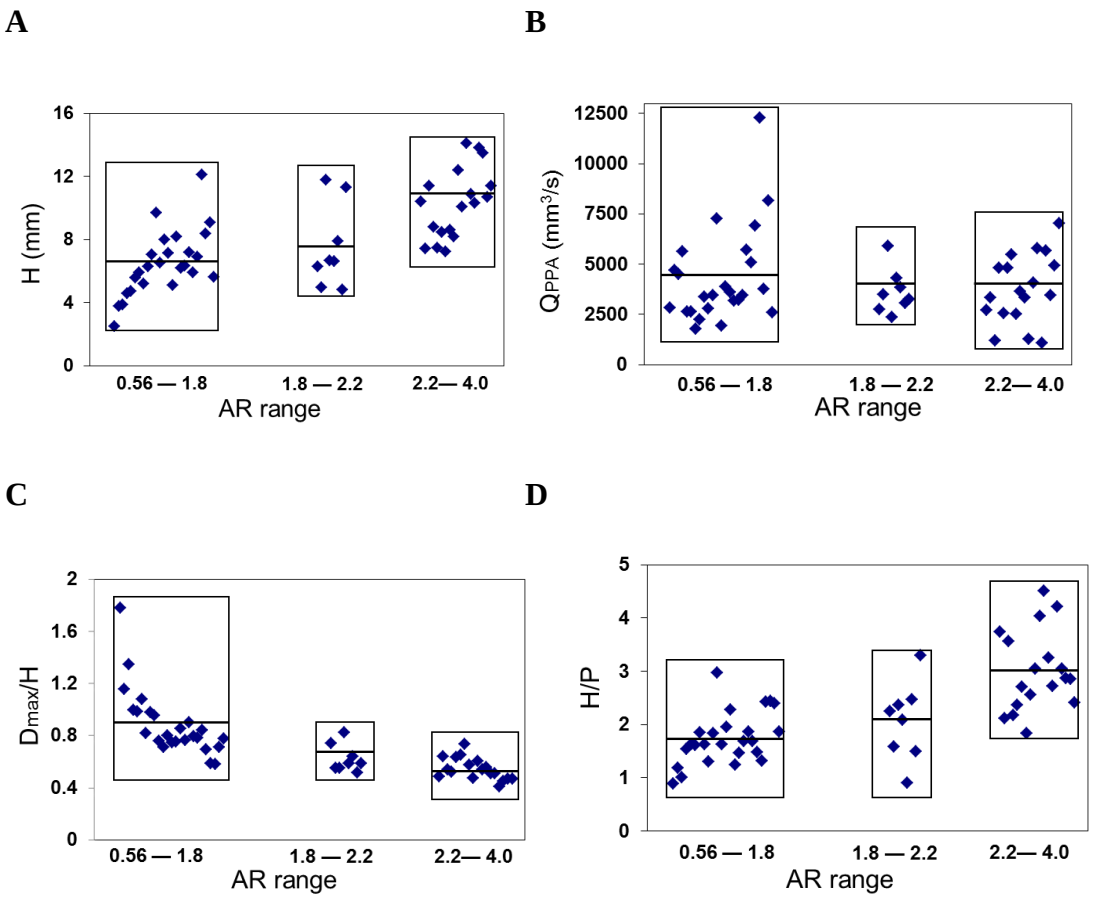

E

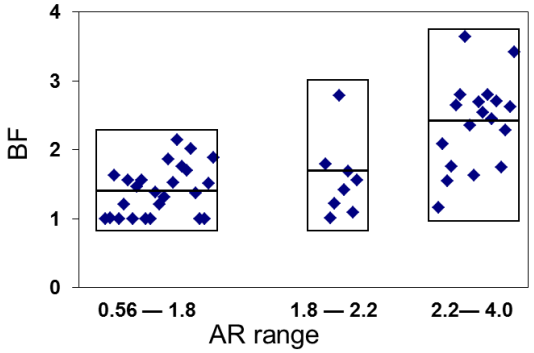

Figure 3.18 Scatter plots of: (A). Aneurysm height; (B). Flow rate at PPA; (C). D_{max}/H; (D). H/P; and (E). BF distributions for three AR categories.

Correlation between AR and hemodynamics

The speed of flow in high AR sacs was diminished relative to low AR sacs with speeds less than 20 mm/s throughout most of the sac, (Fig. 3.16).

For both low and high AR aneurysms, the spatial average of TAWSS ($\overline{TAWSS}$) was substantially lower (< 0.3 Pa) than in the neighboring parent artery, where it ranged from 1.0 to 2.0 Pa, (Table 3.9, Fig. 3.19). The average $\overline{TAWSS}$ was 0.051 ± 0.047 Pa for high AR sacs and increased to 0.20 ± 0.22 Pa for low AR sacs (P=0.02). More generally, a negative correlation between $\overline{TAWSS}$ and AR was found.

Table 3.9 Hemodynamic results in low, transition and high AR models

AR and Hemodynamic features	AR<1.8 (n=25)	1.8<AR<2.2 (n=8)	AR>2.2 (n=18)	P value (between AR<1.8 and AR >2.2 Groups) (95% CI)
AR	1.40 ± 0.32 Range [0.56-1.77]	1.99 ± 0.11 Range [1.81-2.13]	2.86 ± 0.47 Range [2.23-3.98]	--
$\overline{TAWSS}$	0.20 ± 0.22 Range [0.011-1.23]	0.11 ± 0.09 Range [0.02-0.31]	0.051 ± 0.047 Range [0.002-0.18]	=0.02
$\overline{WSS}$ at peak systole	0.68 ± 0.78 Range [0.11-3.22]	0.38 ± 0.38 Range [0.12-1.37]	0.28 ± 0.29 Range [0.02-1.20]	=0.03
% area with TAWSS below 0.1 Pa	42% ± 27% Range [0 -77%] Above 50% n=14 (40%)	71% ± 14% Range [46% -94%] Above 50% n=7 (88%)	82% ± 12% Range [47% - 97%] Above 50% n=17 (94%)	1E-5
Non-dimensional Q	10.4% ± 9.7% Range [1.5% - 49.6%] Less than 10% n=13 (52%)	5.7% ± 6.3% Range [1.2% -21%] Less than 10% n=7 (88%)	4.1% ± 2.5% Range [0.8% - 9%] Less than 10% n=18 (100%)	0.005
Locations of elevated OSI	At neck n=25 (100%) At sidewall n=7 (28%) At dome n=1 (4%)	At neck n=18 (100%) At sidewall n=3 (38%) At dome n=4 (50%)	At neck n=18 (100%) At sidewall n=5 (28%) At dome n=18 (100%)	--
% sac area of RRT >50	Average: 22.6% Above 30% n=10 (40%)	Average: 51% Above 30% n=7 (88%)	Average: 69% Above 30% n=18 (100%)	1E-6
% sac area of RRT >2000	Average: ~0 Above 20% n=0 (0%)	Average: 14% Above 20% n=1 (12%)	Average: 28.6% Above 20% n=12 (67%)	5E-9

A

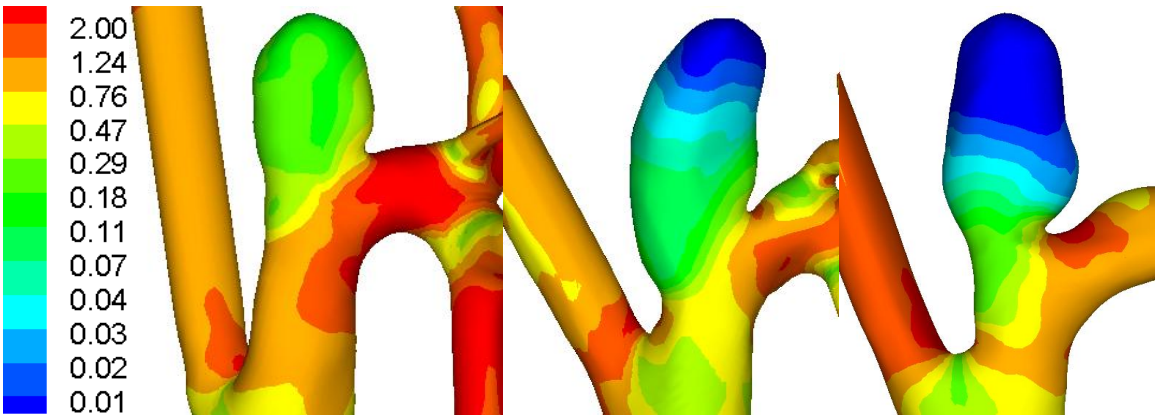

B

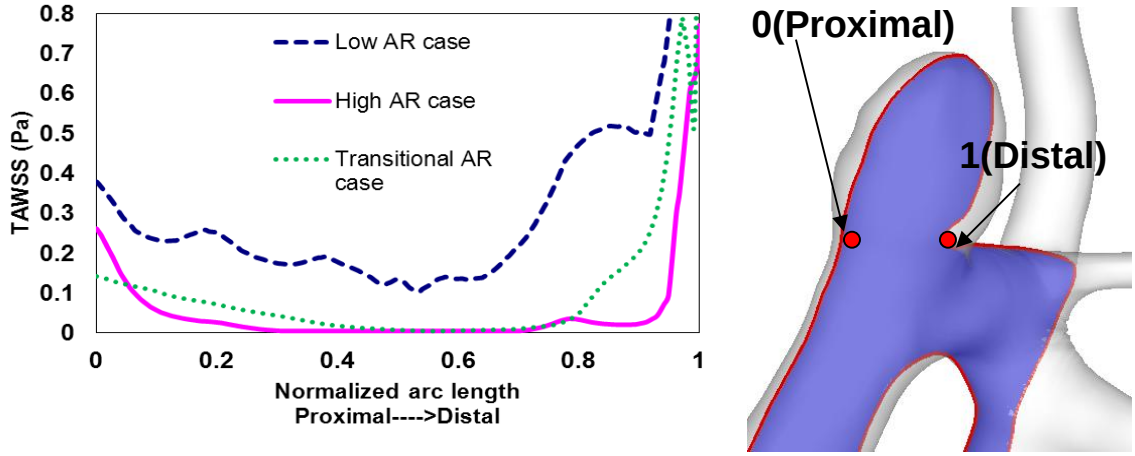

Figure 3.19 A: Typical contours of TAWSS for a flow type I (left), a flow type I case (middle) and a flow type III case (right), using exponential scale; B: TAWSS profiles in the aneurysm sac (left) extracted from intersection curve (right), from proximal neck to distal neck region.

Jou et al. identified 0.1 Pa as a critical WSS value for local aneurysm growth, with largest growth occurring in regions with WSS below this threshold [30]. On average, TAWSS was less than this threshold on 82% of the sac surface in high AR aneurysms as opposed to 42% for low AR aneurysms, (Table 3.9). In fact, in 94% of the high AR cases, more than 50% of the sac had

TAWSS below 0.1 Pa. A positive correlation was found between AR and percent surface area with TAWSS below 0.1 Pa (R=0.69) (Table 3.9).

$\overline{WSS}$ at peak systole was also significantly different between these groups (P = 0.03) with averaging 0.68 ± 0.78 Pa and 0.28 ± 0.29 Pa for low and high AR groups, respectively (Table 3.9). A negative correlation was found between $\overline{WSS}$ and AR (Fig.3.20). The WSS was elevated at the distal neck and wall of the low AR sacs, but only at the distal neck of high AR sacs, (Fig. 3.19).

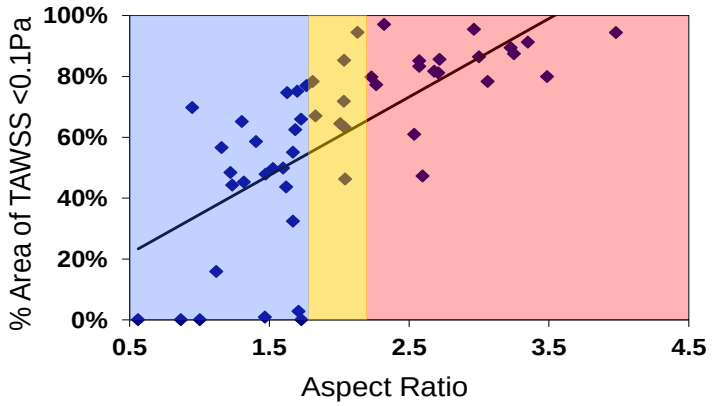

Figure 3.20 AR vs.percentage sac area with TAWSS below 0.1Pa for aneurysms with low AR (AR <1.8, blue), transition AR (1.8<AR<2.2, yellow) and high AR (AR >2.2, red).

A significant difference (P=0.01) was found between QND for the low and high AR groups (Table 3.9). Only three of the fifty-one aneurysms received 20% or more of the parent flow rate. All high AR sacs received less than 10% of the parent flow (Table 3.9).

The OSI was elevated at the neck regions of all sacs (Fig. 3.21). An additional region of elevated OSI was observed at the apex of all high AR cases that was absent in all low AR cases (Fig. 3.21, Table 3.9). The maximum value of RRT is over 2000 for most high AR sacs (73%) and located at the apex of the sac, the location of the transient secondary circulation, (Fig. 3.16, Fig. 3.21). In contrast, the RRT is below 2000 throughout the sacs of 96% of low AR models. A positive correlation was found between AR and percentage area above a RRT cutoff value. For example, R=0.74 for a cutoff value 50 and R=0.82 for cutoff value of 2000, (Fig.3.22).

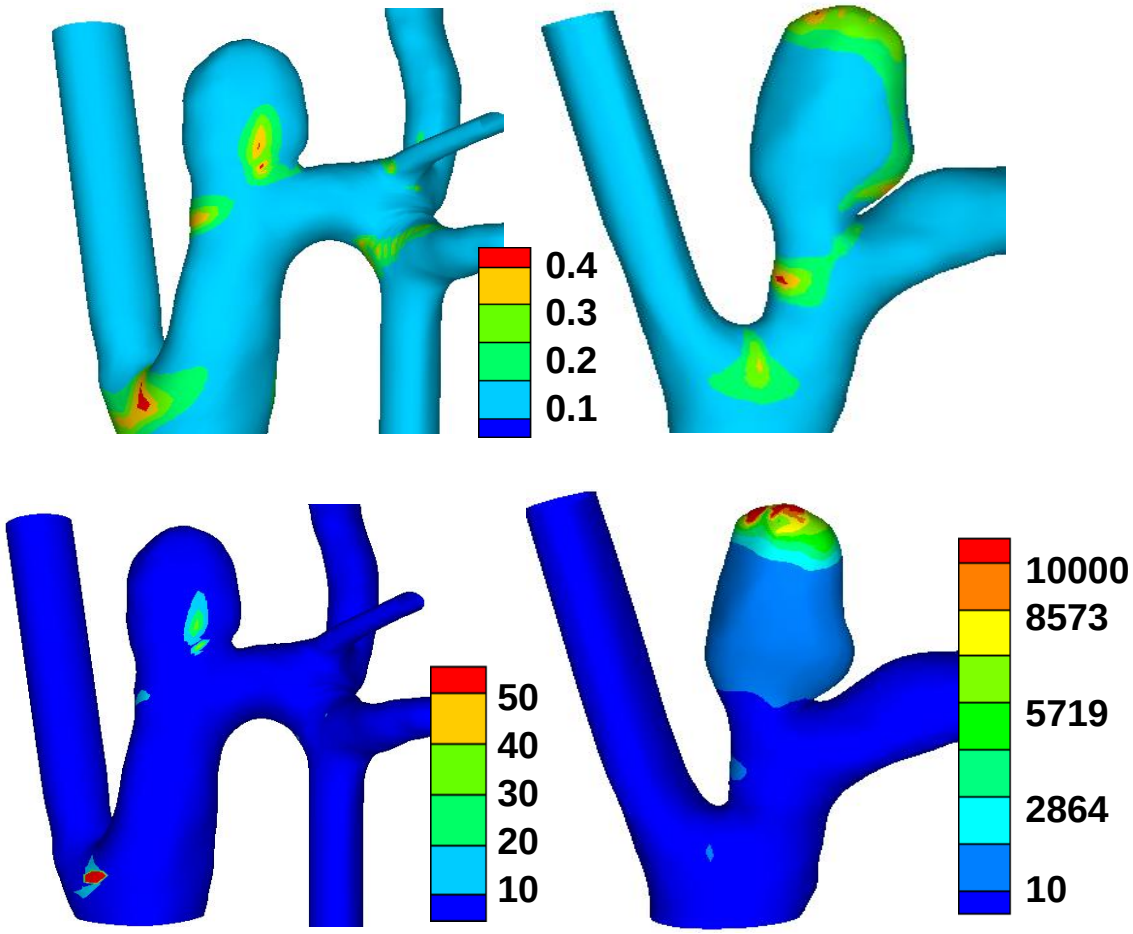

Figure 3.21 Upper row: Contour plots of OSI for a flow type I case (left) and flow type III case (right);Lower row: Contour plots of RRT for a flow type I case (left) and flow type III case (right).

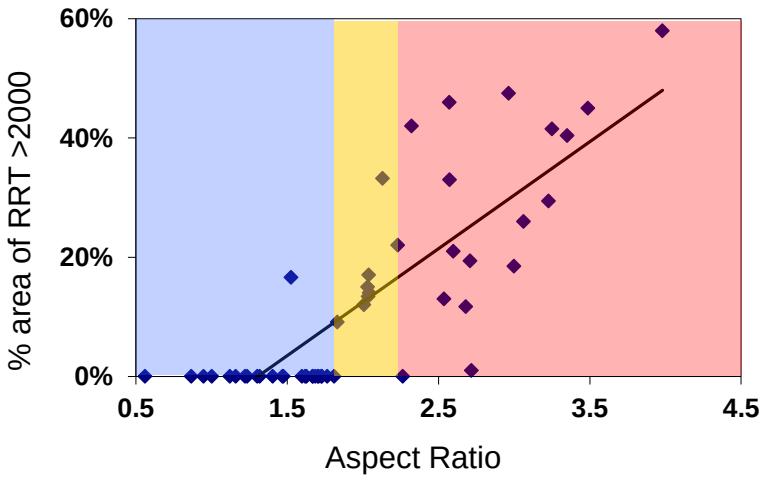

Figure 3.22 AR *vs.* percentage sac area with RRT larger than 2000, for aneurysms with low AR (AR <1.8, blue), transition AR (1.8<AR<2.2, yellow) and high AR (AR >2.2, red).

3.3.4 Discussion

In 1999, Ujiie et al. conjectured AR may be a better index than aneurysm size for planning treatment of unruptured aneurysms due to the role of AR in determining intra-aneurysmal flow [75]. This long standing conjecture has never been proven, despite its clinical significance. It is based on two premises. The first is that hemodynamics in high and low AR aneurysms are different. The second is that high AR flow conditions lead to detrimental changes in the aneurysm wall.

In a previous work, hemodynamics features in the elastase induced aneurysm model in rabbits were shown to be similar to the hemodynamics in a large percentage of human IAs including both bifurcation and sidewall aneurysms [105]. In the present work, we demonstrated

the first premise behind Ujiie et al.'s conjecture is valid in this aneurysm model. Namely, flow in the low and high AR models are significantly different. Low, transitional and high AR categories could be defined such that for all low AR aneurysms, only a single circulation was observed, whereas in all the high AR aneurysms, a transient, slower secondary circulation was also found with an associated separation point. The distinctness of these groups could not be explained by differences in animal specific flow rates between the groups, nor to differences in height.

The current work supports the second premise in that slow, recirculating flow in the high AR models results in hemodynamics conditions that are associated with detrimental changes to the arterial wall. The transient secondary circulation of the high AR model is slower than the primary circulation of both the low and high AR models. This leads to a lower WSS, elevated OSI and higher RRT in the dome. The negative correlation between AR and WSS was also observed in a study of 20 human aneurysms [8]. Regions of pathologically low WSS have been positively correlated with aneurysm growth in humans [8, 99], and high OSI has been tied to increased development of atherosclerosis and local wall remodeling [107, 108]. Elevated OSI and RRT values in arteries are associated with altered endothelial permeability and lesion formation [106, 108]. Thus, the upper sacs of the high AR aneurysms tend to have unhealthy hemodynamic environments which may trigger wall degradation and general mechanical weakening.

This work lays the foundation for a deeper investigation of the second premise. Differences in the histology in low and high AR models will be evaluated in the context of local hemodynamics. In a related work in this direction, differential gene expression was compared in

high and low AR aneurysms from eleven animals included in the present study [109]. In that work, high AR was associated with differential expression of inflammatory/immunomodulatory genes, structural genes, and genes related to proteolytic enzymes, and extracellular matrix-related genes.

Another interesting finding was the existence of transitional flow type in the intermediate AR group, supporting the use of categories of low, high and transitional AR when assessing rupture risk. While most clinical studies identified a statistically significant difference between AR in ruptured and unruptured aneurysms, there is some disagreement about whether a threshold exists and if so, where it lies. As noted by Lall et al., aspect ratios between 1.6 and 2.2 are consistently considered borderline in risk [103]. This range is close to that identified here as transitional. The rabbit model has been used to evaluate novel flow altering treatment strategies such as flow diversion and coiling. Based on the current work, it would seem advisable to interpret results from such studies in the context of low, transitional and high AR groups.

While AR has been found to be a meaningful clinical indicator in human studies, some caution should be taken related to selection bias, lack of prospective studies, the observation of aneurysm geometry at only one time point and the variety of definitions used for AR. Another confounding factor is the use of 2D angiograms versus 3D reconstructions of clinical data. Due to image resolution issues, the neck of the aneurysm may be overestimated in 3D DSA while the use of 2D projections may introduce errors due to asymmetries in the aneurysm sac.

There are some limitations to our study. On the basis of earlier results, we applied modified traction boundary conditions at the inlet of the computational domain. In the future, we intend to use phase-contrast MR angiograms in the parent vessels. [102]. Several idealizations have been included in the model. Motivated by the lack of elastin in the arterial wall, the aneurysm wall has been modeled as rigid. Further, the blood has been idealized as Newtonian.

It will be valuable to determine whether the distinct flow categories identified in this work, carry over to a wider range of vascular geometries such as bifurcation aneurysms. Ujiie et al. identified these similar flow categories in low AR (<1.6) and high AR (> 1.6) in surgically created bifurcation aneurysms in rabbits [75]. Based on their study of flow and rupture in 68 human saccular aneurysms, Hassan et al. concluded that AR may be a useful index for predicting rupture in side wall aneurysms with and without branches, while other geometric factors likely play an important role in end wall aneurysms [9].

3.3.5 Conclusion

Low AR (AR<1.8) and high AR (AR>2.2) categories with distinct intra-aneurysmal flow were identified in 51 elastase-induced rabbit aneurysms. A third transitional flow type was identified in the intermediate range. Flow in high AR aneurysms appears to be more deleterious to the wall, displaying larger regions of pathologically low WSS, elevated OSI and elevated RTT. Future studies will be directed at evaluating differences in wall remodeling in these distinct flow environments.

3.4 A NEW HIGH FLOW BIFURCATION MODEL

3.4.1 Background and Purpose

In our previous studies of the elastase induced aneurysm model, the aneurysm was formed from the right common carotid artery (RCCA). Section 3.2 described studies of 3D reconstructed geometries for 51 cases, the aneurysm size and non-dimensional shape factors were shown to be within the range reported for human IA [105]. As shown in section 3.2, two flow types were identified: Type A flows displayed a single, stationary circulation inside the aneurysm sac while Type B flows also had a transient secondary recirculation. Cebral et al. classified flow in 62 cerebral aneurysms in humans into four flow types [7]. Flow types A and B in the previous rabbit aneurysm models correspond to flow types I and III in that study, respectively, covering 61% of the IA analyzed in [7].

On the other hand, with CFD tools and new techniques for creating geometric configurations in the rabbit aneurysm model, we are working with the Mayo collaborators and exploring the possibility of covering more flow types found in human IAs. Before investing a large amount of effort to create the aneurysm model and test in vivo, we will use CFD as a tool to assist design of the new animal model. The objective of this section is to perform " in silico design" of the animal model, and explore the possibility of generating more flow types in the rabbit aneurysm model by altering the flow waveform and geometry [110].

3.4.2 Materials and Methods

New geometric configuration

Our collaborators at the Mayo Clinic were able to create an elastase induced aneurysm at the left common carotid artery (LCCA) using technique similar to those reported in earlier sections for the RCCA aneurysm models. This will be referred to as the LCCA aneurysm to distinguish it from previously created RCCA aneurysm model (Fig.3.23) [77]. The RCCA aneurysm is a sidewall aneurysm while the LCCA aneurysm is a bifurcation aneurysm (Fig.3.24).

New flow waveform

Previous experimental aneurysms were constructed along extracranial vessels, which subserve vascular beds of high resistance, and low diastolic flow. Indeed, these same vascular beds often demonstrate reversal of flow in early diastole. In contrast, the human, intracranial vasculature is typified by low resistance, high diastolic flow patterns, that satisfy the critical need for brain oxygenation. To achieve a similar flow environment in human intracranial vasculature, our collaborators in the Mayo Clinic surgically created an arteriovenous fistula (AVF) distal to the aneurysm cavity. This resulted in high rates of flow during diastole in the neighborhoods of the aneurysm , thus offering a wave form similar to that of humans (Fig.3.23).

In vivo measurements

Standard digital subtraction angiography and three dimensional rotational angiography (3DRA) (Siemens Medical Systems, Erlangen, Germany) were performed 12 weeks after aneurysm creation. The 3D geometric models of the aneurysm and sections of local vasculature

were reconstructed from the serial image data using Mimics software (Materialise Inc., Leuven, Belgium). Arterial waveforms were captured distal to the aneurysm upstream of the LCCA, in the descending aorta and in the left subclavian artery using transthoracic Duplex Doppler ultrasound (ACUSON Sequoia 512 machine with a 15L8 transducer, Siemens Medical Solutions, Erlangen, Germany). Phase contrast MRA measurements were taken at the aortic arch in order to provide rabbit specific boundary conditions for the CFD studies (Fig.3.24).

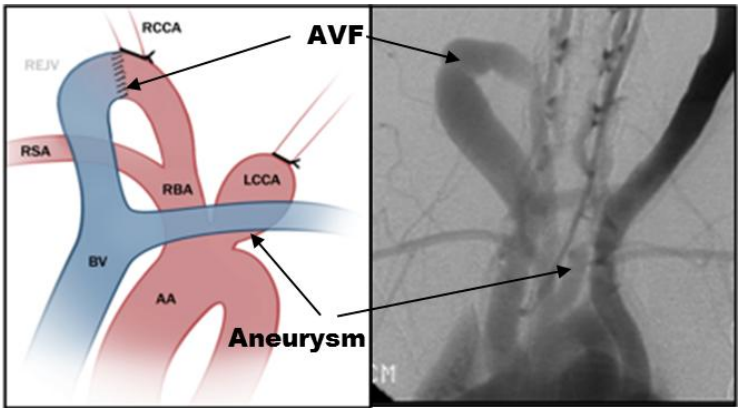

Figure 3.23 The elastase induced bifurcation type aneurysm and AVF in rabbit (left: schematic of creation; right: 2D angiogram of aneurysm and AVF).

CFD study

The CFD simulation was similar to that described in Section 3.1, with the exception that pc-MRA measured data was used for the inlet boundary condition of ascending aortic arch. The 3D velocity profile from pc-MRA measurements were fit to the inlet mesh of the aorta (Fig.3.24).

To explore the new flow type, CFD simulations were conducted using several combinations of flow waveform and geometric configuration, and AR categories (Fig. 3.25).

Specifically, besides the RCCA model with low flow waveform (Model A, Fig.3.25) that we have studied in previous sections; we analyzed the combination of: RCCA model with high flow waveform (Model B, Fig.3.25), LCCA model with low flow waveform (Model C, Fig.3.25), and LCCA model with high flow waveform (Model D, Fig.3.25).

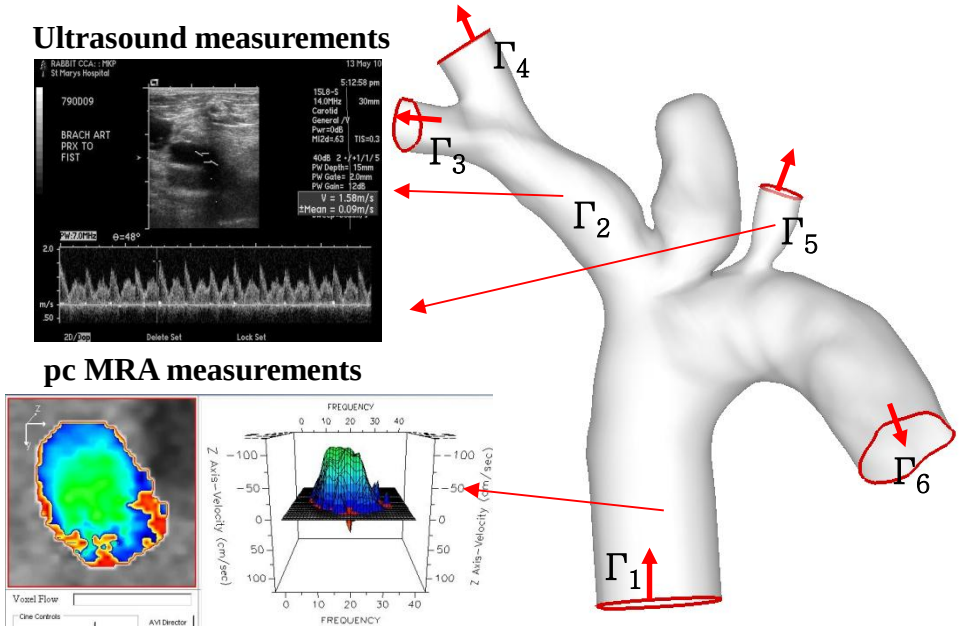

Figure 3.24 Computational domain and flow measurements.

3.4.3 Results and Discussion

The resulting high flow waveform after the AVF creation is shown in Fig. 3.26. Compared to the previous model, the new waveform has an antegrade flow during diastole, which substantially increased the inflow into the aneurysm sac in some geometries.

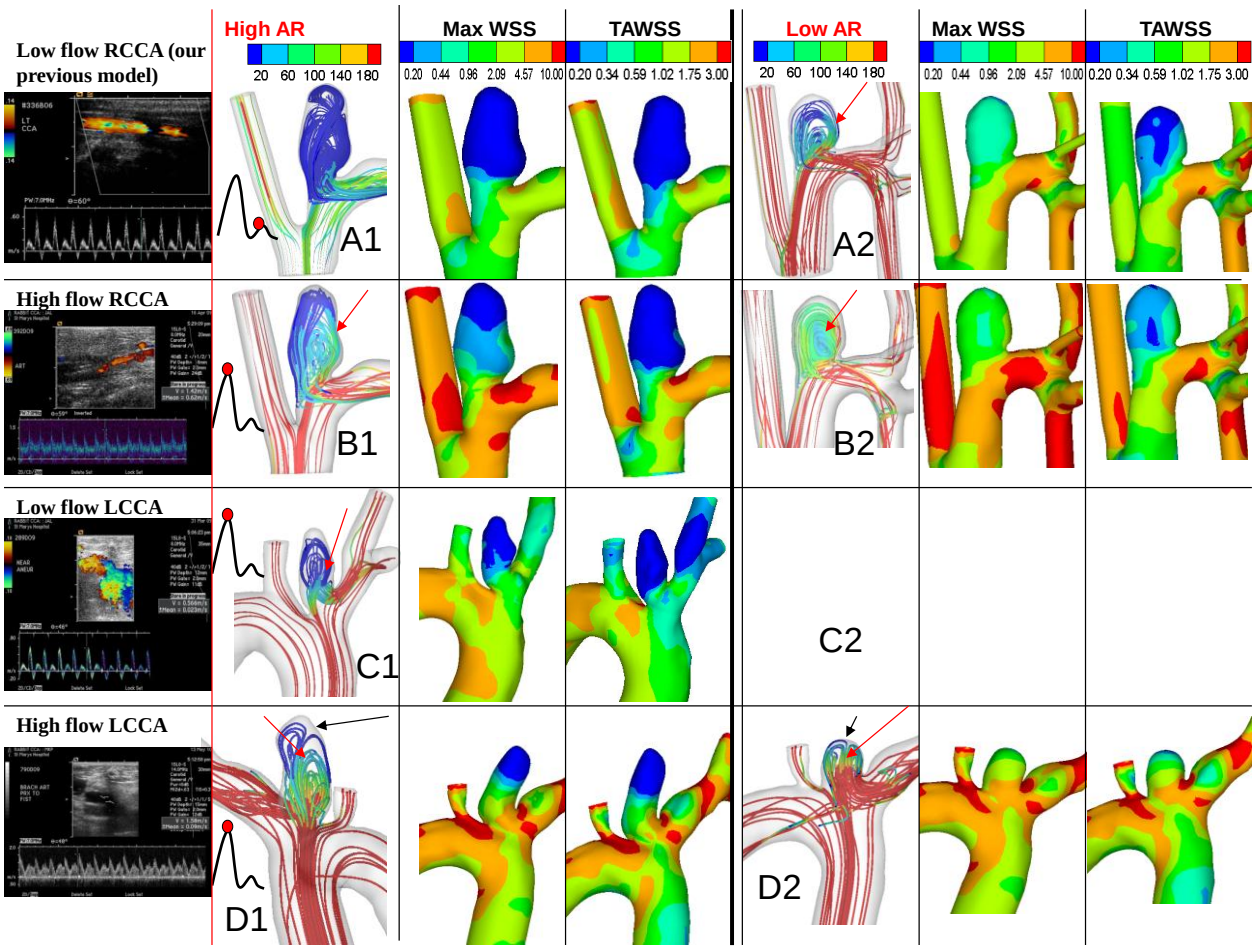

Figure 3.25 Summary of representative WSS of RCCA aneurysm models and LCCA aneurysm models.

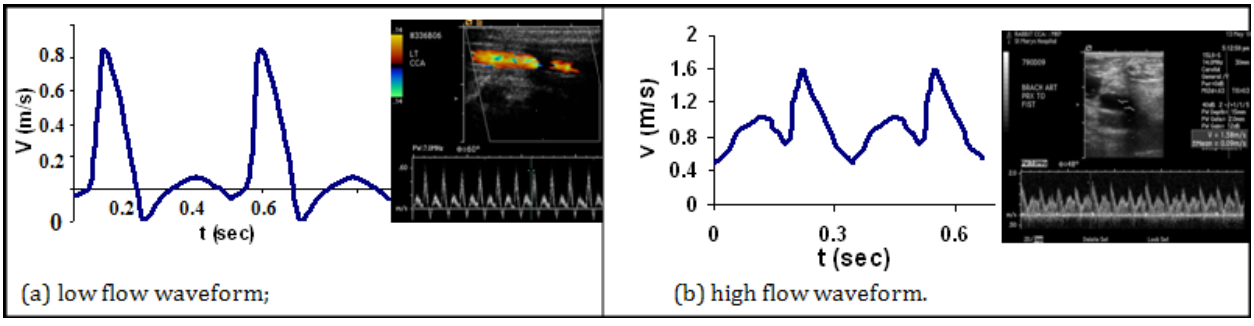

Figure 3.26 Ultrasound flow waveform: (a) low flow used in RCCA aneurysm models, (b) high flow (antegrade flow waveform) used in LCCA aneurysm models.

The new LCCA bifurcation aneurysm model with high flow waveform (Model D) was found to display a third flow type reported in [7] for both low and high AR aneurysm sacs. The intra-aneurysmal flow is characterized by two stationary circulations throughout the entire cardiac cycle (Fig.3.27). Inflow is substantially higher compared with the RCCA aneurysm model (Model A). The incoming jet impinges higher up in the sac and displays an oscillating impingement point (Fig.3.27, arrows). Further, there is a significant increase in WSS inside the aneurysm sac (Fig.3.25). The maximum TAWSS inside the aneurysm sac increased from 20 dynes/cm^2 in the RCCA low AR model to 40 dynes/cm^2 in the LCCA low AR model. The new flow type C (Fig. 3.26) corresponds to flow type II in [7], not previously seen in the RCCA aneurysm model. It is similar to a bifurcation type flow which is commonly associated with human IA [7] and is associated with increased risk of rupture compared with the previous two flow types.

The results of other combinations of geometric configurations and flow waveforms were also presented in the Fig. 3.25. Except the LCCA aneurysm model with high flow waveform (Model D), other types of combinations don't display new flow types. In particular, in Fig.3.25, Models B1, B2 and C1, all present the flow type A. Given the similarity of geometric configuration to C1 combined with the low AR of its sac, Model C2 is expected to have type A flow, the evaluation of Model C2 was omitted here. Base on this, we can exclude these combinations from the future animal aneurysm creation.

A bifurcation, elastase-induced aneurysm model will be useful for numerous reasons. First, this type of morphology is extremely common among human, intracranial aneurysms.

Second, development of devices as well as the study of aneurysm physiology would be facilitated by studies in this type of model aneurysm.

Creation of the ante-grade flow described above will have substantial impact on the relevance of the animal model. First, the application of animal models for the development and validation of CFD modeling requires clinically relevant flow patterns. Second, recanalization rates following device placement likely will be impacted by the elevated, trans-cardiac cycle hemodynamic stress provided by high diastolic flow rates. Third, preclinical study of the growth and remodeling of aneurysms in relation to flow requires realistic flow patterns. Finally, gene and protein expression likely will be affected substantially by these flow patterns, and thus successful development of this model will facilitate numerous lines of ongoing research.

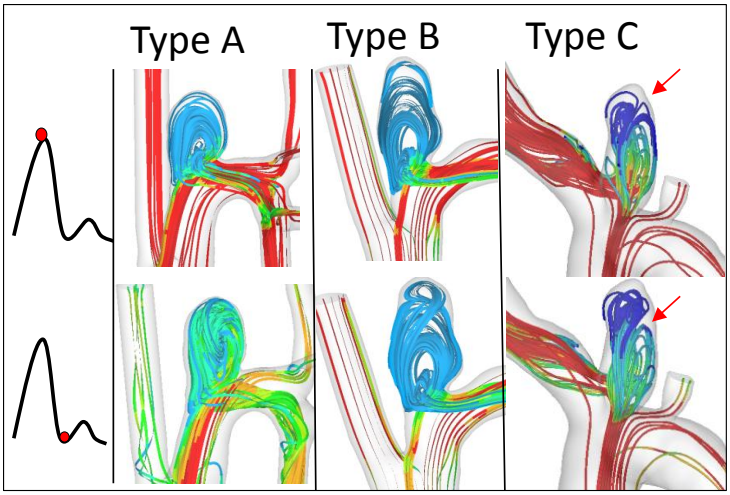

Figure 3.27 Streamlines for flow type A (RCCA-aneurysm); type B (RCCA-aneurysm) and type C (LCCA-aneurysm). Arrows denote the shifting impingement point in a cardiac cycle during systole and diastole.

The CFD aided “in silico design” of the new aneurysm model is a new approach in conducting animal model research. Using the simulation technique to explore the possible outcome of the animal model will give insight into the actual model creation, and also save time and resources compared with a trial and error approach to the model creation. We expect this technique will be widely used in animal model studies in the future.

3.4.4 Conclusion

An elastase-induced aneurysm at LCCA in rabbit was created that is of bifurcation type, in contrast to the previously created sidewall type. A high flow antegrade waveform in the peri-aneurysmal region was achieved by placing a downstream AVF. The “in silico design” approach demonstrates the intra-aneurysmal flow of high flow LCCA aneurysm model leads to a third of the four flow types identified in [7], and was not previously seen in the RCCA-EIAR model. Hence, this new aneurysm model extends the range of applicability of the elastase induced aneurysm model in rabbits.

3.5 SUMMARY OF ELASTASE INDUCED ANEURYSM MODELS IN RABBIT

In this chapter, an elastase induced aneurysm model in rabbits has been shown to provide similar geometries and hemodynamic environments to those seen in humans. A detailed sensitivity study was done to choose an efficient and accurate computational domain and boundary conditions of the rabbit aneurysm models (section 3.1). CFD analysis has shown that three of the four flow types identified in human IAs can be created using a previously created RCCA model as well as a new high flow LCCA model (section 3.2 and section 3.4). A wide range of ARs can be created in the rabbit model. CFD studies demonstrate distinct flow types in low and high AR models. Flow in the high AR aneurysms appears to be more deleterious to the wall including larger regions of pathologically low WSS, and elevated OSI compared with the low AR sacs (Section 3.3).

This work lays the foundation for future applications of the rabbit aneurysm models to studies of the coupling between local intra-aneurysmal hemodynamics and wall structure. A current area of investigation is the capability of wall of the rabbit aneurysm model for growth and remodeling. The remodeling of the aneurysm, especially, the enlargement of the aneurysm sac after 3 weeks of creation was observed in an earlier study of this rabbit aneurysm models [111]. The biological response of the aneurysm wall was previously examined by our collaborators in the Mayo Clinic, and differences in P-Akt expression were found in the aneurysm sac of high and low AR models [73].

In a related work in this direction, differential gene expression was compared in high and low AR aneurysms in 11 rabbit aneurysm models [112]. High AR was associated with differential expression of inflammatory/ immunomodulatory genes, structural genes, and genes related to proteolytic enzymes, and extracellular matrix-related genes.

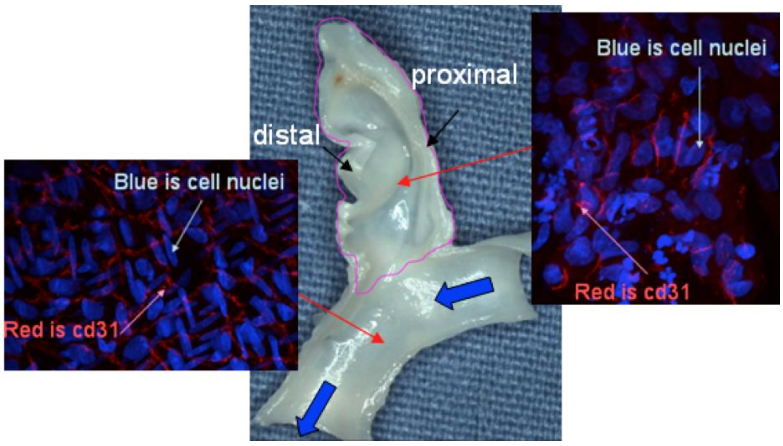

Figure 3.28 Confocal images of en face preparations of the vessel wall showing the scattered EC in the aneurysm wall inner surface. Picture taken and provided by Michael R. Hill, with permission.

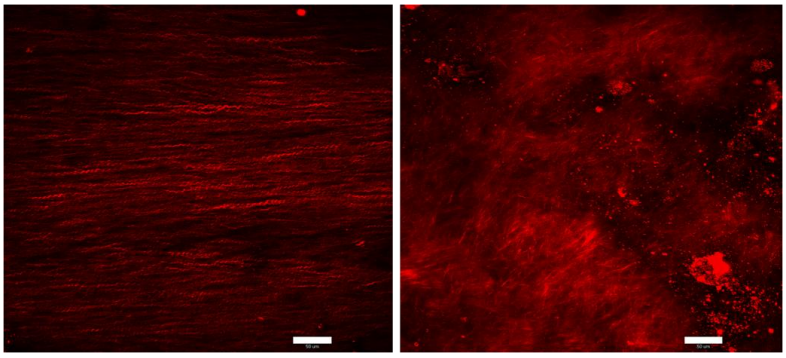

Figure 3.29 Multi photon images of rabbit control artery wall (left) and rabbit aneurysm wall (right) showing difference in collagen alignment between aneurysm and control artery. Picture taken and provided by Michael R. Hill, with permission.

Endothelial cells were found along the intima of the rabbit aneurysm sacs. They are more disordered and less uniformly distributed than in control arteries (Fig.3.28). The multiphoton microscopy images showed substantial differences in collagen alignment in the rabbit aneurysm wall compared with the control artery, which provides clear evidence of wall structural remodeling after the aneurysm model creation (Fig. 3.29). Future studies will be directed at rigorously assessing wall remodeling and degradation in the elastase induced aneurysm model to evaluate its relevance to humans. In the future, studies on growth and remodeling of the rabbit aneurysm wall will be correlated with the hemodynamic forces to provide insights on pathophysiology of human intracranial aneurysms.

This animal model is not intended to be used for studies of aneurysm initiation since the sac is constructed using elastase. It is also unlikely that it will be practical to study the rupture process until we know more about growth and remodeling in this model. The rupture rate of human saccular aneurysms is quite low- much less than one percent per year. If a similar rupture rate is reproduced in the animal model, we would need to study 500 animals for approximately a year to obtain five ruptured aneurysms. This is clearly impractical, both for the duration and quantity of the study. However, once we better understand the growth and remodeling process, we may be able to focus on long term studies of rabbit geometries that are more likely to be unstable. In any case, the rabbit model provides an opportunity to study biological response to the abnormal hemodynamics found in the aneurysm sac. This includes the effect of the intra-aneurysmal hemodynamics on the growth, remodeling and damage process.

4.0 DEVELOPMENT OF A PARAMETRIC MODEL FOR HUMAN INTRACRANIAL ANEURYSMS

4.1.1 Background and Purpose

Regional differences in hemodynamic loads on artery walls have been associated with localized vascular disease such as atherosclerosis and intracranial aneurysms (IA). Intracranial aneurysm rupture represents the leading cause of devastating, spontaneous subarachnoid hemorrhage [113, 114]. The physiologic and hemodynamic mechanisms of initiation, growth and rupture of saccular aneurysms remain unclear. However, hemodynamic factors such as WSS, flow impingement, OSI, and residence time are thought to be important in aneurysm pathophysiology [37, 108, 115]. In vivo measurements of these factors are extremely difficult or impossible. Thus, numerical simulation and in vitro experiment are more applicable in obtaining these hemodynamic factors. 3D reconstructions of aneurysms from patient specific data are frequently used in preparing computational fluid dynamics (CFD) models to apply hemodynamic studies [7, 8, 95]. These 3D reconstructed models can provide accurate anatomies of aneurysms and their surrounding vasculature thus lead to local estimation of the hemodynamic factors. However, due to the pipeline used in this kind of geometric reconstruction and realistic geometry complexity, it is not possible to use them to systematically vary geometric features for parametric studies.

Idealized models of IA have been created for hemodynamic studies, but they are limited by their tendency to oversimplify the geometry, thus not suitable for studying geometric parameters and shape factors of aneurysms. A methodology to create parametric models of arterial bifurcations that can reproduce all the common geometric features of cerebral arterial bifurcations has been previously developed [116]. Comparison of CFD results confirmed that these models also have the ability to reproduce the hemodynamic features of arterial bifurcations.

The purpose of the present study is to build on earlier work to design and validate parametric models for intracranial aneurysms and their surrounding vasculature. Here, we focus on two categories of IAs, side wall aneurysms and bifurcation aneurysms with different sizes and AR [9]. As will be discussed below, methodology we have developed is relatively simple, yet creates parametric models that capture key geometric and hemodynamic features which have been hypothesized to be important in cerebral aneurysms pathology. In addition to applications for human IAs, this model has applications to studies of animal models. In the previous chapter we presented a new approach of "in silico design" of the rabbit aneurysm models. To facilitate the computational method, a parametric model will be helpful in exploring the effect of different geometric features on intra-aneurysmal flow type. With a parametric model in hand, we will be able to construct the model geometry using known animal model configurations and available geometric manipulations, and predict the outcome of different model creation methods.

4.1.2 Materials and Methods

Real (reference) geometry reconstruction

Four representative human IA cases were selected for developing parametric models. These geometries include two side-wall IAs: one low aspect ratio (AR=1.2, Model A) case and one high AR (AR=2.8, Model B) case, both located at internal carotid artery; and two low AR bifurcation IAs (AR=1.4, Model C and AR=0.9, Model D) located at the tip of basilar artery and anterior communicating artery respectively. The lumen surfaces were reconstructed from 3D DSA data as previously described in Section 3.1 (Fig. 4.1).

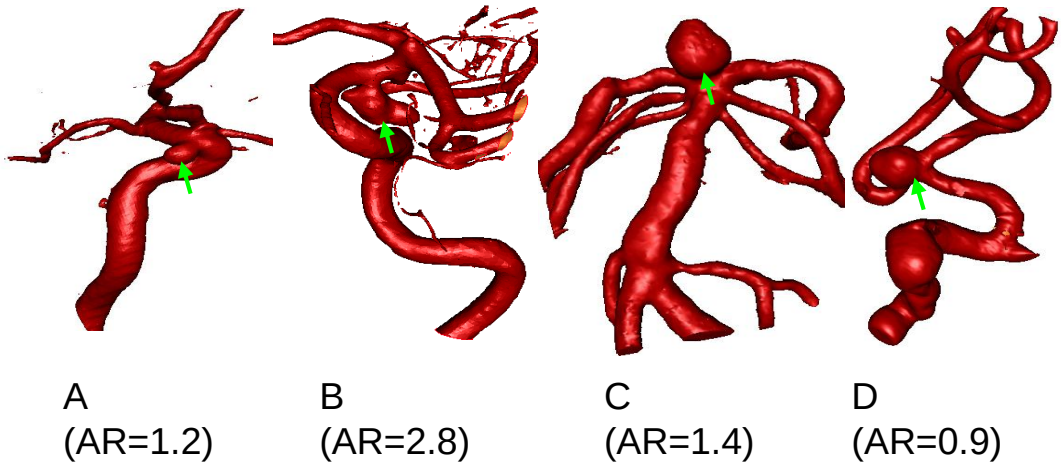

Figure 4.1 Four ICAs and their surrounding vasculature reconstructed from 3D DSA data sets; arrows indicate the aneurysms.

Parametric model development

From the reconstructed 3D original geometries, the centerline points of surrounding vascular and aneurysms were calculated (Fig. 4.2a). The centerline fitting algorithm was based on a

discretized 3D distance field. The reconstructed 3D model was rasterized uniformly using the resolving resolution as discretization parameter. For each voxel, the minimal distance to the surface boundary was calculated, after which the centerline point was selected as the point with a maximum Euclidean distance from the boundary. At each centerline point, a cross section was defined normal to the centerline, the plane normal was obtained and a "best fit" diameter was calculated based on least square fitting (Fig. 4.2b). This centerline calculating algorithm was implemented using MIMICS software.

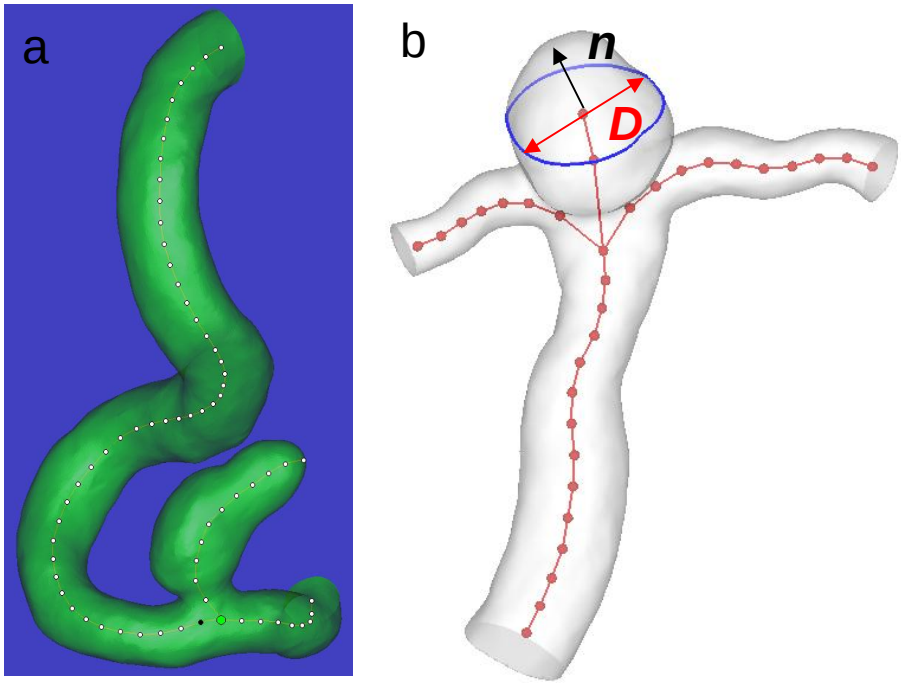

Figure 4.2 a: centerline points calculated from the reconstructed geometry (model B); b: cross section normal and best fit diameter associated with a centerline point.

Fig. 4.3 shows the schematics of the steps used for developing the parametric model for one side wall aneurysm model (Model B) and one bifurcation aneurysm model (Model C). The development pipeline of the parametric model is as follows:

I. The centerline point coordinates and associated cross sectional information (normal and diameters) were calculated and extracted from the reconstructed 3D geometry (Fig. 4.3. a1 and b1).

II. The centerline points and cross sectional information were tabulated as numerical values, using the datum points function, the text file were imported into Pro/ENGINEER software (PTC., Needham, MA, USA) to create the points of centerline. A spline function is used to connect these centerline points together to form the centerline. Each cross section is created using from a sketch on the plane which is crossing the centerline point and perpendicular to the local curvature of the centerline, after which a skeleton of parametric model was generated (Fig. 4.3. a2 and b2).

III. The parent vasculature was generated using an approach similar to that used in our previous study [116] (Fig. 4.3. a3 and b3). For the side-wall cases (Models A and B), the parent artery was generated by using the sweep blend function in Pro/E along the centerline skeleton created in "II". During the volume extrusion, the control cross sections were selected at the relatively high curvature regions of the artery. For the bifurcation cases (Models C and D), a parametric model of the bifurcation was generated by merging two arterial segments together with a common inlet (Fig. 4.3 b3). The center line point coordinates, cross section normal and effective radii of three

cross sections (one parent and two daughter cross sections) from the original bifurcation were used to provide geometric information and sweep blending basis [117] during bifurcation development. For simplification of the current model development, all the vessel cross sections were circular.

IV. The aneurysm geometry was generated using its centerline and three critical cross sections: neck cross section (C1), cross section of maximum area (C2) and an intermediate cross section (C3) between C2 and apex of the centerline (Fig. 4.3. a2 and b2). Elliptic cross sections were used for C3 in Model A and B only. The remaining cross sections were circular. For the high AR aneurysms, the aneurysm centerline was directly calculated, and for low AR aneurysms, the centerline was linearly extrapolated by using the center of neck cross section, the geometric center of aneurysm sac, and the apex point of aneurysm sac (defined as the point on the aneurysm sac which has the largest distance to the center of neck cross section). The parametric aneurysm sac model was then merged to the parametric models of the parent vasculature, to form the complete parametric model.

V. Following the merging of aneurysm and parent vasculature, the unphysical sharp junction between the aneurysm and the parent artery were rounded using the round function in Pro/E. The final constructed models are shown in Fig. 4.3 a4 and b4.

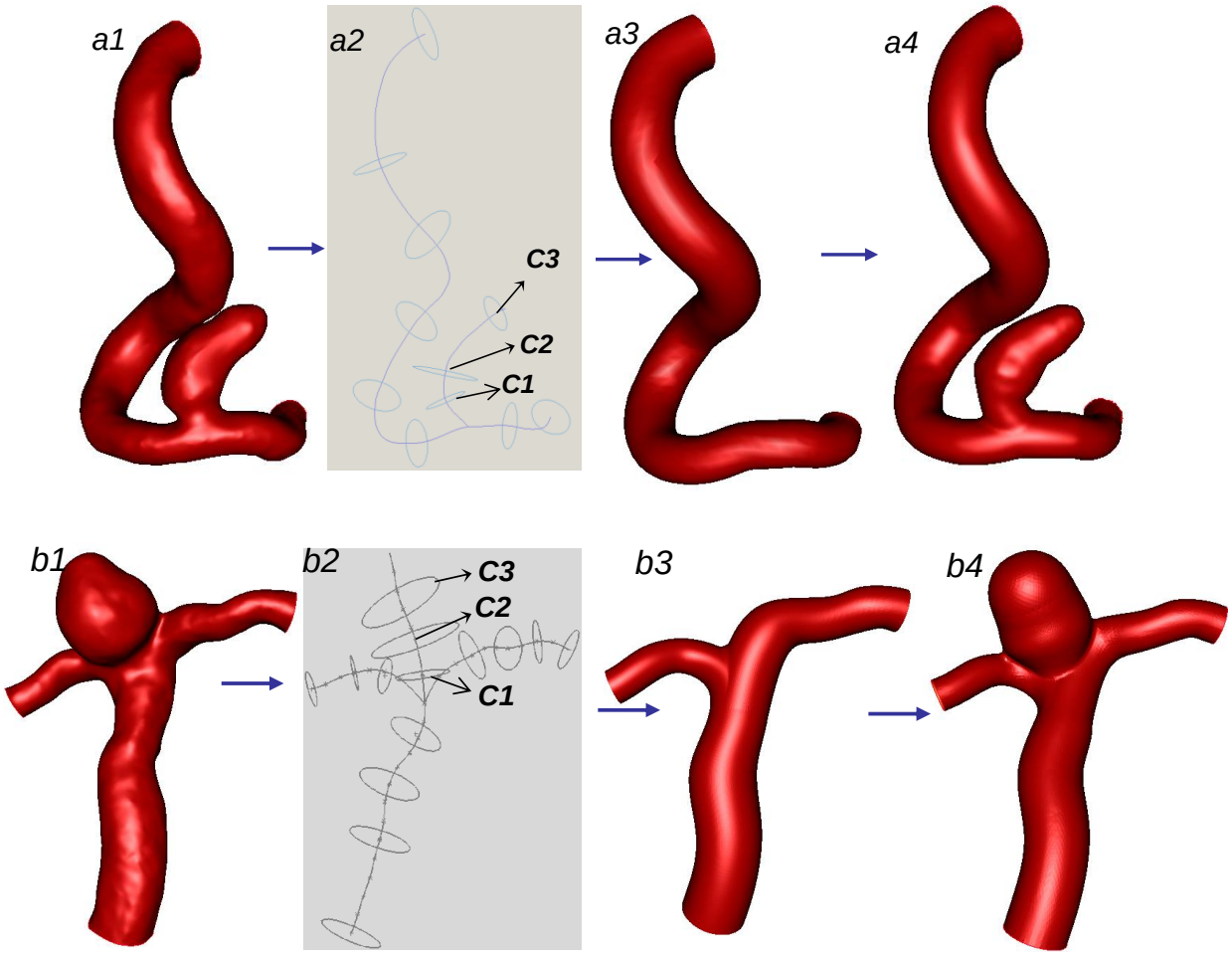

Figure 4.3 a: parametric model construction for side wall aneurysm (Model B); b: parametric model construction for bifurcation aneurysm (Model C); a1&b1: 3D reconstructed real geometry, a2&b2: model skeleton containing centerline and cross sections, a3&b3: parent artery, a4&b4: parametric model

To simplify the current models, relatively small surrounding arteries were truncated during the development (comparing Fig. 4.1 and 4.3). A superposition of the parent vasculature and aneurysm sac for Model C is shown in Fig. 4.4a and demonstrates the geometric relationship between aneurysm and the original bifurcation geometry. The ability of the parametric model to reproduce the real aneurysm geometry and neighboring vasculature was quantified using a point wise geometric error function, defined as the shortest distance between the reference (3D

reconstructed geometry) and parametric model. The surface of the reference and parametric models were triangulated, and the shortest distance between the surfaces was calculated using Geomagic Studio 9.0, (Geomagic Inc., North Carolina, USA).

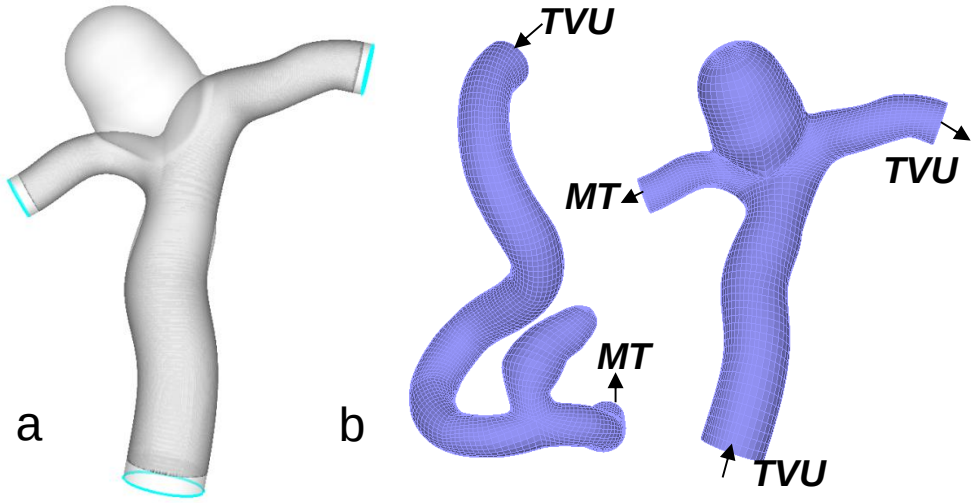

Figure 4.4 a. Aneurysm and bifurcation subtraction, shaded body is bifurcation and parent artery; b. finite element mesh of parametric models and boundary conditions, arrows indicate the flow directions.

CFD simulation

CFD models were constructed for both the parametric models and 3D reconstructed real geometries. Pulsatile blood flow in both models was analyzed using computational fluid dynamic (CFD) simulations. The CFD set up and fluid properties are the same as those used in Section 3.1.

For side wall aneurysm models, a time varying uniform (TVU) velocity profile was applied at the inlet based on representative volume flow rate [117]. A pulsatile flow waveform

was used from [118] The outlet condition was set by applying a modified traction condition (MT) or “do nothing” boundary condition [48, 49, 51].

For bifurcation aneurysm models, a TVU velocity profile was applied at the inlet based on volume flow rate at basilar artery and anterior cerebral artery [117, 119]. The inlet volume flow rate was split by assuming the same wall WSS level in the two bifurcating branches [82]; At one of these two branches, a TVU profile was used and a MT condition was used at the other (Fig. 4.4 b). For TVU conditions, a representative pulsatile waveform was used as in Section 3.1 [119]. The average Reynolds numbers (based on inlet diameter) ranged from 200 to 500 across all models, within the range for blood flow in Circle of Willis in human [81, 119]. The Womersley number ranged from 2 to 5 based on a pulsatile frequency of 1Hz, also in range of values reported for cerebral blood flow [97].

A finite element mesh of the computational domains was composed of 40000-50000 hexahedral (Fig. 4.4b). The same mesh style and comparable element quantity were used for 3D reconstructed real geometry and parametric models. CFD analyses were performed for each model for a period of two cardiac cycles using 100 time steps per cycle. Simulations were done using a 3-GHz dual Xeon processor work station with 4-GB of memory. The computational time ranged from 16 to 20 hours depending on model size.

The velocity field and flow streamlines were obtained using the CFD results. Time averaged WSS, and OSI were calculated and compared between the parametric and reconstructed geometries.

4.1.3 Results

Geometry

The average differences between the geometry of the parametric and 3D reconstructed models was between 1% to 5% of the local vessel diameter for nearly the entire model (Fig. 4.5). The maximum deviations (around 10% of local diameter) were found at the neck regions of all models and regions of highest curvature in the parent arteries.

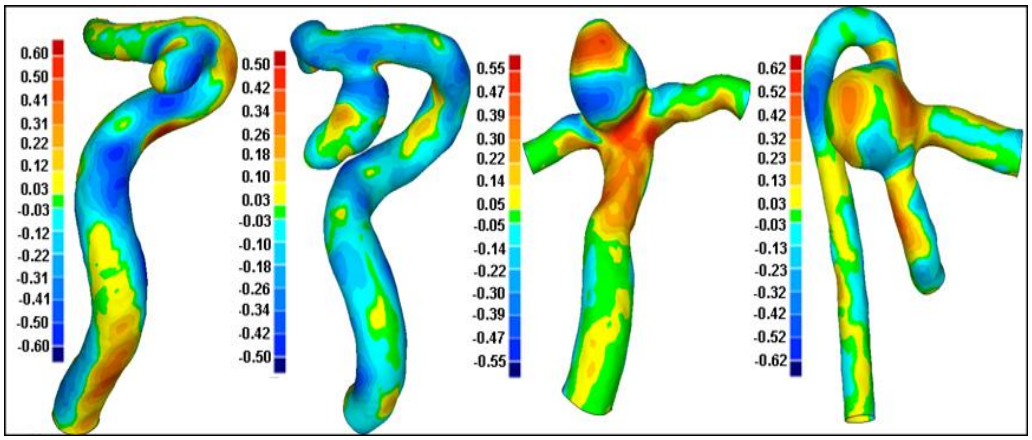

Figure 4.5 Contours of geometric error in lumen surface of the parametric models compared to the 3D reconstructed (real) geometry, units in mm.

Flow Structures

The flow streamlines of parametric models and 3D reconstructed geometries are shown in Fig. 4.6. For side wall aneurysms, the flow enters the aneurysm sac from the distal side of the neck, recirculates inside the sac and exits from the proximal side of the neck. One recirculation was found inside the low AR cases whereas two recirculations were observed in the high AR cases (Fig. 4.6a). For bifurcation aneurysms, flow enters the aneurysm mainly from one side (back side), makes a single recirculation and exits towards the two daughter branches (Fig. 4.6b). The

parametric models were able to capture these flow structures found in the 3D reconstructed for both side wall and bifurcation aneurysms.

The contours of the magnitude of cross sectional velocity give a more quantitative view of flow field (Fig. 4.7). The overall flow field matches very well between parametric models and reconstructed real geometries. The impingement region and inflow jet [7] were very similar in parametric models and reconstructed real geometries. The flow speed of the inflow jet in the aneurysm sac is slightly lower in the parametric model compared with real geometries.

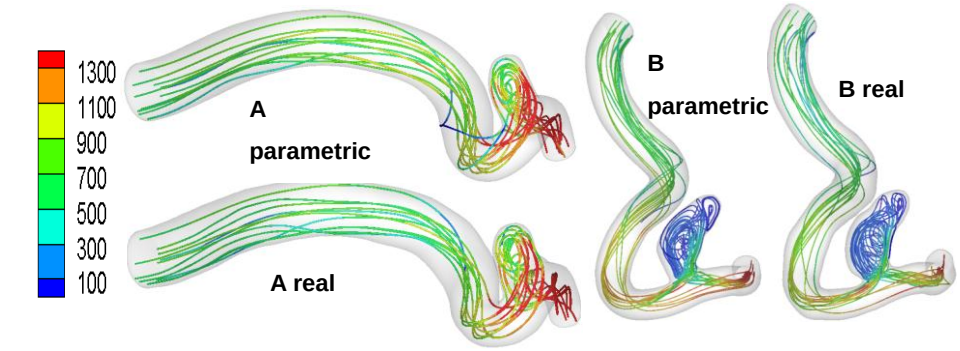

a.

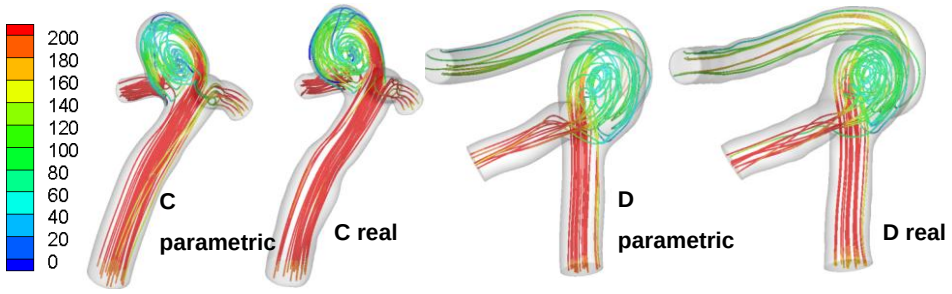

b.

Figure 4.6 Flow streamlines of parametric models and 3D reconstructed real geometries; a: sidewall aneurysms; b: bifurcation aneurysms (mm/s).

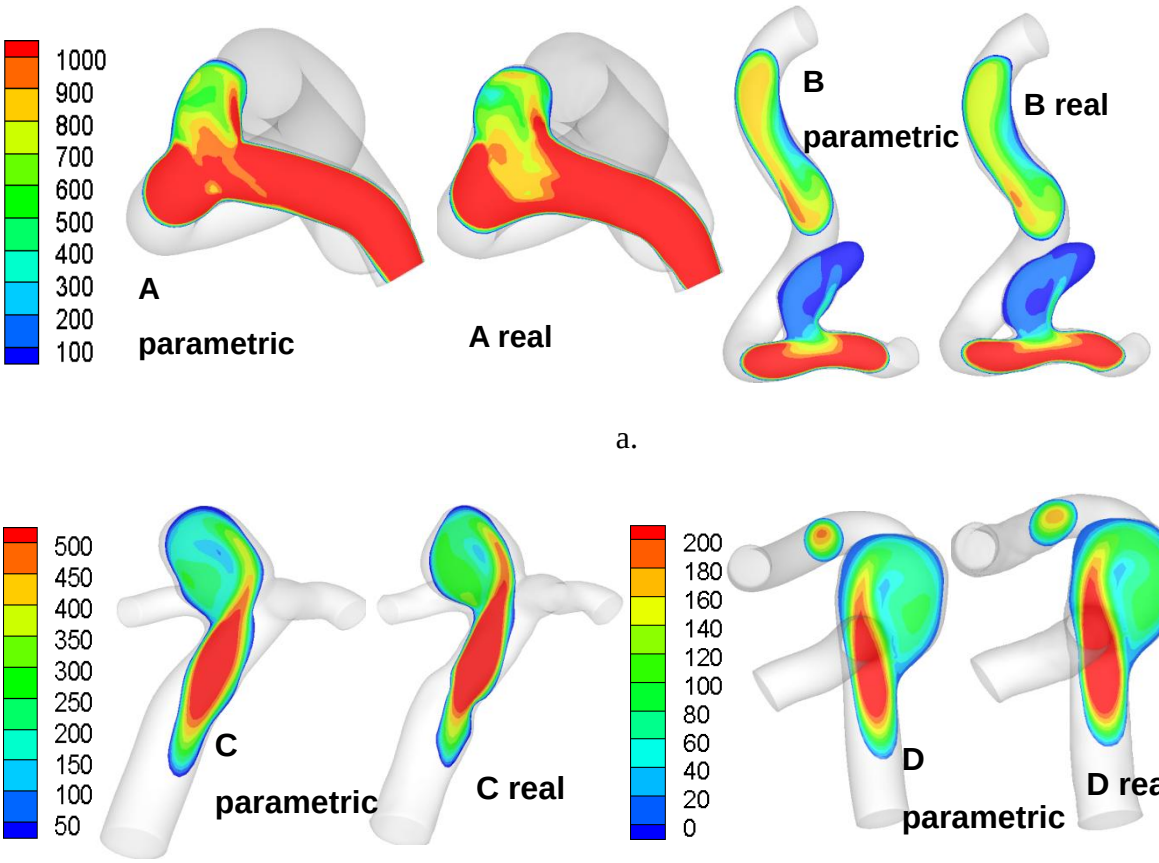

Figure 4.7 Cross sectional velocity magnitude (mm/s) contours for parametric and 3D reconstructed real geometries; a: side wall aneurysms; b: bifurcation aneurysms.

The overall TAWSS distributions were similar between parametric models and real geometries (Fig. 4.8). The parametric models were able to catch the regions of elevated TAWSS such as those found at the aneurysm necks and highly curved parent artery segments. For side wall aneurysms, elevated TAWSS was found at distal neck regions. In low AR case, another high TAWSS region was found in proximal dome region, whereas in high AR case, the majority of the aneurysm sac has TAWSS below 1 Pa. For bifurcation aneurysms, the TAWSS inside the

aneurysm sac was low compared to its parent arteries. For the aneurysm sacs, a slightly elevated TAWSS region was found in real geometries but not in parametric models.

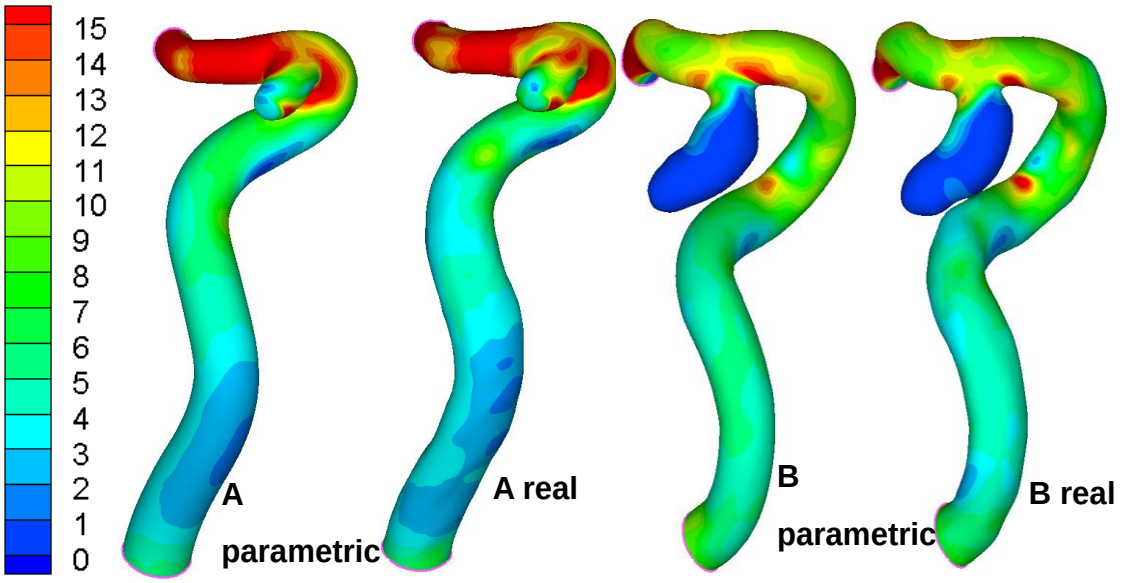

a.

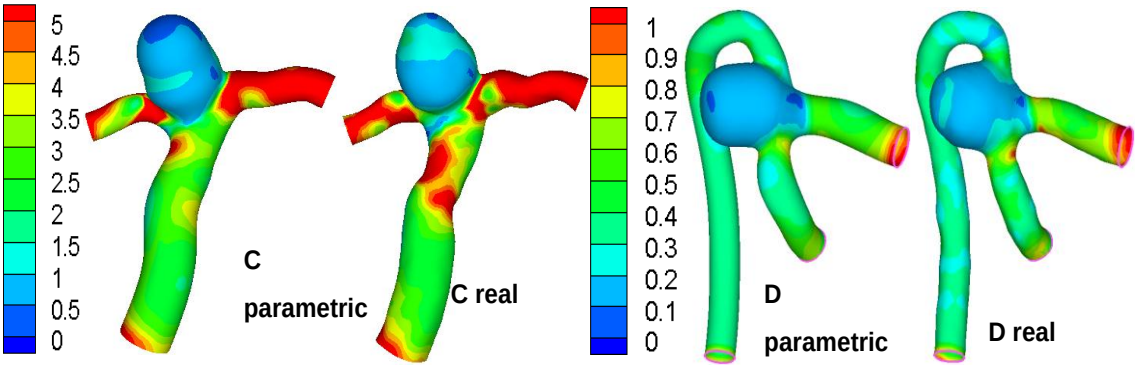

b.

Figure 4.8 Contours of time averaged WSS (Pa) for both and parametric models and reconstructed real geometries; (a) side wall aneurysms; (b) bifurcation aneurysms.

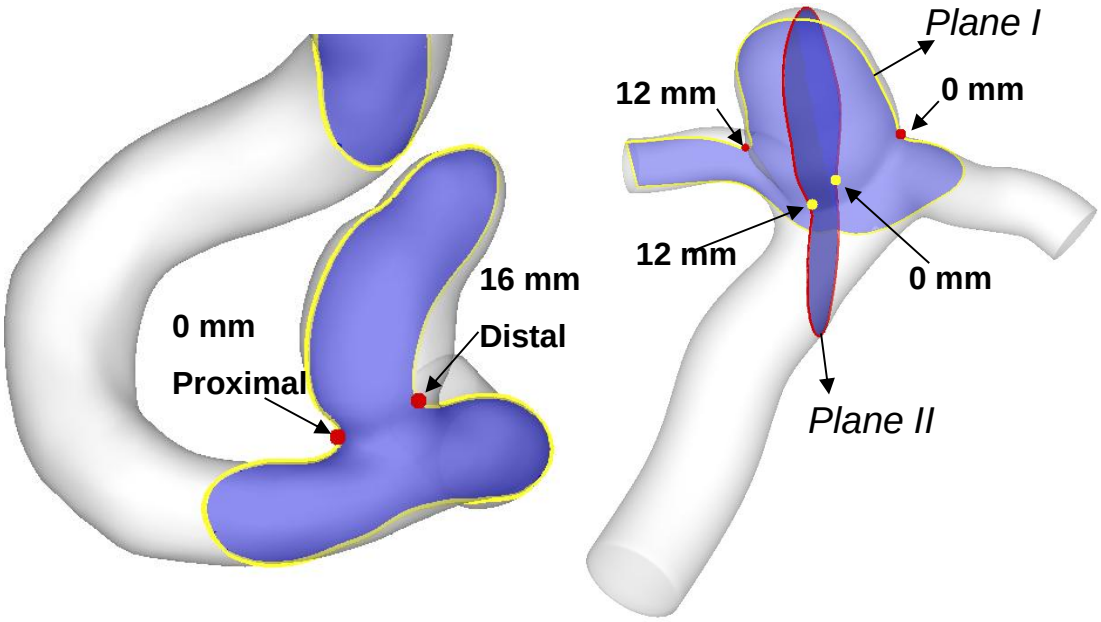

Figure 4.9 Schematic view of cross planes and intersecting curves for extracting the WSS; one plane for side wall case and two planes for bifurcation aneurysm; arrows indicate the starting and ending points of the intersecting curves.

A more quantitative comparison was done by extracting the WSS along intersecting curves (Fig. 4.9) and the distribution is shown in Fig. 4.10 and Fig. 4.11. For side wall aneurysms, the shape of WSS profile in parametric models match that in real geometries, whereas for low AR case, the second WSS peak was elevated and shifted to distal neck region in parametric model (Fig. 4.10). For bifurcation aneurysms, the overall WSS distribution was captured by parametric models except plane II in Model D (the first WSS peak in real geometry was not captured by parametric model) (Fig. 4.11). However, the WSS magnitude was lower in all parametric models than in real geometries.

The regions of elevated OSI in the real geometry are reproduced closely in the parametric models (Fig. 4.12). A high consistency in both location and magnitude is seen. All the elevated OSI regions are located in the aneurysm sac or aneurysm neck where complex flow pattern was found.

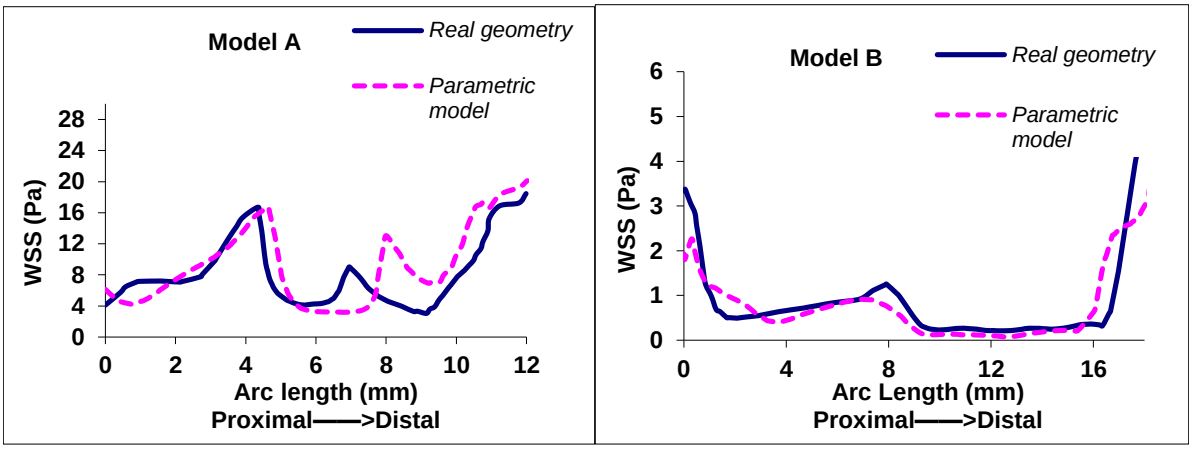

Figure 4.10 Extracted planar WSS profile for side wall aneurysms (Model A and Model B), X-axis indicates the arc length from proximal side to distal side of aneurysms.

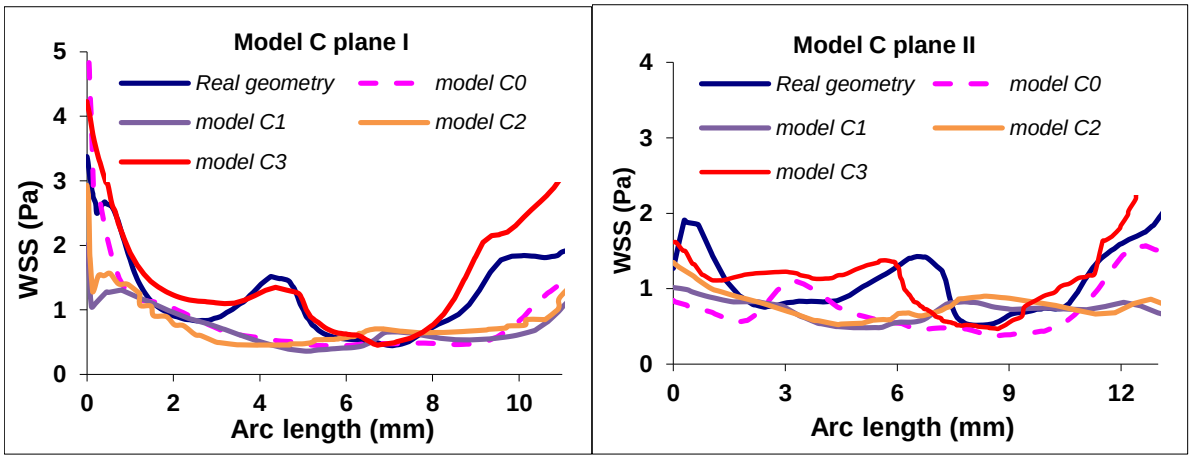

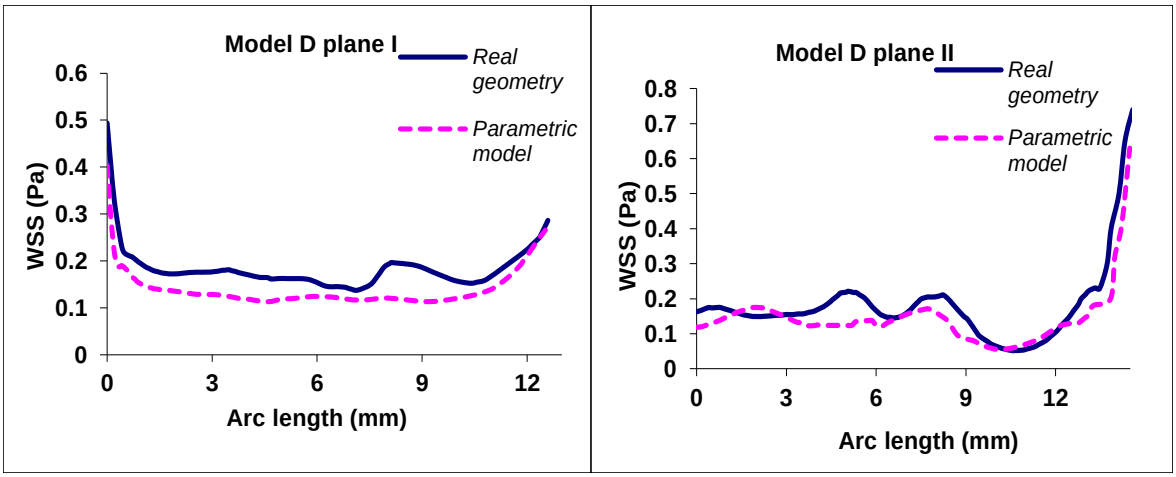

Figure 4.11 Extracted planar WSS profile for bifurcation aneurysms (Model C and Model D), two planes (I and II) perpendicular to each other were used for each model.

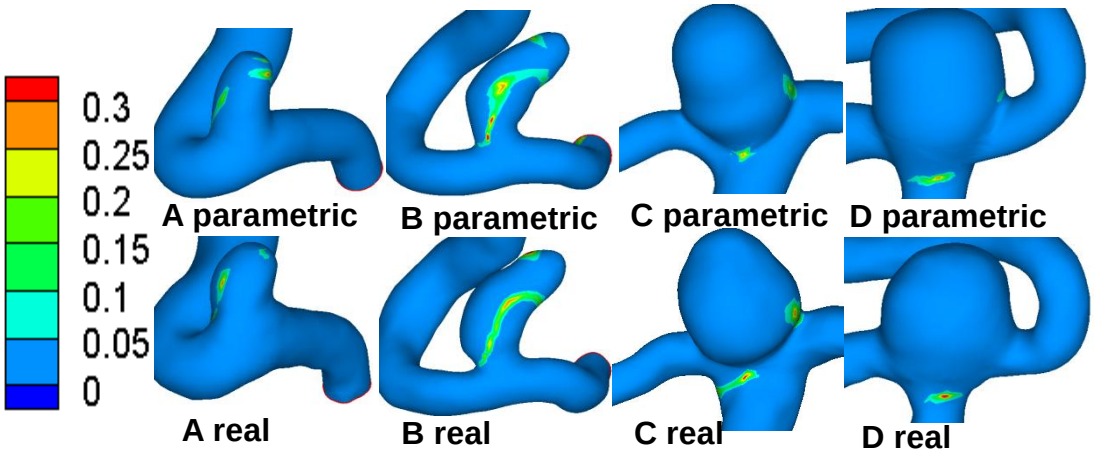

Figure 4.12 Contours of elevated OSI regions for real geometries and parametric models.

4.1.4 Discussion

A methodology for creating parametric cerebral aneurysm models has been developed and its ability to capture the geometric and hemodynamic features of realistic geometry has been evaluated. The surrounding vasculature was created using a previously developed method [116],

the “five cross section model” was used and all the cross sections were treated as circular. Three cross sections plus the centerline of aneurysm were used to reproduce the aneurysm geometry. The complete parametric model was formed by merging the parametric aneurysm model and surrounding parametric vascular model together. The geometric comparison shows the parametric models were able to reproduce the major features of the realistic geometry. Hemodynamic calculations also show a good match between parametric models and realistic geometries both qualitatively and quantitatively.

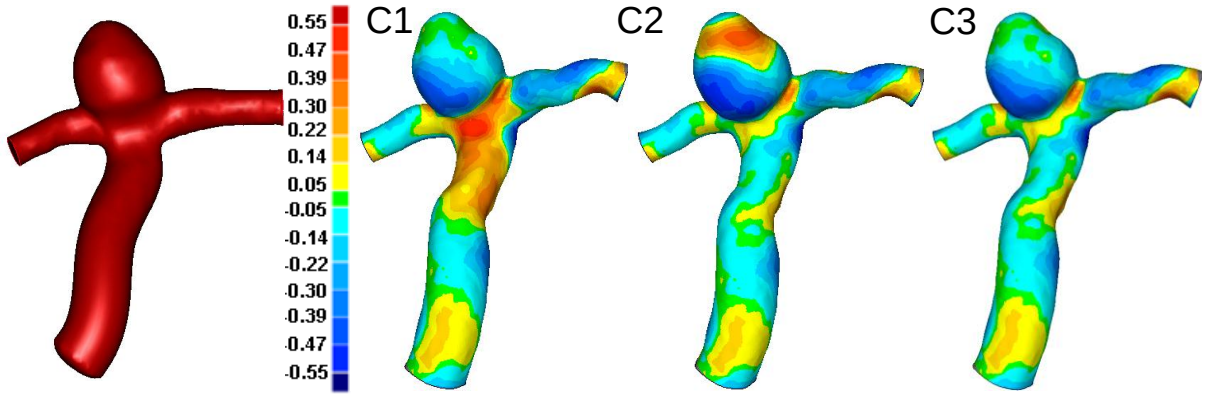

Figure 4.13 Improved parametric geometry (Model C): model geometry with both improved aneurysm and parent artery (left); and geometric comparison between models C1 (improved aneurysm), C2 (improved parent artery) and C3 (improved both).

The quantitative comparison of WSS between parametric models and realistic geometries show a consistent overall distribution; however, some large local variations (around 50% in WSS difference) between the two were noticed (Fig. 4.10 and 4.11, Model C and D, plane II). A comparison between Figure 4.5 and Figure 4.8 shows that all large variations of WSS between parametric models and real geometries were found in regions of large geometric errors. Unsurprisingly, all the large geometric errors were found at the high curvature regions (error

~10% of local diameters), where the current parametric models were unable to capture the curved surfaces accurately. The main reason of this was the use of limited number of cross sections and simple cross section shape (circular). Since one of the objectives in developing these parametric models was to minimize the number of model variables (e.g. number of cross sections, shape of cross sections) while still maintaining a good match with the hemodynamics in the real geometry. If desired, information from additional cross sections from the vessels and aneurysm sac can be included in the parametric model. Fig. 4.13 shows another construction of Model C with 4 cross sections for the aneurysm, the geometric difference decreased and the WSS distribution is closer to the real geometry compared to the previous model (Fig. 4.11). Furthermore, the cross sectional shape, which was idealized as circular for all the parent arteries and bifurcation aneurysms, can be generalized using elliptic or more complex shapes.

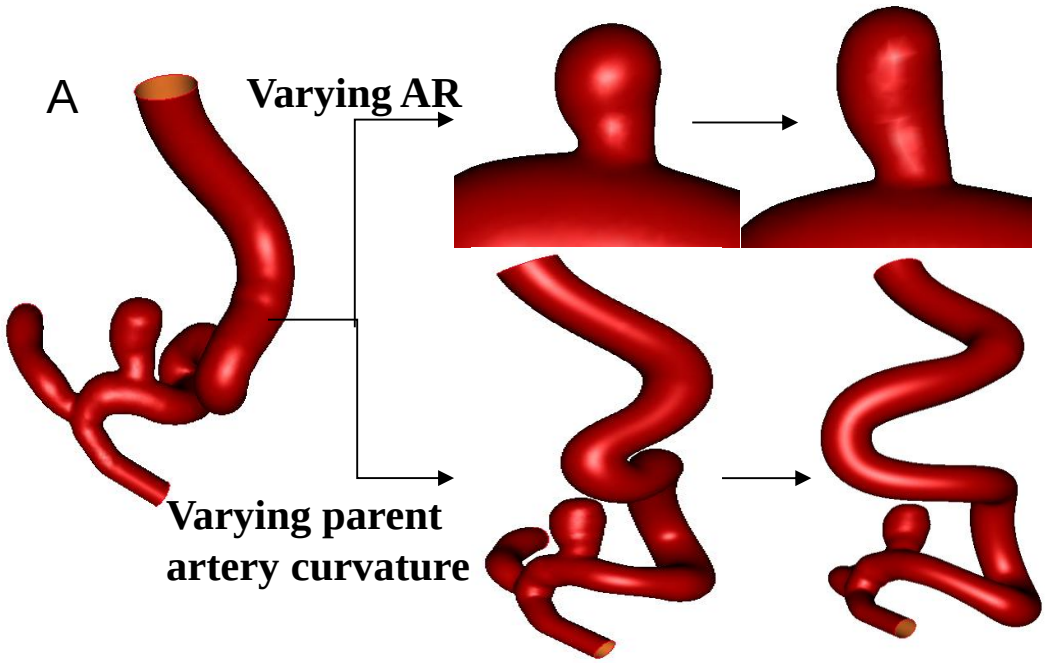

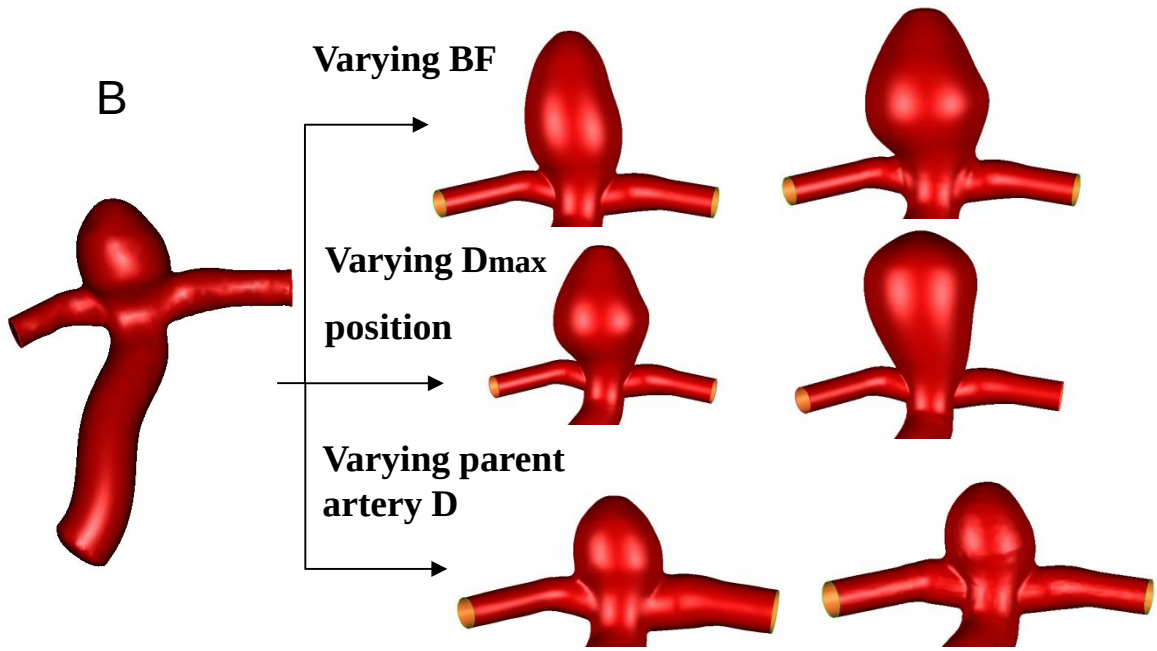

Figure 4.14 Examples of parametric modeling on aneurysm and parent artery, A: side wall aneurysm case; B: bifurcation aneurysm case.

Patient specific geometries have been used in hemodynamics studies of cerebral aneurysms [7, 8, 10, 120]. The shape and size of the aneurysms also have been analyzed and quantified, different parameters and geometric ratios were measured and calculated to categorize the aneurysms [93, 121]. While the geometry is one of the determining factors of hemodynamics in the aneurysms, it is desirable to vary the geometric parameters of the aneurysm and its parent arteries systematically in this kind of study. In this way, the geometric parameters (such as aneurysm height, neck diameter, maximum diameter and in-plane or out-plane angles) or shape ratios (such as AR, bottle neck factor (BF), non-spherical index (NSI) and parent-to-neck ratio) [75, 93] can be correlated with hemodynamic features.

While we have emphasized hemodynamics in this work, the intramural stresses also play an important role in the health of the arterial wall. The parametric models can be used to assess the importance of geometric parameters on the distribution of intramural stress and thus indirectly on biomechanical derived changes in the wall. Another aspect of parametric modeling is to evaluate the effect of various geometric parameters on hemodynamic conditions in the aneurysm sac and assess the risk factor of aneurysm rupture and further help the decision making and treatment planning in clinical practices. Figure 4.14 shows an example of parametric modeling of aneurysm at the internal carotid artery and its parent artery. By varying the AR and neck diameter of the aneurysm (parent artery keeps the same) and also changing the parent artery curvature (aneurysm geometry keeps the same), a parametric study can be conducted systematically.

4.1.5 Conclusion

This parametric model captures important geometric and hemodynamic features for the four aneurysms and neighboring arteries obtained from human cerebral vasculature data sets. In the future, these parametric models will be used in parametric studies of remodeling and rupture of ICA. They can also be used to guide 3D reconstruction of poor quality clinical and animal model data.

BIBLIOGRAPHY

[1] Hademenos, G. J., 1995, "The physics of cerebral aneurysms," Physics Today, Vol.48(Issue 2), p. 24.

[2] Foutrakis, G. N., Yonas, H., and Sclabassi, R. J., 1999, "Saccular aneurysm formation in curved and bifurcating arteries," Ajnr: American Journal of Neuroradiology, 20(7), pp. 1309-1317.

[3] Weir, B., 2002, "Unruptured intracranial aneurysms: a review," Journal of Neurosurgery, 96(1), pp. 3-42.

[4] Broderick, J. P., Brott, T. G., Duldner, J. E., Tomsick, T., and Leach, A., 1994, "Initial and recurrent bleeding are the major causes of death following subarachnoid hemorrhage," Stroke; A Journal Of Cerebral Circulation, 25(7), pp. 1342-1347.

[5] Winn, H. R., Jane, J. A., Sr., Taylor, J., Kaiser, D., and Britz, G. W., 2002, "Prevalence of asymptomatic incidental aneurysms: review of 4568 arteriograms.[see comment]," Journal of Neurosurgery, 96(1), pp. 43-49.

[6] Kaminogo, M., Yonekura, M., and Shibata, S., 2003, "Incidence and outcome of multiple intracranial aneurysms in a defined population," Stroke, 34(1), pp. 16-21.

[7] Cebral, J. R., Castro, M. A., Burgess, J. E., Pergolizzi, R. S., Sheridan, M. J., and Putman, C. M., 2005, "Characterization of Cerebral Aneurysms for Assessing Risk of Rupture By Using Patient-Specific Computational Hemodynamics Models," AJNR Am J Neuroradiol, 26(10), pp. 2550-2559.

[8] Shojima, M., Oshima, M., Takagi, K., Torii, R., Hayakawa, M., Katada, K., Morita, A., and Kirino, T., 2004, "Magnitude and role of wall shear stress on cerebral aneurysm: computational fluid dynamic study of 20 middle cerebral artery aneurysms," Stroke, 35(11), pp. 2500-2505.

[9] Hassan, T., Timofeev, E. V., Saito, T., Shimizu, H., Ezura, M., Matsumoto, Y., Takayama, K., Tominaga, T., and Takahashi, A., 2005, "A proposed parent vessel geometry-based categorization of saccular intracranial aneurysms: computational flow dynamics analysis of the risk factors for lesion rupture," Journal of Neurosurgery, 103(4), pp. 662-680.

[10] Steinman, D. A., Milner, J. S., Norley, C. J., Lownie, S. P., and Holdsworth, D. W., 2003, "Image-based computational simulation of flow dynamics in a giant intracranial aneurysm," AJNR Am J Neuroradiol, 24(4), pp. 559-566.

[11] Karmonik, C., Yen, C., Diaz, O., Klucznik, R., Grossman, R. G., and Benndorf, G., "Temporal variations of wall shear stress parameters in intracranial aneurysms-importance of patient-specific inflow waveforms for CFD calculations," Acta Neurochir (Wien).

[12] Parlea, L., Fahrig, R., Holdsworth, D. W., and Lownie, S. P., 1999, "An analysis of the geometry of saccular intracranial aneurysms," Ajnr: American Journal of Neuroradiology, 20(6), pp. 1079-1089.

[13] LaMack, J. A., Himburg, H. A., Li, X. M., and Friedman, M. H., 2005, "Interaction of wall shear stress magnitude and gradient in the prediction of arterial macromolecular permeability," Ann Biomed Eng, 33(4), pp. 457-464.

[14] Tardy, Y., Resnick, N., Nagel, T., Gimbrone, M. A., Jr., and Dewey, C. F., Jr., 1997, "Shear stress gradients remodel endothelial monolayers in vitro via a cell proliferation-migration-loss cycle," Arterioscler Thromb Vasc Biol, 17(11), pp. 3102-3106.

[15] Altes, T. A., Cloft, H. J., Short, J. G., DeGast, A., Do, H. M., Helm, G. A., and Kallmes, D. F., 2000, "1999 ARRS Executive Council Award. Creation of saccular aneurysms in the rabbit: a model suitable for testing endovascular devices. American Roentgen Ray Society," AJR. American Journal of Roentgenology, 174(2), pp. 349-354.

[16] Ding, Y. H., Dai, D., Lewis, D. A., Cloft, H. J., and Kallmes, D. F., 2005, "Angiographic and histologic analysis of experimental aneurysms embolized with platinum coils, Matrix, and HydroCoil," AJNR Am J Neuroradiol, 26(7), pp. 1757-1763.

[17] Sadasivan, C., Cesar, L., Seong, J., Rakian, A., Hao, Q., Tio, F. O., Wakhloo, A. K., and Lieber, B. B., 2009, "An original flow diversion device for the treatment of intracranial aneurysms: evaluation in the rabbit elastase-induced model," Stroke, 40(3), pp. 952-958.

[18] Seong, J., Wakhloo, A. K., and Lieber, B. B., 2007, "In vitro evaluation of flow divertors in an elastase-induced saccular aneurysm model in rabbit," J Biomech Eng, 129(6), pp. 863-872.

[19] Mohan, S., Mohan, N., Valente, A. J., and Sprague, E. A., 1999, "Regulation of low shear flow-induced HAEC VCAM-1 expression and monocyte adhesion," Am J Physiol, 276(5 Pt 1), pp. C1100-1107.

[20] Murray, C. D., 1926, "The Physiological Principle of Minimum Work: I. The Vascular System and the Cost of Blood Volume," Proc Natl Acad Sci U S A, 12(3), pp. 207-214.

[21] Glagov, S., Zarins, C., Giddens, D. P., and Ku, D. N., 1988, "Hemodynamics and atherosclerosis. Insights and perspectives gained from studies of human arteries," Arch Pathol Lab Med, 112(10), pp. 1018-1031.

[22] Kamiya, A., and Togawa, T., 1980, "Adaptive regulation of wall shear stress to flow change in the canine carotid artery," Am J Physiol, 239(1), pp. H14-21.

[23] Langille, B. L., 1996, "Arterial remodeling: relation to hemodynamics," Can J Physiol Pharmacol, 74(7), pp. 834-841.

[24] Zamir, M., 1976, "Optimality principles in arterial branching," J Theor Biol, 62(1), pp. 227-251.

[25] Kleinstreuer, C., Hyun, S., Buchanan, J. R., Jr., Longest, P. W., Archie, J. P., Jr., and Truskey, G. A., 2001, "Hemodynamic parameters and early intimal thickening in branching blood vessels," Critical Reviews in Biomedical Engineering, 29(1), pp. 1-64.

[26] Malek, A. M., and Izumo, S., 1996, "Mechanism of endothelial cell shape change and cytoskeletal remodeling in response to fluid shear stress," Journal Of Cell Science, 109 (Pt 4), pp. 713-726.

[27] Ku, D. N., 1997, "Blood Flow In Arteries," Annual Review of Fluid Mechanics, 29(1), pp. 399-434.

[28] Davies, P. F., Shi, C., Depaola, N., Helmke, B. P., and Polacek, D. C., 2001, "Hemodynamics and the focal origin of atherosclerosis: a spatial approach to endothelial structure, gene expression, and function," Annals of the New York Academy of Sciences, 947, pp. 7-16; discussion 16-17.

[29] Nagel, T., Resnick, N., Dewey, C. F., Jr., and Gimbrone, M. A., Jr., 1999, "Vascular endothelial cells respond to spatial gradients in fluid shear stress by enhanced activation of transcription factors," Arterioscler Thromb Vasc Biol, 19(8), pp. 1825-1834.

[30] Jou, L. D., Wong, G., Dispensa, B., Lawton, M. T., Higashida, R. T., Young, W. L., and Saloner, D., 2005, "Correlation between lumenal geometry changes and hemodynamics in fusiform intracranial aneurysms," Ajnr: American Journal of Neuroradiology, 26(9), pp. 2357-2363.

[31] Mangrum, W. I., Farassati, F., Kadirvel, R., Kolbert, C. P., Raghavakaimal, S., Dai, D., Ding, Y. H., Grill, D., Khurana, V. G., and Kallmes, D. F., 2007, "mRNA expression in

rabbit experimental aneurysms: a study using gene chip microarrays," AJNR Am J Neuroradiol, 28(5), pp. 864-869.

[32] Meng, H., Wang, Z., Hoi, Y., Gao, L., Metaxa, E., Swartz, D. D., and Kolega, J., 2007, "Complex Hemodynamics at the Apex of an Arterial Bifurcation Induces Vascular Remodeling Resembling Cerebral Aneurysm Initiation," Stroke, 38(6), pp. 1924-1931.

[33] Nerem, R. M., Rumberger, J. A., Jr., Gross, D. R., Hamlin, R. L., and Geiger, G. L., 1974, "Hot-film anemometer velocity measurements of arterial blood flow horses," Circ Res, 34(2), pp. 193-203.

[34] Shahcheraghi, N., Dwyer, H. A., Cheer, A. Y., Barakat, A. I., and Rutaganira, T., 2002, "Unsteady and three-dimensional simulation of blood flow in the human aortic arch," Journal of Biomechanical Engineering, 124(4), pp. 378-387.

[35] Gao, L., Hoi, Y., Swartz, D. D., Kolega, J., Siddiqui, A., and Meng, H., 2008, "Nascent aneurysm formation at the basilar terminus induced by hemodynamics," Stroke; A Journal Of Cerebral Circulation, 39(7), pp. 2085-2090.

[36] Hashimoto, N., Handa, H., Nagata, I., and Hazama, F., 1980, "Experimentally induced cerebral aneurysms in rats: Part V. Relation of hemodynamics in the circle of Willis to formation of aneurysms," Surgical Neurology, 13(1), pp. 41-45.

[37] Kayembe, K. N., Sasahara, M., and Hazama, F., 1984, "Cerebral aneurysms and variations in the circle of Willis," Stroke, 15(5), pp. 846-850.

[38] Sasaki, T., Kodama, N., and Itokawa, H., 1996, "Aneurysm formation and rupture at the site of anastomosis following bypass surgery. Case report," Journal of Neurosurgery, 85(3), pp. 500-502.

[39] Sekhar, L. N., and Heros, R. C., 1981, "Origin, growth, and rupture of saccular aneurysms: a review," Neurosurgery, 8(2), pp. 248-260.

[40] Haljasmaa, I. V., Robertson, A. M., and Galdi, G. P., 2001, "On the effect of apex geometry on wall shear stress and pressure in two-dimensional models of arterial bifurcations,," Mathematical Models and Methods in Applied Sciences, 11(3), pp. 499-520.

[41] Chung, B. J., 2004, "The study of blood flow in arterial bifurcations: the influence of hemodynamics on endothelial cell response to vessel wall mechanics.," Ph.D. thesis, University of Pittsburgh.

[42] Kučera, P., and Skalák, Z., 1998, "Local Solutions to the Navier-Stokes Equations with Mixed Boundary Conditions," Acta Applicandae Mathematicae, 54(3), pp. 275-288.

[43] Weir, B., Amidei, C., Kongable, G., Findlay, J. M., Kassell, N. F., Kelly, J., Dai, L., and Karrison, T. G., 2003, "The aspect ratio (dome/neck) of ruptured and unruptured aneurysms.," Journal of Neurosurgery, 99(3), pp. 447-451.

[44] Chung, B. J., 2004, "The study of blood flow in arterial bifurcations: the influence of hemodynamics on endothelial cell response to vessel wall mechanics.," Ph.D. thesis, University of Pittsburgh

[45] Chung, B. J., Robertson, A. M., and Peters, D. G., 2003, "The numerical design of a parallel plate flow chamber for investigation of endothelial cell response to shear stress," Computers & Structures, 81(8-11), pp. 535-546.

[46] Meng, H., Swartz, D. D., Wang, Z., Hoi, Y., Kolega, J., Metaxa, E. M., Szymanski, M. P., Yamamoto, J., Sauvageau, E., and Levy, E. I., 2006, "A model system for mapping vascular responses to complex hemodynamics at arterial bifurcations in vivo," Neurosurgery, 59(5), pp. 1094-1100; discussion 1100-1091.

[47] Bathe, K. J., Zhang, H., and Zhang, X., 1997, "Some advances in the analysis of fluid flows," Computers & Structures, 64(5-6), pp. 909-930.

[48] Gresho, P. M., 2001, "Some current CFD issues relevant to the incompressible Navier-Stokes equations," Computer Methods in Applied Mechanics and Engineering, 87(2-3), pp. 201-252.

[49] Heywood, J. G., Rannacher, R., and Turek, S., 1996, "Artificial boundaries and flux and pressure conditions for the incompressible Navier-Stokes equations," International Journal for Numerical Methods in Fluids, 22(5), pp. 325-352.

[50] Galdi, G. P., 2008, "Mathematical problems in classical and non-newtonian fluid mechanics," Hemodynamical Flows: Modeling, Analysis and Simulation, Oberwolfach Seminars, G. Galidi, R. Rannacher, A. Robertson, and S. Turek, eds., Birkhauswer.

[51] Leone, J. M., and Gresho, P. M.,, 1981, "Finite element simulations of steady, two-dimensional, viscous incompressible flow over a step," Journal of Computational Physics, 41(1), pp. 167-191.

[52] Li, D., and Robertson, A. M., 2009, "A structural multi-mechanism damage model for cerebral arterial tissue," J Biomech Eng, 131(10), p. 101013.

[53] Truesdell, C., and Noll, W., 1965, The non-linear field theories of mechanics, Springer-Verlag, Berlin New York,.

[54] Huo, Y., Guo, X., and Kassab, G. S., 2008, "The flow field along the entire length of mouse aorta and primary branches," Annals of Biomedical Engineering, 36(5), pp. 685-699.

[55] Berger, S. A., and Jou, L.-D., 2000, "Flows in Stenotic Vessels," Annual Review of Fluid Mechanics, 32(1), pp. 347-382.

[56] Lou, Z., and Yang, W. J., 1992, "Biofluid dynamics at arterial bifurcations," Crit Rev Biomed Eng, 19(6), pp. 455-493.

[57] Robertson, A. M., Sequeira, A., and Kameneva, M. V., 2008, "Hemorheology," Hemodynamical Flows: Modeling, Analysis and Simulation, G. P. Galdi, R. Rannacher, A. M. Robertson, and S. Turek, eds., Birkhäuser.

[58] Szymanski, M. P., Metaxa, E., Meng, H., and Kolega, J., 2008, "Endothelial cell layer subjected to impinging flow mimicking the apex of an arterial bifurcation," Ann Biomed Eng, 36(10), pp. 1681-1689.

[59] Frangos, J. A., Huang, T. Y., and Clark, C. B., 1996, "Steady shear and step changes in shear stimulate endothelium via independent mechanisms--superposition of transient and sustained nitric oxide production," Biochemical & Biophysical Research Communications, 224(3), pp. 660-665.

[60] McCann, J. A., Peterson, S. D., Plesniak, M. W., Webster, T. J., and Haberstroh, K. M., 2005, "Non-uniform flow behavior in a parallel plate flow chamber : alters endothelial cell responses," Ann Biomed Eng, 33(3), pp. 328-336.

[61] DePaola, N., Gimbrone, M. A., Jr., Davies, P. F., and Dewey, C. F., Jr., 1992, "Vascular endothelium responds to fluid shear stress gradients.[erratum appears in Arterioscler Thromb 1993 Mar;13(3):465]," Arteriosclerosis & Thrombosis, 12(11), pp. 1254-1257.

[62] Dolan, J. M., Meng, H., Singh, S., Paluch, R., and Kolega, J., "High fluid shear stress and spatial shear stress gradients affect endothelial proliferation, survival, and alignment," Ann Biomed Eng, 39(6), pp. 1620-1631.

[63] Sakamoto, N., Saito, N., Han, X., Ohashi, T., and Sato, M., "Effect of spatial gradient in fluid shear stress on morphological changes in endothelial cells in response to flow," Biochem Biophys Res Commun, 395(2), pp. 264-269.

[64] Anderson, E. J., Falls, T. D., Sorkin, A. M., and Knothe Tate, M. L., 2006, "The imperative for controlled mechanical stresses in unraveling cellular mechanisms of mechanotransduction," Biomed Eng Online, 5, p. 27.

[65] Buchanan, J. R., Jr., Kleinstreuer, C., Truskey, G. A., and Lei, M., 1999, "Relation between non-uniform hemodynamics and sites of altered permeability and lesion growth at the rabbit aorto-celiac junction," Atherosclerosis, 143(1), pp. 27-40.

[66] Lei, M., Archie, J. P., and Kleinstreuer, C., 1997, "Computational design of a bypass graft that minimizes wall shear stress gradients in the region of the distal anastomosis," Journal of Vascular Surgery, 25(4), pp. 637-646.

[67] Keynton, R. S., Evancho, M. M., Sims, R. L., Rodway, N. V., Gobin, A., and Rittgers, S. E., 2001, "Intimal hyperplasia and wall shear in arterial bypass graft distal anastomoses: an in vivo model study," J Biomech Eng, 123(5), pp. 464-473.

[68] Fukuda, S., Hashimoto, N., Naritomi, H., Nagata, I., Nozaki, K., Kondo, S., Kurino, M., and Kikuchi, H., 2000, "Prevention of rat cerebral aneurysm formation by inhibition of nitric oxide synthase," Circulation, 101(21), pp. 2532-2538.

[69] Kondo, S., Hashimoto, N., Kikuchi, H., Hazama, F., Nagata, I., and Kataoka, H., 1997, "Cerebral aneurysms arising at nonbranching sites. An experimental Study," Stroke, 28(2), pp. 398-403; discussion 403-394.

[70] Roach, M. R., 1978, "A model study of why some intracranial aneurysms thrombose but others rupture," Stroke, 9(6), pp. 583-587.

[71] Short, J. G., Fujiwara, N. H., Marx, W. F., Helm, G. A., Cloft, H. J., and Kallmes, D. F., 2001, "Elastase-induced saccular aneurysms in rabbits: comparison of geometric features with those of human aneurysms," Ajnr: American Journal of Neuroradiology, 22(10), pp. 1833-1837.

[72] Kadirvel, R., Ding, Y. H., Dai, D., Lewis, D. A., Raghavakaimal, S., Cloft, H. J., and Kallmes, D. F., 2008, "Gene expression profiling of experimental saccular aneurysms using deoxyribonucleic acid microarrays," AJNR Am J Neuroradiol, 29(8), pp. 1566-1569.

[73] Kadirvel, R., Ding, Y.-H., Dai, D., Zakaria, H., Robertson, A. M., Danielson, M. A., Lewis, D. A., Cloft, H. J., and Kallmes, D. F., 2007, "The influence of hemodynamic forces on biomarkers in the walls of elastase-induced aneurysms in rabbits," Neuroradiology, 49(12), pp. 1041-1053.

[74] Sadatomo, T., Yuki, K., Migita, K., Taniguchi, E., Kodama, Y., and Kurisu, K., 2008, "Morphological differences between ruptured and unruptured cases in middle cerebral artery aneurysms," Neurosurgery, 62(3), p. 602.

[75] Ujiie, H., Tachibana, H., Hiramatsu, O., Hazel, A. L., Matsumoto, T., Ogasawara, Y., Nakajima, H., Hori, T., Takakura, K., and Kajiya, F., 1999, "Effects of size and shape (aspect ratio) on the hemodynamics of saccular aneurysms: a possible index for surgical treatment of intracranial aneurysms," Neurosurgery, 45(1), pp. 119-129; discussion 129-130.

[76] Ujiie, H., Tamano, Y., Sasaki, K., and Hori, T., 2001, "Is the aspect ratio a reliable index for predicting the rupture of a saccular aneurysm?," Neurosurgery, 48(3), pp. 495-502; discussion 502-493.

[77] Ding, Y. H., Danielson, M. A., Kadirvel, R., Dai, D., Lewis, D. A., Cloft, H. J., and Kallmes, D. F., 2006, "Modified technique to create morphologically reproducible elastase-induced aneurysms in rabbits," Neuroradiology, 48(8), pp. 528-532.

[78] Kallmes, D. F., Fujiwara, N. H., Yuen, D., Dai, D., and Li, S. T., 2003, "A collagen-based coil for embolization of saccular aneurysms in a New Zealand White rabbit model," AJNR Am J Neuroradiol, 24(4), pp. 591-596.

[79] Humphrey, J. D., Kang, T., Sakarda, P., and Anjanappa, M., 1993, "Computer-aided vascular experimentation: a new electromechanical test system," Annals of Biomedical Engineering, 21(1), pp. 33-43.

[80] Zamir, M., 2000, The Physics of Pulsatile Flow, Springer, New York.

[81] Hendrikse, J., van Raamt, A. F., van der Graaf, Y., Mali, W. P. T. M., and van der Grond, J., 2005, "Distribution of cerebral blood flow in the circle of Willis," Radiology, 235(1), pp. 184-189.

[82] Zamir, M., 1977, "Shear forces and blood vessel radii in the cardiovascular system," Journal of General Physiology, 69(4), pp. 449-461.

[83] Womersley, J. R., 1955, "Method for the calculation of velocity, rate of flow and viscous drag in arteries when the pressure gradient is known," J Physiol, 127(3), pp. 553-563.

[84] Malek, A. M., Alper, S. L., and Izumo, S., 1999, "Hemodynamic shear stress and its role in atherosclerosis," JAMA, 282(21), pp. 2035-2042.

[85] He, X., and Ku, D. N., 1996, "Pulsatile flow in the human left coronary artery bifurcation: average conditions," Journal of Biomechanical Engineering, 118(1), pp. 74-82.

[86] Castro, M. A., Putman, C. M., and Cebral, J. R., 2006, "Computational fluid dynamics modeling of intracranial aneurysms: effects of parent artery segmentation on intra-aneurysmal hemodynamics," AJNR Am J Neuroradiol, 27(8), pp. 1703-1709.

[87] Steinman, D. A., 2002, "Image-based computational fluid dynamics modeling in realistic arterial geometries," Annals of Biomedical Engineering, 30(4), pp. 483-497.

[88] Ding, Y. H., Dai, D., Danielson, M. A., Kadirvel, R., Lewis, D. A., Cloft, H. J., and Kallmes, D. F., 2007, "Control of aneurysm volume by adjusting the position of ligation

during creation of elastase-induced aneurysms: a prospective study," Am J Neuroradiol, 28, pp. 857-859.

[89] Ding, Y. H., Dai, D., Lewis, D. A., Danielson, M. A., Kadirvel, R., Cloft, H. J., and Kallmes, D. F., 2006, "Long-term patency of elastase-induced aneurysm model in rabbits," Ajnr: American Journal of Neuroradiology, 27(1), pp. 139-141.

[90] Ding, Y. H., Dai, D., Lewis, D. A., Danielson, M. A., Kadirvel, R., Mandrekar, J. N., Cloft, H. J., and Kallmes, D. F., 2005, "Can neck size in elastase-induced aneurysms be controlled? A prospective study," Ajnr: American Journal of Neuroradiology, 26(9), pp. 2364-2367.

[91] Ding, Y. H., Dai, D., Lewis, D. A., Danielson, M. A., Kadirvel, R., Mandrekar, J. N., Cloft, H. J., and Kallmes, D. F., 2006, "Can neck size in elastase-induced aneurysms be controlled? A retrospective study," AJNR Am J Neuroradiol, 27(8), pp. 1681-1684.

[92] Ebina, K., Shimizu, T., Sohma, M., and Iwabuchi, T., 1990, "Clinico-statistical study on morphological risk factors of middle cerebral artery aneurysms," Acta Neurochir (Wien), 106(3-4), pp. 153-159.

[93] Raghavan, M. L., Ma, B., and Harbaugh, R. E., 2005, "Quantified aneurysm shape and rupture risk," Journal of Neurosurgery, 102(2), pp. 355-362.

[94] Zeng, Z., Kallmes, D. F., Durka, M., Ding, Y., Lewis, D., Kadirvel, R., and Robertson, A. M., 2010, "Sensitivity of CFD Based Hemodynamic Results in Rabbit Aneurysm Models to Idealizations in surrounding Vasculature," ASME Journal of Biomechanical Engineering-T ASME, 132.

[95] Steinman, D. A., Milner, J. S., Norley, C. J., Lownie, S. P., and Holdsworth, D. W., 2003, "Image-based computational simulation of flow dynamics in a giant intracranial aneurysm.[comment]," Ajnr: American Journal of Neuroradiology, 24(4), pp. 559-566.

[96] Zhao, M., Amin-Hanjani, S., Ruland, S., Curcio, A. P., Ostergren, L., and Charbel, F. T., 2007, "Regional cerebral blood flow using quantitative MR angiography," American Journal of Neuroradiology, 28(8), pp. 1470-1473.

[97] Vriens, E. M., Wieneke, G. H., Hillen, B., Eikelboom, B. C., Van Huffelen, A. C., and Visser, G. H., 2001, "Flow redistribution in the major cerebral arteries after carotid endarterectomy: a study with transcranial Doppler scan," Journal of Vascular Surgery, 33(1), pp. 139-147.

[98] Shojima, M., Oshima, M., Takagi, K., Torii, R., Nagata, K., Shirouzu, I., Morita, A., and Kirino, T., 2005, "Role of the bloodstream impacting force and the local pressure elevation in the rupture of cerebral aneurysms," Stroke, 36(9), pp. 1933-1938.

[99] Jou, L. D., Lee, D. H., Morsi, H., and Mawad, M. E., 2008, "Wall shear stress on ruptured and unruptured intracranial aneurysms at the internal carotid artery," AJNR Am J Neuroradiol, 29(9), pp. 1761-1767.

[100] Hoi, Y., Meng, H., Woodward, S. H., Bendok, B. R., Hanel, R. A., Guterman, L. R., and Hopkins, L. N., 2004, "Effects of arterial geometry on aneurysm growth: three-dimensional computational fluid dynamics study," Journal of Neurosurgery, 101(4), pp. 676-681.

[101] Mantha, A., Karmonik, C., Benndorf, G., Strother, C., and Metcalfe, R., 2006, "Hemodynamics in a cerebral artery before and after the formation of an aneurysm," American Journal of Neuroradiology, 27(5), pp. 1113-1118.

[102] Karmonik, C., Klucznik, R., and Benndorf, G., 2008, "Blood flow in cerebral aneurysms: comparison of phase contrast magnetic resonance and computational fluid dynamics--preliminary experience," Rofo, 180(3), pp. 209-215.

[103] Lall, R. R., Eddleman, C. S., Bendok, B. R., and Batjer, H. H., 2009, "Unruptured intracranial aneurysms and the assessment of rupture risk based on anatomical and morphological factors: sifting through the sands of data," Neurosurg Focus, 26(5), p. E2.

[104] Nader-Sepahi, A., Casimiro, M., Sen, J., and Kitchen, N. D., 2004, "Is aspect ratio a reliable predictor of intracranial aneurysm rupture?," Neurosurgery, 54(6), pp. 1343-1347; discussion 1347-1348.

[105] Zeng, Z., Kallmes, D. F., Durka, M. J., Ding, Y., Lewis, D., Kadirvel, R., and Robertson, A. M., 2011, "Hemodynamics and anatomy of elastase-induced rabbit aneurysm models--similarity with human cerebral aneurysms?," AJNR Am J Neuroradiol, March, 32: 595 - 601.

[106] Himburg, H. A., Grzybowski, D. M., Hazel, A. L., LaMack, J. A., Li, X. M., and Friedman, M. H., 2004, "Spatial comparison between wall shear stress measures and porcine arterial endothelial permeability," Am J Physiol Heart Circ Physiol, 286(5), pp. H1916-1922.

[107] Kaazempur-Mofrad, M. R., Isasi, A. G., Younis, H. F., Chan, R. C., Hinton, D. P., Sukhova, G., LaMuraglia, G. M., Lee, R. T., and Kamm, R. D., 2004, "Characterization of the atherosclerotic carotid bifurcation using MRI, finite element modeling, and histology," Ann Biomed Eng, 32(7), pp. 932-946.

[108] Ku, D. N., Giddens, D. P., Zarins, C. K., and Glagov, S., 1985, "Pulsatile flow and atherosclerosis in the human carotid bifurcation. Positive correlation between plaque location and low oscillating shear stress," Arteriosclerosis, 5(3), pp. 293-302.

[109] Kadirvel, R., Ding, Y. H., Dai, D., Lewis, D. A., and Kallmes, D. F., "Differential expression of genes in elastase-induced saccular aneurysms with high and low aspect ratios," Neurosurgery, 66(3), pp. 578-584; discussion 584.

[110] Z. Zeng, D. F. K., Y.Ding, R. Kadirvel, D. A. Lewis, A. M. Robertson, "Hemodynamics of Elastase-induced aneurysms model in rabbits-a new high flow bifurcation model," Proceeding of ASME Summer Bioengineering Conference, Famington, Pennsylvania, USA, June 22-25, 2011.

[111] Fujiwara, N. H., Cloft, H. J., Marx, W. F., Short, J. G., Jensen, M. E., and Kallmes, D. F., 2001, "Serial angiography in an elastase-induced aneurysm model in rabbits: evidence for progressive aneurysm enlargement after creation," AJNR Am J Neuroradiol, 22(4), pp. 698-703.

[112] Kadirvel, R., Ding, Y. H., Dai, D., Lewis, D. A., and Kallmes, D. F., 2010, "Differential expression of genes in elastase-induced saccular aneurysms with high and low aspect ratios," Neurosurgery, 66(3), pp. 578-584; discussion 584.

[113] Huang, J., and van Gelder, J. M., 2002, "The probability of sudden death from rupture of intracranial aneurysms: a meta-analysis," Neurosurgery, 51(5), pp. 1101-1105; discussion 1105-1107.

[114] J. van Gijn, and G. J. Rinkel, 2001, "Subarachnoid heamorrhage: diagnosis, cause and management," Brain, 124, pp. 249-278.

[115] Steiger, H. J., 1990, "Pathophysiology of development and rupture of cerebral aneurysms," Acta Neurochir Suppl (Wien), 48, pp. 1-57.

[116] Zakaria, H., Robertson, A. M., and Kerber, C. W., 2008, "A parametric model for studies of flow in arterial bifurcations," Ann Biomed Eng, 36(9), pp. 1515-1530.

[117] Moore, S., David, T., Chase, J. G., Arnold, J., and Fink, J., 2006, "3D models of blood flow in the cerebral vasculature," J Biomech, 39(8), pp. 1454-1463.

[118] Oshima, M., Torii, R., Kobayashi, T., Taniguchi, N., and Takagi, K., 2001, "Finite element simulation of blood flow in the cerebral artery," Computer Methods in Applied Mechanics and Engineering, 191(6-7), pp. 661-671.

[119] Fahrig, R., Nikolov, H., Fox, A. J., and Holdsworth, D. W., 1999, "A three-dimensional cerebrovascular flow phantom," Medical Physics, 26(8), pp. 1589-1599.

[120] Jou, L. D., Quick, C. M., Young, W. L., Lawton, M. T., Higashida, R., Martin, A., and Saloner, D., 2003, "Computational approach to quantifying hemodynamic forces in giant cerebral aneurysms," Ajnr: American Journal of Neuroradiology, 24(9), pp. 1804-1810.

[121] Ma, B., Harbaugh, R. E., and Raghavan, M. L., 2004, "Three-dimensional geometrical characterization of cerebral aneurysms," Annals of Biomedical Engineering, 32(2), pp. 264-273.